PVCap as Kinetic Hydrate Inhibitor in Gas-Water Systems

Master of Science thesis in process technology

by

Archana Parmar

Department of Physics and Technology

University of Bergen, Norway

November 2009

Abstract

In this work, molecular dynamic (MD) simulations were employed on different model systems of practical and theoretical significance to investigate possible mechanisms of kinetic hydrate inhibition. Water/methane interface structuring and possible precursors to hydrate nucleation have been investigated using a model system of water and methane at different densities. The impact of oligomers, specifically Poly-N-VinylCaprolactam (PVCap) dodecamer, on structuring of water/methane interfaces at different methane densities was investigated utilizing two different sets of partial atomic charges. In yet another system, the effect of high PVCap concentration on water restructuring was also analyzed. Regions of stability for methane hydrate have been investigated using a model system consisting of a slab of hydrate embedded in liquid water. Solvation Model 6 was applied to obtain charges on PVCap atoms using density functional theory with B3LYP and STO-6-31+G** basis set. MM3 force field parameters were used to handle torsional and angle-bending motions. Intermolecular interactions were treated by a combination of Coulomb and Lennard-Jones potentials. Temperature was first controlled by a simple velocity scaling and then towards the end of the simulation run, Nosé-Hoover thermostat was used.

Systems containing liquid water and methane showed certain signs of hydrate nucleation. The dissolution of methane into water appeared to increase with methane concentration. PVCap formed hydrogen bonds with water via carbonyl oxygen and hence hindered water reordering needed to build hydrate cages from liquid water. The PVCap behavior was shown to be heavily affected by its concentration in water and distribution of atomic charges. At low concentrations, PVCap preferred the water-methane interface and did not interact with each other, similar to another kinetic inhibitor, PVP (Kvamme et al. 2005). When the liquid PVCap content was high, it evidently modified the interfacial tension of water-methane surface, converting the initially dispersed methane phase into separated bubbles. The PVCap molecules then built a system-wide network that covered the interface between water and methane bubbles. The orientations and interactions of PVCap molecule with other molecules was influenced by the distribution of the partial atomic charges.

Charges obtained via Charge Model 4 proved to result in a more reliable behavior than those obtained by means of the Löwdin population analysis.

Several of the hydrate-containing systems showed a tendency to melt when in contact with liquid water even at temperatures (200K, 240K) well below the hydrate stability region. This behavior was attributed to the fact that hydrate volume available in a MD experiment is small and lacks the stabilizing presence of bulk.

An article involving the work in this thesis is in the process of being written. The findings were presented at the Seventh International Conference of Computational Methods in Sciences and Engineering (ICCMSE 2009), and an extended abstract will appear in its proceedings.

Acknowledgement

First, I offer my sincere gratitude to my supervisor, Professor Tatiana Kuznetsova, who has supported me throughout my thesis with her experience and provided me with invaluable feedback on this thesis. I would also like to express my deep sense of gratitude to my co-supervisor, Professor Bjørn Kvamme for guiding me through this research experience.

I am heartily thankful to my colleague Bjørnar Jensen for his excellent guidance and help on building the PVCap model. I am deeply thankful to Per Fotland for helping me to develop the practical understanding of this subject and providing me feedback on my work.

University of Bergen Library provided me with the books, research material needed, Bergen Center for Computational Science provided me with the supercomputer to run my simulation, and I am thankful to them.

In my daily work, I have been blessed with a friendly and cheerful group of fellow students. I am thankful to My Ngo, Khuram Baig, Alusine Jalloh and all others for always supporting me and making the life pleasant.

Finally, my special acknowledgment goes to my family for their love, understanding and warm support.

Abbreviations:

AO	Atomic orbital
B3LYP	Becke, three-parameter, Lee-Yang-Parr
CM4	Charge model 4
DFT	Density functional theory
DSC	Differential scanning calorimetry
FCC	Face centered cubic lattice
GH	Gas hydrate
GTO	Gaussian type orbital
HEN	Heterogeneous nucleation
HF	Hartree-Fock
HON	Homogeneous nucleation
KHI	Kinetic hydrate inhibitor
LCAO	Linear combination of atomic orbital
LDHI	Low dosage hydrate inhibitor
L-J	Lennard-Jones
LPA	Löwdin population analysis
MD	Molecular dynamics
md43	Molecular dynamics version 4.3
MK	Monte Carlo
MM3	Molecular mechanics force field
MO	Molecular orbital
NVT	Number of atoms, volume and temperature
OPLS	Optimized potential for liquid simulations
OPLS-AA	Optimized potential for liquid simulations for all atoms
PBC	Periodic boundary conditions
PDB	Protein data bank
PSI-C	2PVCap(with Charge model 4 charges)+1306water+260methane system
PSII-C	2PVCap(with Charge model 4 charges)+1306water+520methane system
PSIII-C	9PVCap(with Charge model 4 charges)+1306water+260methane system
PSIII-L	9PVCap(with Löwdin population analysis charges) + 1306 water + 260 methane system
PSII-L	2PVCap(with Löwdin population analysis charges) + 1306 water + 520 methane system
PSI-L	2PVCap(with Löwdin population analysis charges) + 1306 water + 260 methane system
QM	Quantum mechanics
RDF	Radial distribution function

RLPA	Redistributed Löwdin population analysis
RSI	Reference system I with 1306 water + 260 methane
RSII	Reference system II with 1306 water + 520 methane
SCF	Self consistent field
SI	Structure I
SII	Structure II
SH	Structure H
SIV-A	System IV at 240K (water--hydrate--water--methane system)
SIV-B	System IV at 200K (water--hydrate--water--methane system)
SIV-C	System IV at 190K (water--hydrate--water--methane system)
SM6	Solvation model 6
SPC/E	Simple point charge/extended
STO	Slater type orbital
VMD	Visual molecular dynamics

Symbols:

$\vec{a}$	Acceleration
γ	Activity coefficient
$\phi, \theta, \psi, \omega$	Angles
k_B	Boltzmann constant
l	Bond length
$\overline{h_z}$	Box length in the direction normal to the interface
Ω_{NVT}	Canonical partition function
h	Cavity partition function
C_{ZZ} ; D_{ZZ}	Charge model 4 parameters
μ	Chemical potential
σ	Collision diameter or interfacial tension
N_c	Coordination number
r_c	Critical radius
ρ	Density
ε_0	Dielectric permittivity of vacuum
P_e	Electron density matrix
J	Electron-electron Coulombic energy
ΔG	Excess Gibbs free energy
$\vec{F}$	Force
K, V_1 , V_2, V_3	Force constant
Δg_v	Free energy change per unit volume
G	Gibbs free energy
$\hat{H}$	Hamilton operator

A	Helmholtz free energy
Υ	Interfacial free energy
T_S	Kinetic energy
φ	Lennard-Jones 12-6 potential
m, Q	Mass
B	Mayer bond order
V_{m}	Molar volume
x	Mole fraction
Z	Nuclear charge
N	Number of atoms
v	Number of cavities formed per water molecule
C	Number of components
P'	Number of phases in the system
F	Number of the degrees of freedom
S	Overlap matrix
g(r)	Pair correlation function
P_r	Parachor contribution
q	Partial charge
$\vec{x}$	Position
U	Potential energy
P	Pressure
T'	Quadratic function of Mayer bond order
r	Radius or distance between two sites
T	Temperature
t	time
E	Total energy
R	Universal gas constant
$\vec{\mathrm{v}}$	Velocity
V	Volume
Ψ	Wave function
ε	Well depth

Superscripts and subscripts:

i, j, k, k', A, B, C, D	Atoms
x, y, z	Axis
$c$ut	Cut-off
c	Electron correlation term
x	Electron exchange term
e	Equilibrium
xc	Exchange and correlation term

ne	Electron –nuclear interaction
ES	Electrostatic interaction
O,H	Empty hydrate
$exact$	Exact energy from Hartree-Fock theory
$B88$	Exchange correction proposed by Becke
H	Hydrate
$LSDA$	Local spin density approximation
LYP	Lee, Yang and par
s	Surface
v	Volume
w	Water
i, j, k, k', A, B, C, D	Atoms

Contents

1 Introduction 1

2 Goals & methods 4

3 Natural gas hydrates 6

3.1 Hydrate types & formers 6

3.2 Structure I hydrate 7

3.3 Thermodynamics of hydrate formation 8

3.3.1 The Gibbs phase rule 10

3.3.2 Hydrate formation 10

3.4 Nucleation 12

3.4.1 Hydrate nucleation at the molecular Level 14

3.5 Hydrate inhibition 16

3.5.1 Physical inhibition 16

3.5.2 Chemical inhibition 17

4 Kinetic hydrate inhibitors (KHIs) 19

4.1 History and experimental results 19

4.2 Theories and mechanisms 23

4.2.1 The Massachusetts Institute of Technology (MIT) 23

4.2.2 The University of Warwick group (UOW) 24

4.2.3 The University of Bergen (UIB) 24

5 Computational methods 26

5.1 Quantum mechanics 27

5.1.1 The Schrödinger equation 27

5.1.2 Basis sets 27

5.1.3 Density functional theory 29

5.1.4 Continuum solvation models 30

5.1.5 Partial atomic charges 31

5.2 Molecular dynamics 33

5.2.1 Verlet algorithms 33

5.2.2 Canonical ensemble 34

5.2.3 Periodic boundary conditions 35

5.2.4 Molecular interactions 36
5.2.5 Radial distribution function 39
5.2.6 Quaternion 40
5.2.7 Constraint dynamics 41
5.2.8 Nosé-Hoover thermostat 42
6 Previous simulational work 45
7 Strategy 50
8 Simulational details 52
8.1 Molecular models 52
8.1.1 SPC/E water model 52
8.1.2 OPLS one-site methane model 53
8.1.3 PVCap dodecamer model 53
8.2 Setup of simulation systems 58
8.2.1 Reference systems I and II 60
8.2.2 PVCap systems I and II 61
8.2.3 PVCap system III 62
8.2.4 System IV 63
9 System evolution, results and discussion 65
9.1 Reference system I & II 65
9.2 PVCap system I 74
9.3 PVCap system II 85
9.4 PVCap system III 96
9.5 System IV 103
10 Conclusion 106
11 Suggestions for further work 109
References 111
Appendix A 115
Appendix B 119

1 Introduction

Natural Gas hydrates are crystalline, non-stoichiometric clathrate compounds comprised of hydrogen-bonded water lattices, which encapsulate suitably sized molecules like methane, carbon dioxide or other naturally occurring gases, at high pressure (>1.5 MPa) and low temperatures(<25 °C) (Sloan 1998). It is primarily due to their crystalline, insoluble, non-flowing nature that hydrates have been of concern to petroleum industry. Plugging of natural gas transportation lines, because of the solid ice-like hydrates can lead to serious accidents in the worst-case scenario and long downtime in the best cases. Natural gas hydrate occurrence is a significant factor to be considered during oil and gas exploration, production and transportation (Englezos 1993; Sloan 1998).

Several strategies have been developed to prevent hydrate formation, such as heating, insulation, and addition of kinetic or thermodynamic inhibitors. On the Norwegian Continental Shelf, the most common strategy for hydrate plugging prevention is to use thermodynamic inhibitors such as methanol. The amount of methanol can be as high as 40% of the water content. Environmental and economical concerns for the use of methanol have provided the driving force for development of Low dosage hydrate inhibitors (LDHIs).

Recently, a change in hydrate paradigm has resulted in a shift of focus from total hydrate prevention to risk management (Sloan 2005). Risk management is more economical as it allows hydrate formation, if plug formation is avoided. Kinetic hydrate inhibitors (KHIs) are a type of LDHIs that delay nucleation and growth of hydrate crystals for substantial period of time rather than prevent it altogether. There are also many side-benefits of using KHIs such as reduced storage and injection facilities (Kelland 1994).

The mechanism by which KHIs delay the massive hydrate growth & plugging is not well understood. Some studies related the inhibition activities to the effects of the LDHIs on the water structuring during homogeneous nucleation, thereby preventing the formation of the critical nuclei (Kelland 2006; Moon et al. 2007). Other researchers suggested that nucleation and/or crystal growth inhibition is achieved via adsorption on the hydrate surface (Larsen et al. 1998; Hutter et al. 2000). However, knowledge about their effects on the unavoidable

heterogeneous nucleation of gas hydrate is limited (Colle et al. 1999). Several types of KHIs have been tested, including Poly-N-VinylCaprolactam(PVCap) and Vinylpyrrolidone(PVP). However, PVCap has been recognized to be a more effective inhibitor than PVP (Lederhos et al. 1996; Kvamme et al. 2005). One of the essential prerequisites for designing better LDHIs is a molecular-level understanding of the mechanisms by which they work, which requires commensurate understanding of hydrate nucleation and growth (Moon et al. 2007). But the nucleation part of hydrate formation process cannot be completely probed and predicted using the state-of-the-art experimental technology (Radhakrishnan and Trout 2002).

Several software platforms capable of predicting the effect of thermodynamic inhibitors (alcohols, salts) are currently available for evaluation of hydrate prevention issues. However, there exists no software able to estimating the impact of KHIs on the kinetic rates of massive hydrate formation. If the mechanism and working of KHIs are completely comprehended, then they can be incorporated in the software for further use in the Oil and Gas Industry.

Molecular dynamics is a valuable tool for evaluating potential candidates for kinetic hydrate inhibitors, since it reduces the expensive testing of inhibitors in laboratory-scale or pilot-scale experiments. CPU-time, after all, becomes cheaper and cheaper almost by the minute.

The purpose of this study was to study the impact of PVCap on hydrate pre-nucleation due to water restructuring in the water/pure methane system. Molecular dynamic simulations were used for this purpose. Both behavior and orientation of the PVCap molecule will be heavily affected by the chosen combination of force fields. MM3 force field parameters were used for angular and torsional movements in PVCap. The distribution of partial atomic charge will especially have large impact on the behavior of PVCap molecule. Hence, it was decided to model PVCap dodecamer using the quantum mechanics approach. Currently, there are no available literature data on actual experimental values for the charge distribution on PVCap dodecamer, and hence there was nothing to compare with the quantum mechanics-obtained charges. Due to this, two different set of charges calculated from Löwdin population analysis (LPA) and Charge Model 4 (CM4) were used. Three different system setups were studied with PVCap molecules. System I consisted of 2 PVCap dodecamers (12-unit monomers) inserted in water phase stacked side by side with a methane phase. A reference system

without PVCap was also constructed to compare the direct effect of PVCap addition. System II was set up similar to System I except that in this system the concentration of methane was doubled to observe how PVCap would be able to delay nucleation under higher driving forces for hydrate formation. System III involved high concentrations of PVCap. 9 PVCap dodecamers were inserted in the dispersed water-methane phase to study the effect of high PVCap concentrations on restructuring in the system.

We also planned to study the effect of the PVCap in a system consisting of a slab of hydrate alongside a water – methane – water phase so that the PVCap's impact and adsorption preferences could be studied in the system having two interfaces, liquid water – methane and hydrate – liquid water. A stable hydrate phase is necessary to begin this analysis. For this, the simulations were first run without PVCap at different temperature to find the hydrate stability temperature. In these simulations, hydrate showed the tendency to melt even at very low temperatures and thus these systems were not studied with PVCap. In all, there were 11 different simulations run in this work to obtain insights into the inhibition mechanism of hydrate nucleation and further growth.

Varying the PVCap concentration plays a significant role in analyzing its impact as surfactant in presence of water and hydrocarbon phase. Since PVCap is a surfactant, our working hypothesis stated that it will mainly concentrate at the interfaces disrupting the local structuring of water and methane molecules, and thereby increasing the induction time for nucleation and hydrate formation. Also at a high formation driving force, the PVCap partial atomic charges played a major role. PVCap molecule with the LPA charges tended to promote the nucleation process rather than delay it. In contrast to this, PVCap with the CM4 charges was proven to demonstrate hydrate inhibition effect.

2 Goals & methods

The primary goal in this thesis was to study the effect of oligomers, specifically PVCap dodecamer, on delaying the nucleation process and inhibiting hydrate formation. The secondary goal was to see the effect of PVCap concentration on the behavior of water-methane system and ultimately, inhibition and formation of hydrate.

Structural analysis of efficient kinetic inhibitors has pointed out two distinct features: 1) a non-polar backbone, which will theoretically facilitate the contact with the nonpolar phase in a combined water/hydrocarbon system, and 2) very specific distances between branches containing polar groups. "Specific" means in this context that the distance between them should make it difficult for surrounding water molecules to structure into regular hydrogen bonded structures of either hydrate type. The complexity and the size of systems needed to approximate the behavior of real life systems obviously excluded quantum mechanics as a feasible method, with the only two reasonable choices left were Monte Carlo (MK) and Molecular Dynamics (MD), with different quantum chemistry techniques to estimate charge distribution in the model kinetic inhibitors. We ruled out Monte Carlo due to lack of dynamic information and the risk of potentially missing certain pathways of dynamic development by inappropriate choice of MK steps.

To achieve these goals, a representative interaction model for PVCap is an obvious requirement. Charge distributions obtained through different approximations in quantum mechanics may differ significantly, and it was found essential to establish two sets from different methods to obtain some sensitivity of results on different characterizations. To consider the bending and twisting moments in PVCap molecule, reliable force field parameters were needed. MM3 (molecular mechanics force field (Allinger et al. 1989; Allinger and Durkin 2000)) force field parameters were selected to represent angles and torsions in PVCap molecules.

Model system without kinetic inhibitor was chosen to serve as a reference. In order to study the impact of inhibitor on systems under the influence of different driving forces for hydrate formation, two systems differing only in the concentration of non-polar methane phase were

constructed. A system with high inhibitor content was also built to analyze the effect of inhibitor concentration. To study the interfacial preference and PVCap's inhibition impact after the hydrate formation, a system containing a stable hydrate phase with two interfaces, hydrate-liquid water and methane-liquid water was also included in the study.

3 Natural gas hydrates

Natural gas hydrates are ice-like solid structures formed in the presence of water and gas molecules (CO_2, CH_4, C_2H_6, etc.) when water form cages entrapping guest molecules. Formation of hydrate is promoted at high pressure and low temperature conditions (Carroll 2003).

3.1 Hydrate types & formers

There are two types of hydrates commonly encountered in the petroleum field. These are called Structure I (SI) and Structure II (SII). A third type of hydrate that may also occur is Structure H (SH), but it is much less common. The unit cells of the three structures are shown in Figure 3-1.

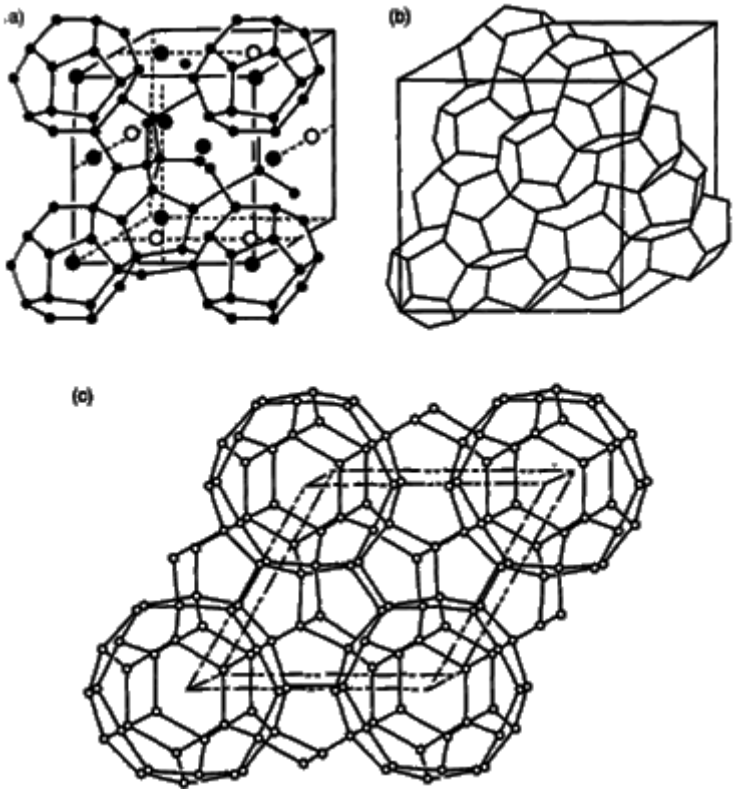

Figure 3-1: Unit cells of hydrate structure I(a), II(b) & H(c) (Sloan 1998).

More recently discovered hydrate structures include structure T (Udachin et al. 2001) and the high pressure methane structures MH-II and MH-III (Loveday et al. 2001). These are rarely found in the petroleum industry. The geometric properties of different types of hydrates are

summarized in the Table 3-A. SI is the simplest type of hydrate formed. This thesis concentrated on the SI hydrate for the simulation analysis. We shall now address this hydrate type in detail.

Table 3-A: Main geometrical properties of hydrate structure I, II and H (Modified from(Sloan 2003))

Hydrate structure	SI		SII		SH		
Cavity	small	large	small	large	small	medium	large
Cavity shape	round	oblate	round	round	round	Round	oblate
Cavity description	5^{12}	$5^{12}6^2$	5^{12}	$5^{12}6^4$	5^{12}	$4^3 5^6 6^3$	$5^{12}6^8$
Number/unit cell	2	6	16	8	3	12	1
Average radius (A)	3.91	4.33	3.902	4.683	3.91†	4.06†	5.71†
Rel. size of CH_4	88.6%	75.7%	88.9%	67.5%	88.6%	-	-
Coordination No.	20	24	20	28	20	20	36

†Estimates of structure H cavities from geometric models.

3.2 Structure I hydrate

As shown in Figure 3-2, SI is made from two types of cavities:

a) Dodecahedra, 12-sided polyhedra where each face is a regular pentagon;
b) Tetrakaidecahedra, 14-sided polyhedra with 12 pentagonal faces and 2 hexagonal faces.

Dodecahedral cages are smaller than the tetrakaidecahedral cages; thus the dodecahedra are often referred to as small cages, whereas tetrakaidecahedra as large cages (Carroll 2003).

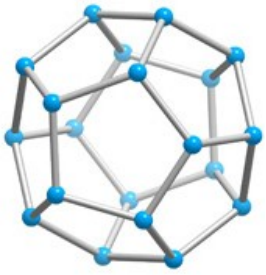

Dodecahedron 5^{12}

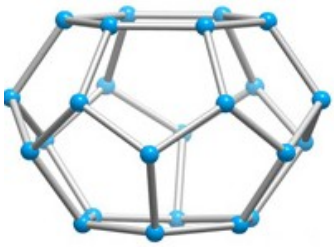

Tetrakaidecahedron $5^{12}6^2$

Figure 3-2: Structure I cavities (updated from (Jeffrey and McMullan 1967)

A unit cell of SI contain 46 hydrogen-bonded water molecules forming 2 small and 6 large cavities and encapsulating appropriate guest molecule. A guest molecule that does not compete or disturb with the already existing hydrogen bonding is needed to stabilize the cavity (Jeffrey 1984). Guest molecules with diameter between 4.2 Å – 6.0 Å stabilizes the cavities in SI. Hydrogen sulfide and methane molecule can occupy both small as well as large cavities of SI. Carbon dioxide and ethane are other guest molecules, which form SI hydrate. Ethane molecule can only enter the large cavity of SI hydrate.

It is known that CH_4 can stabilize the dodecahedron small cavity in all the hydrate structures (I, II & H), as well as the tetrakaidecahedron in SI. Since methane can stabilize both small and large cavities of SI hydrate and given its abundance in nature (Sloan 1998), this guest molecule will be used in the simulations presented in this thesis.

3.3 Thermodynamics of hydrate formation

"The most challenging and intriguing question regarding hydrates concern how hydrates form, dissociate, and are inhibited with time" (Sloan 1998). With the determination of hydrate structure, more definite predictive methods were formulated to predict hydrate thermodynamic properties. The groundbreaking theory of hydrate thermodynamics due to van der Waals and Platteuw's was derived from the fundamental principles of statistical physics.

The expression for the chemical potential of water in the hydrate phase (μ_w^H) is given by equation (3-1) below. This equation is derived from the semi-grand canonical ensemble under the constraints of water molecule number being fixed, corresponding to an empty lattice of the actual structure. Details of the derivation are given elsewhere (Kvamme and Tanaka 1995) and only the main equation for the chemical potential of water in hydrate is presented here:

$$\mu_w^H = \mu_w^{O,H} - \sum_i RT\, v_i \ln\left(1 + \sum_j h_{ij}\right) \qquad \textbf{(3-1)}$$

In this equation, $\mu_w^{O,H}$ is the chemical potential of water in an empty hydrate structure; h_{ij} is the cavity partition function of component j in cavity type i ; v_i is the number of cavities of type i formed per water molecule. For SI hydrate, there are 6 large cavities and 2 small cavity and hence $v_l = 3/23$ and $v_s = 1/23$; per 23 water molecules. The first sum in this equation

is over cavity types, and the second sum is over components j going into cavity type i. In this work, only one guest molecule type, namely methane, occupying the hydrates is considered and therefore the second sum will be reduced to a single term.

In its classical formulation of this equation (van der Waal & Platteuw), the cavity partition functions are integrated under the assumption that the number of water molecules is fixed and their interactions with the entrapped guest molecules are negligible. The water lattice is considered undisturbed by the presence of guest molecules. This approximation is valid for small guest molecules with weak interactions. However, large guest molecules like carbon dioxide in the large cavities of SI hydrate will have a significant impact on the librational modes of the water molecules in the lattice. Thus, the free energy of the water lattice will be affected. To consider the impact of guest inclusion molecule on the water lattice, a revised adsorption theory was proposed by Kvamme and Tanaka (1995). This alternative approach considers the guest motion away from the minimum energy position in the cavity as a spring, and evaluates the free energy changes through samplings of frequencies for different displacements. A small molecule like methane however, will not have significant impact on the water movements.

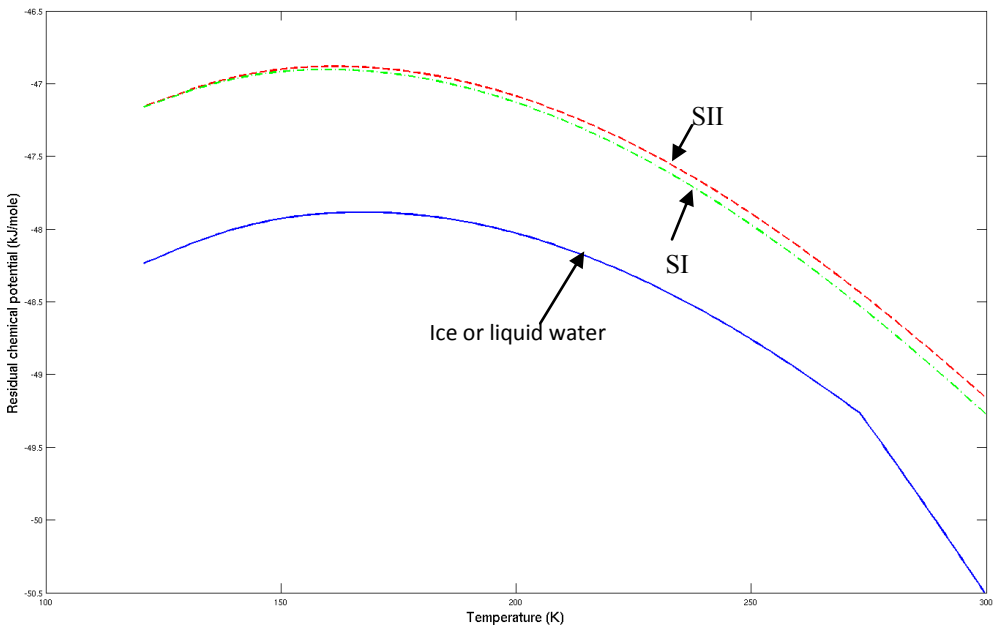

Figure 3-3: Residual Chemical potential for TIP4P model. Solid line for ice or water, dash line for SI empty hydrate and dash-dotted line for SII empty hydrate.

Kvamme and Tanaka (1995) calculated the chemical potential change with temperature for the TIP4P water model forming an empty clathrate lattice of SI and SII type. They showed

that the difference in chemical potential between the empty cavity of SI and SII hydrate is quite small and hence there is a possibility of formation of either of the SI or SII hydrate during the initial nucleation stage. Figure 3-3 illustrates these results. Below 180 K, they are no longer reliable due to the quantum mechanical effects becoming significant. In addition to the above, the structure of small cavity is identical for both SI and SII and larger number of small cavities are present in SII as compared to SI. Hence, both structures formation could be initiated during the nucleation process.

3.3.1 The Gibbs phase rule

A phase is a distinct region of material that is chemically uniform, physically distinct and (often) mechanically separable (Modell and Reid 1983). The Gibbs' phase rule (Gibbs 1928) is based on the fundamental principles of thermodynamics. It provides the theoretical foundation for characterizing the state of a system and makes it possible to predict the equilibrium relations of the phases present as a function of intensive variables such as pressure and temperature. Gibbs' phase rule is given by equation (3-2). In this equation, F is the number of intensive variables needed to specify the system (aka the number of the degrees of freedom); C is the number of components, and P' is the number of phases in the system.

$$F = C - P' + 2 \quad \textbf{(3-2)}$$

To understand the implication of this rule, let us consider the potential for hydrate formation from methane in gas phase and water in the liquid phase. Since the number of components are two, methane and water, $C = 2$, and there are three phases, liquid, gas and solid hydrate, $F = 1$, and thus only one intensive variable, such as temperature or pressure can be defined to achieve a unique solution for the formation of hydrates. A unique solution means that if the system is left to itself for long time, it could theoretically reach equilibrium (Sloan 1998). If equilibrium cannot be reached due to Gibb's phase rule, i.e. too many intensive variables are fixed, the hydrate containing system will not reach thermodynamic equilibrium but will still strive towards the lowest possible Gibbs energy (G).

3.3.2 Hydrate formation

For the hydrate to form (Makogon 1999) the following three conditions must be satisfied:

a) The process should be thermodynamically favorable ($\Delta G < 0$)
b) Access to hydrate forming constituents (water + hydrate former)

c) Heat transport during hydrate formation to remove latent heat of hydrate formation.

Labile clusters of hydrates form and dissociate until they reach a critical radius (r_c) beyond which a spontaneously cluster growth is achieved. The change in Gibbs free energy, ΔG can explain the formation and further growth of hydrate crystal (Sloan 1998). When a crystal is being formed, there are two competing processes.

1. The penalty(surface excess free energy, ΔG_s) , where the solute molecule is adsorbed to the crystal and become a part of the growing crystal thereby pushing the surrounding, as this new phase needs space.
2. The benefit (volume excess free energy, (ΔG_v) , which is the actual phase transition itself favored due to negative Gibb's free energy thereby making solute molecule to end up inside the crystal surface.

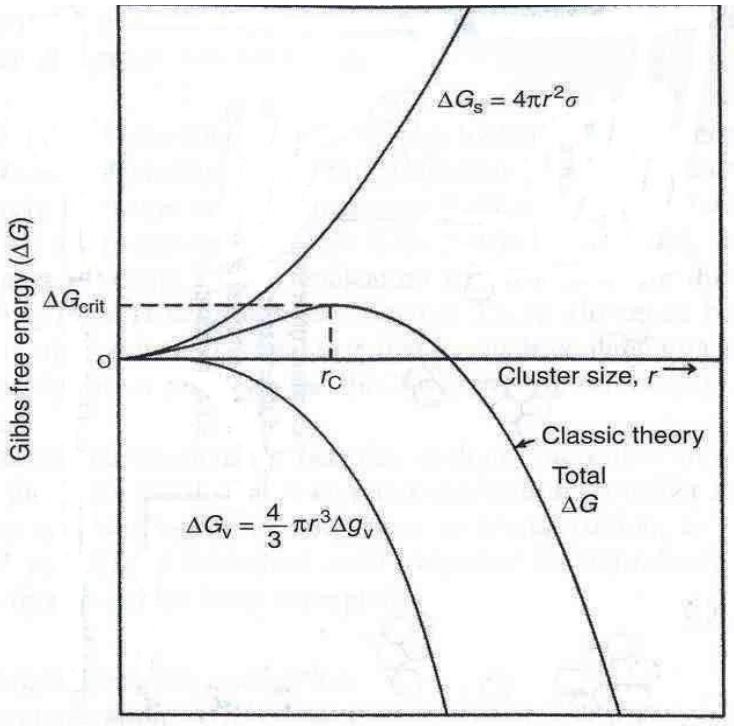

Figure 3-4: Gibbs free energy as a function of cluster size (Sloan & Koh, 2008)

The total change in Gibb's free energy for a spherical particle is given by:

$$\Delta G = \Delta G_s + \Delta G_V$$

Where,

$$\Delta G_s = 4\pi r^2 \Upsilon \qquad \textbf{(3-3)}$$

$$\Delta G_v = \frac{4}{3}\pi r^3 \Delta g_v$$

In equation (3-3), Δg_v is the free energy change per unit volume and Υ is the interfacial free energy of the sharp crystal-liquid interface (uniform properties outside interface).

Growth occurs spontaneously once the critical cluster size is reached where ΔG_v overcomes ΔG_s as shown in Figure 3-4. Depending on the ambient conditions, composition of gases, water and impurities present the range of temperature and pressure at which hydrate will form can be predicted. A typical Hydrate P-T Curve is shown in Figure 3-5.

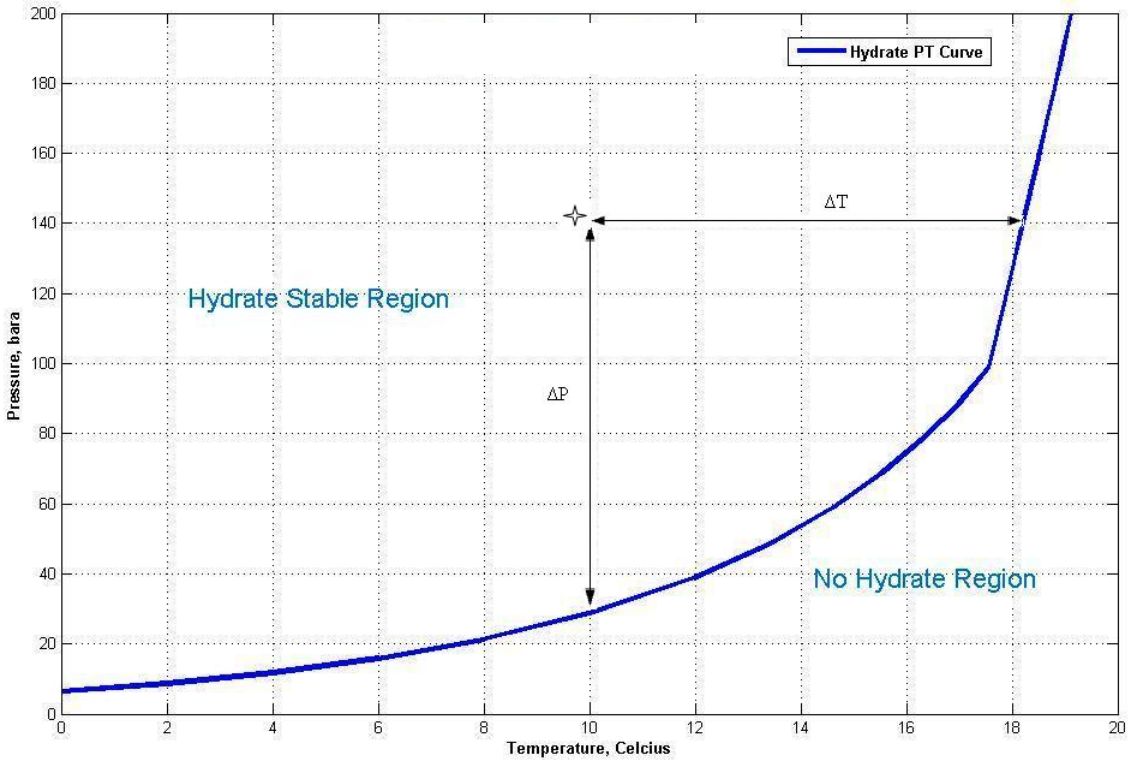

Figure 3-5: Typical hydrate P - T curve

This curve is the hydrate equilibrium curve. At the left hand side of the curve (Hydrate Stable Region), hydrate is thermodynamically stable and at the right hand side (No Hydrate Region) itself, no hydrate formation is thermodynamically possible. On the equilibrium line, hydrate can coexist with the hydrate former and the free fluid phase.

3.4 Nucleation

The initial stage of formation of a new phase from an old phase is nucleation (Kashchiev 2000). It is difficult to observe the nucleation step experimentally, since it is a microscopic phenomenon involving tens of thousands of molecules (Mullin 1993). In this thesis, the pre-

nucleation process at different concentration of methane in methane – water systems is studied at the microscopic level using molecular dynamic simulation.

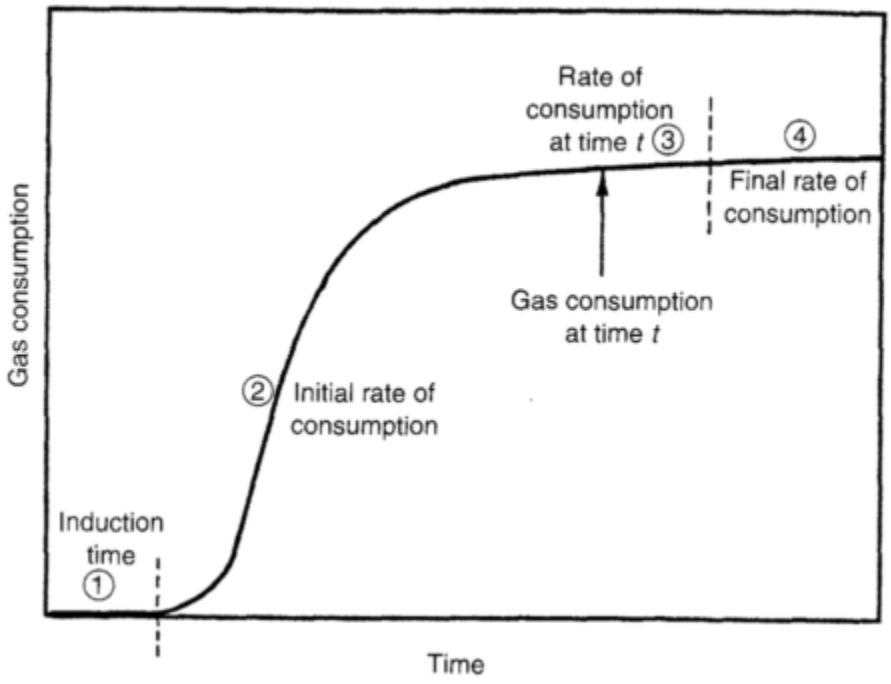

Figure 3-6: Gas consumption during formation of hydrates. Modified by (Sloan and Koh 2008) from (Lederhos et al. 1996).

Nucleation is the process up to the first stable nucleus is formed. It is typically in the nano size region and normally very fast (nanoseconds), provided thermodynamically high driving forces present. The critical nuclei size defines the size of this first stable nucleus, after which the net free energy is dominated by free energy gain. This particle will grow without decay unless competing with neighboring particles which may be in a state of lower free energy (Kvamme et al. 2004; Kvamme et al. 2007). The time elapsed from the moment the first nucleus of hydrate formed to the appearance of detectable amount of hydrate phase is called the induction time. Most of the experiments have been focused on the macroscopic stage of growth, defined as the interval after the induction time but before the onset of massive growth. The exact definition of induction time will obviously depend on the resolution of the experimental method employed and as such is not a well-defined physical term. Experiments depicted in Figure 3-6 used gas consumption to measure the induction time and monitor hydrate growth.

Depending on the conditions and phases present, two different types of nucleation are possible.

a) Homogeneous nucleation (HON) in which hydrate formation takes place in a single "parent" phase present without any impurities.
b) Heterogeneous nucleation (HEN) in which hydrate formation takes place in the presence of two or more phases, and/or impurities, which serve as nucleation catalysts.

HON is very unlikely to occur, as it is virtually impossible to achieve a pure phase free of impurities. In addition, the aforementioned special condition 'b' in section 3.3.2 , access to hydrate formers is limited.

3.4.1 Hydrate nucleation at the molecular Level

Molecular-level models of hydrate nucleation focus on the water – gas interface. There are various hypotheses concerning nucleation mechanisms, three of which are discussed below.

a) "Labile" cluster hypothesis (Christiansen and Sloan 1994) supporting HON is illustrated in Figure 3-7. This hypothesis proposes that under favorable conditions, water rearranges itself to forms clusters with no guest molecules encapsulated in it. (B) The water forms the labile cluster quickly around the dissolved guest molecule. (C) These clusters agglomerates by sharing faces thereby stabilizing the nucleation. (D) Once the cluster reaches critical radius during agglomeration, growth of hydrate begins.

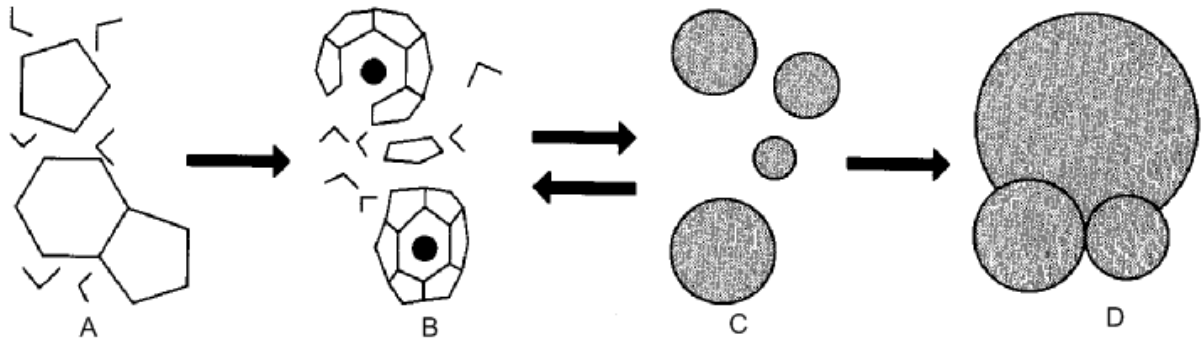

Figure 3-7: Labile cluster nucleation hypothesis. Modified from (Sloan and Koh 2008)

b) Another hypothesis supporting HEN, was put forward by (Long 1994) and (Kvamme 1996); it states that nucleation starts on the gas side of the interface and is illustrated in Figure 3-8. The hypothesis suggests that a gas molecule is transported from bulk to the interface, which is most favorable site for nucleation.

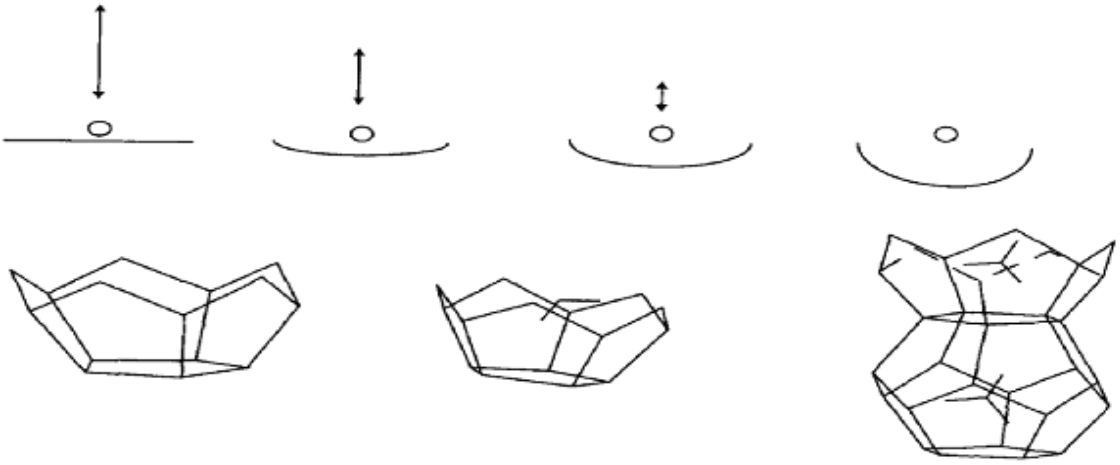

Figure 3-8: Adsorption of gas molecules onto labile hydrate cavities at gas - water interface. (Long 1994)

This gas molecule then is adsorbed to the most favorable site at the interface. The water molecule will reorient them around this guest molecule forming first partial and then complete cavities. Labile clusters will agglomerate and grow on the gas side of interface until the critical size is achieved. The mathematical model, based on statistical thermodynamics, has later been refined in (Kvamme 2000; Kvamme 2002). The hydrate growth on the gas side of interface is two times faster than on the waterside, thus hydrate growth on the gas side will dominate. In most real systems, the interface between water and the hydrate former is not flat (Kvamme 2002) but contains waves, pores, bubbles and hydrate nucleus of different size.

c) The third hypothesis, based on local structuring nucleation (HON), was suggested by (Radhakrishnan and Trout 2002). It states that thermal fluctuation causes the guest molecule to arrange in a manner similar to that in the clathrate hydrate phase. Water molecules around these locally ordered guest molecules will form small and large cages. The numbers of guest molecules, which are locally ordered, are more than that needed for critical nucleus. These cages agglomerate and dissociate until the critical size of the

hydrate cluster is formed. (Moon et al. 2003)also proposed the model similar to that of Radhakrishnan and Trout (2002); using MD simulations of methane hydrate nucleation at methane – water interface.

Kinetic rates calculated based on different hypotheses vary quite significantly and show that the exact mechanism of nucleation is still not clear. Since this nucleation takes place at micro level, it is difficult to follow its mechanism experimentally. To obtain insights into the hydrate nucleation phenomenon, MD simulations on methane – water system at different concentration of methane were performed in this thesis.

3.5 Hydrate inhibition

Hydrate formation can be prevented by shifting the condition from hydrate stable region (as shown in Figure 3-5) to no hydrate region. This can be done in two ways:

1. Physical Inhibition
2. Chemical Inhibition

3.5.1 Physical inhibition

Physical inhibition can be done by changing physical conditions of the system by either heating, reducing pressure or removing water from system.

a) Heating / Insulation:

If the flow conditions are in hydrate stable zone, they can be shifted by supplying heat, increasing temperature enough, and keeping the pressure constant, so that the mixture will be moved away from the hydrate stability region, and no hydrate formation will occur. This is illustrated in Figure 3-5, where ΔT represents heating at constant pressure and by moving on a straight line to the right from a point in the hydrate stable region, crossing the equilibrium line and ending up in a non-stable region thereby resulting in no hydrate formation. For short transport pipelines, proper insulation is appropriate but if the transportation occurs over long distance, this method will be very expensive.

b) Pressure Reduction:

As seen in Figure 3-5, ΔP line represents change in pressure. When mixture is in hydrate stable zone, pressure can be reduced at constant temperature to cross the hydrate equilibrium curve and thereby preventing hydrate formation. When pressure is reduced, gas expands and hence there is a temperature drop so heat needs to be provided to keep temperature constant. In addition, cost is involved for recompressing gas at the gas terminal.

c) Water Removal:

Water removal or water dew point lowering will decrease the hydrate formation and growth and if the process is operated above the water dew point temperature, formation of hydrate could be slowed. The gas is brought into contact with a hygroscopic solution like glycols to remove the dissolved water. Alternatively, selective adsorption of water is achieved by using molecular sieves, alumina or silica gel. In this dehydration process, operating costs are very high and hence chemical dosing inhibitors are preferred over this.

3.5.2 Chemical inhibition

Two classes of chemical inhibitors are as follows:

1. Thermodynamic Inhibitors
2. Low Dosage Hydrate Inhibitors.

3.5.2.1 Thermodynamic inhibitors

Thermodynamic inhibitors shift the hydrate P-T curve by changing the thermodynamic properties of the system. The effect of the inhibitor is both through the dilution of water and through the impact of the inhibitor on the water activity. Addition of thermodynamic inhibitors like methanol, ethanol, and salt, etc. makes liquid water more stable than hydrate water, since it reduces the chemical potential of aqueous water. The chemical potential for water in liquid state, μ_w^{liquid} is given in equation (3-4) below (Modell and Reid 1983)

$$\mu_w^{liquid} = \mu_w^{pureliquid} + RTln[x_w \gamma_w(T, P, \vec{X}^{liquid})] \quad \textbf{(3-4)}$$

Where $\mu_w^{pureliquid}$ is chemical potential for pure liquid water phase; R is universal gas constant; x_w is the mole fraction of water; γ_w the activity coefficient of water. T, P and $\vec{X}^{liquid}$ corresponds to temperature, pressure and liquid phase composition respectively.

By changing the chemical potential of liquid water, the equilibrium curve for hydrate can be shifted further left, and hydrate formation therefore prevented. The amount of thermodynamic inhibitor needed is usually high and hence the oil and gas industry is now focusing more on using less expensive low dosage inhibitors.

3.5.2.2 Low dosage hydrate inhibitors (LDHIs)

LDHIs do not influence the thermodynamics of the hydrate formation but influence kinetics and specifics of hydrate formation. Anti-Agglomerants and Kinetic hydrate inhibitors (KHIs) constitutes the two main classes of LDHIs. Both KHI and Anti-Agglomerants are added at low concentrations, often around 0.1–1.0 wt. percentage active concentration. This is in sharp contrast with 10–50 wt. % needed for thermodynamic inhibitors such as methanol, glycols or salts (Kelland et al. 2006).

Anti-Agglomerants are a class of surfactants and polymers that accelerate hydrate growth but in such a way that the polymer creates a non-polar coating surrounding hydrate crystal thus preventing further agglomeration of small hydrate crystals. Hence hydrate can be transported as a transportable non-sticky slurry of hydrate particles dispersed in the liquid hydrocarbon phase (Kelland 1994). For this method to be effective, a liquid hydrocarbon phase should be present.

Kinetic Hydrate Inhibitors interfere with the initiation and growth process, preventing the hydrate formation without shifting the hydrate equilibrium curve.

The next chapter focuses on Kinetic Hydrate Inhibitors.

4 Kinetic hydrate inhibitors (KHIs)

KHIs are special polymers and surfactants that delay the process of hydrate nucleation (and usually growth of hydrate crystals as well) long enough for the fluids to reach the process facilities without plugging the transport pipelines. The higher the driving force for hydrate formation (larger sub cooling), the shorter is the induction time of hydrate nucleation (Kelland et al. 2009). As opposed to Anti-Agglomerants, KHIs can also be used in the gas lines with no liquid hydrocarbon phase present. Many petroleum companies are working on developing the KHIs but most of the industrial research is confidential.

4.1 History and experimental results

In early 1970s, Kuliev and his co-workers performed laboratory experiments using various different surfactants (pure as well as mixtures) to study their effect on hydrate formation from natural gas. They observed that Alkyl aryl sulfonate gave the highest degree of sub cooling of 9.2 °C (Kuliev et al. 1972). The mechanism of surfactant inhibition was not well understood but they concluded that the more effective the mixture as a surfactant, the higher the sub cooling achieved for hydrate formation. This was the first published example of using a low dosage hydrate inhibitor.

Extensive history of LDHIs is presented in "History of the development of low dosage hydrate Inhibitor" (Kelland 2006). By the beginning of the 1990s, three institutes and three oil companies, namely The French Petroleum Institute (IFP), Colorado School of Mines (CSM), SINTEF, Shell, British Petroleum and ExxonMobil, were involved in the search for LDHIs.

The first discovery of KHI was done by CSM in 1991. After screening 750 substances for KHI properties in their Tetrahydrofuran (THF) hydrate ball-stop rig tests, they discovered that poly (vinylpyrrolidone) (PVP), delayed the formation and the agglomeration of THF hydrates (Long et al. 1994; Sloan 1995). Later they tested Gaffix VC-713 and PVCap and observed that these polymers outperformed PVP in the ball-stop test. PVCap delayed hydrate nucleation by 24 h for sub cooling up to 8 – 9 °C at the dosage of 0.5 weight percent. Shell tested PVP on a field trial in Michigan and in the Groningen field which showed that PVP works only for lower sub cooling and is not recommended for high sub cooling(above 10 °C)

fields (Klomp et al. 1997). Figure 4-1 below illustrates the chemical structure of different KHI.CSM also discovered that other polymers like polyvinylamides, polyalkyloxazolines etc. could act as synergists increasing the performance of PVCap as KHI (Sloan 1995; Sloan et al. 1997). Rogaland Research Project (RF) for Exxon Mobil in 1995 tested VIMA (N-methyl-N-vinylacetamide) as a 1:1 copolymer with VCap as shown in Figure 4-2 and concluded that it performed better than PVCap alone.

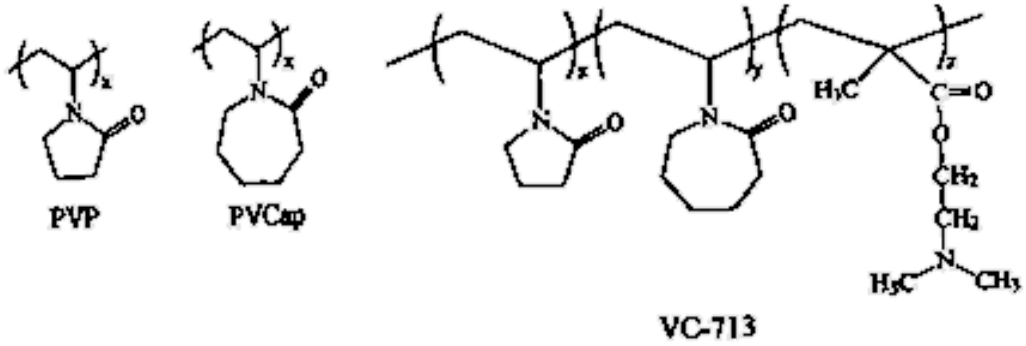

Figure 4-1: Chemical structure of hydrate inhibitors. (Lederhos et al., 1996)

They were of the opinion that a key element in many KHIs was the presence of amide group attached to hydrophobic group in repeating unit. The hydrophobic group will form hydrate cavities around it while the carbonyl oxygen will form hydrogen bonds with water molecules (Kelland 2006). However VIMA: VCap copolymer is no longer in use due to the high price and difficulty in getting monomers of VIMA.

By the mid-1990s, most of the classes of KHIs used today were discovered, although the clear picture of the mechanisms of KHI needed more research. (Kelland and Phillips 1999) showed that PVCap gave a higher sub cooling performance for SII compared to that of SI since SI is having relatively higher symmetry of hydrate crystals.

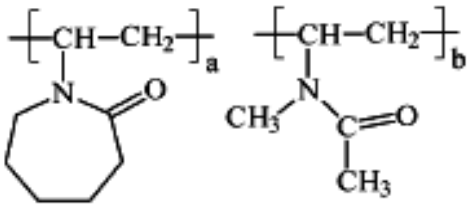

Figure 4-2: Structure of VCap: VIMA 1:1 copolymer. (Kelland, 2006)

By the end of the last millennium, most of the research work related to KHI was diminishing. Shell was still open for new LDHIs ideas and found that certain Polyesteramides performed well as KHI. They patented the results in 2002 (Klomp 2002), two field trials were carried out in 2004, and several applications have already begun. Polyesteramide KHI as shown in Figure 4-3 are commercially available today through Baker Petrolite which have found that their polyesteramide-based KHI have better performance on SI hydrates than other KHIs chemistries such as PVCap.

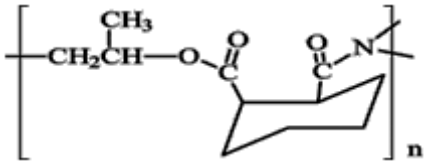

Figure 4-3: Repeat unit in a polyesteramide made from di-2-propanolamine & hexahydrophthalic anhydride. (Kelland 2006)

To investigate the effect of KHI in emulsions, a group at CSM used differential scanning calorimetry (DSC) (Lachance et al. 2009) to measure emulsions characteristics such as droplet size distribution, emulsion stability, and mass transfer through the dispersion (Dalmazzone et al. 2006). The micro–differential scanning calorimeter (μ-DSC VIIa, Setaram Inc.) can be used to measure thermal properties of hydrates and ice at the pressure ranging from 0.1-40 MPa and temperatures between 228 and 393 K (Setaram 2003). In this experiments, PVCap (i.e. PVCap, BASF 6214 Luvicap) was added to de-ionized water at concentrations of 0.2, 0.5 & 1 weight percent of the total emulsion (0.7, 1.6, 3.2 weight percent in water). Then the water-in-oil emulsified samples were prepared using a cyclone IQ2 microprocessor controlled homogenizer (Virtris Co). Further details of sample preparation and mode of operation is described elsewhere (Lachance et al. 2009).

The 50 experimental results at different concentrations of PVCap shown in Figure 4-4 indicate that PVCap is proved effective in delaying the hydrate induction time in an emulsified system.

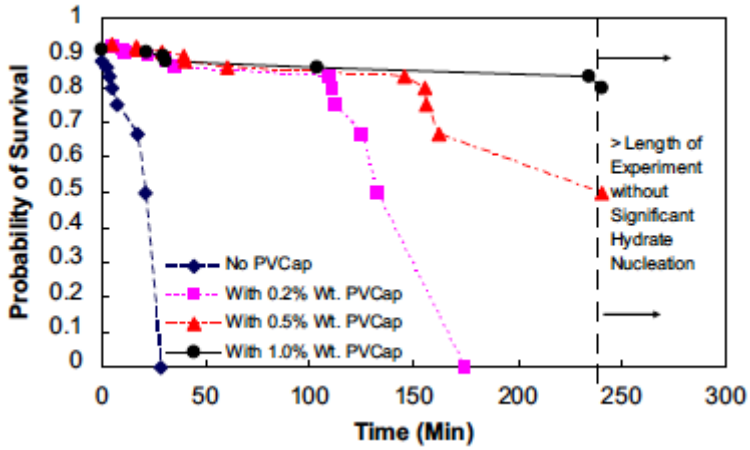

Figure 4-4: With increased concentration of PVCap, the probability of hydrate nucleating decreases. (Lachance et al. 2006)

As demonstrated in Figure 4-5, varying PVCap concentrations from 0.2, to 0.5 and 1.0 weight percent had little effect on the width of the hydrate formation peak. This may have to do with the way KHI is dispersed throughout the droplets. "Although many of the droplets nucleate independently, the propagation of hydrate reduces the effect of the increased inhibitor concentration" (Lachance et al. 2009). Hence increasing the concentration of PVCap is effective in delaying the initial induction time but does not affect the width of hydrate formation.

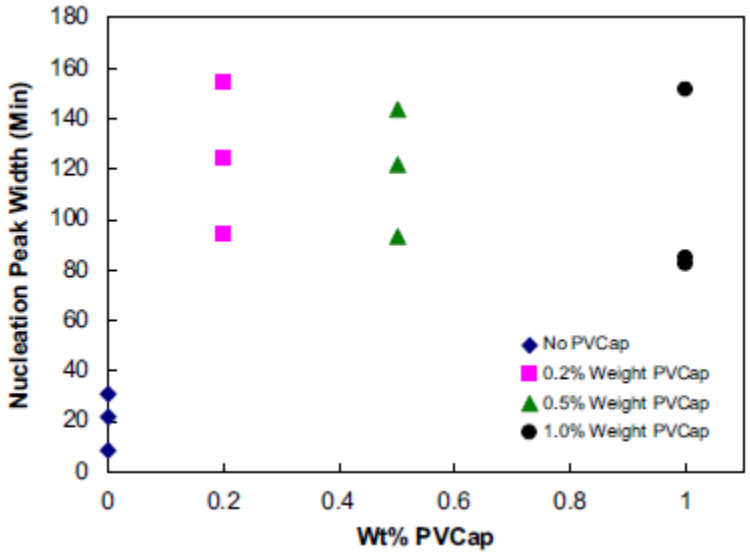

Figure 4-5: Effect of varying PVCap concentration on the width of hydrate formation peak in the DSC. Measurement taken from onset of nucleation to top of hydrate formation peak (Lachance et al. 2006)

In order to confirm this hypothesis, additional study was needed either with different oil samples able to keep the droplets segregated, or reducing the water cut to only 5 – 10% instead of 30 wt% (used in above experiments) to reduce the communication between droplets. The results from this investigation thus showed that PVCap was able to increase both the average nucleation time of hydrates and the stochastic nature of hydrate nucleation in an emulsion.

Through several experiments, it was clear that KHIs delays the growth of hydrate formation but how these KHIs delay the process of nucleation and further growth was not well understood. There was a need to develop a theoretical understanding of the kinetic hydrate inhibition. Thus, theoretical investigations were started aiming to pinpoint the mechanism of inhibition by KHIs.

4.2 Theories and mechanisms

Several different hypotheses explaining the working of KHIs has been suggested. Following is the discussion of theoretical approaches suggested by leading hydrate research groups.

4.2.1 The Massachusetts Institute of Technology (MIT)

The MIT group proposed that hydrate inhibition occurs via the following two-step mechanism (Anderson et al. 2005):

a) Inhibitor molecules disrupt the local organization of the water and guest molecules, increasing the barrier to nucleation and nuclei propagation.
b) Once nucleation occurs, the inhibitor binds to the surface of hydrate nanocrystal and retards further growth along the bound growth plane.

In the first step, the disruption of newly forming nuclei occurs as proposed by (Storr et al. 2004) They found that the hydrophilic group of a new KHIs, tributylammoniumpropylsulfate, enhances the water structure in the mid-long range, but in a way that is incompatible with the hydrate ordering, thus preventing hydrate formation.

The step 2 of the mechanism proposed is based on the experimental observation by several groups (Makogon et al. 1997; Larsen et al. 1998; Sakaguchi et al. 2003; Storr et al. 2004)

who found that addition of PVP and PVCap gave rise to plate-like hydrate crystals. Thus, KHIs adsorbing on the hydrate surface will retard any further growth in that direction and leave only the possibility of growth in other directions. (King et al. 2000) experiments show that a non-inhibitor, poly (ethylene oxide) is not adsorbed on hydrate surface in contrast to PVP, PVCap & VIMA which adsorbs on hydrate surface, further supporting the surface binding hypothesis. Based on these results, it was proposed that the stronger the KHI binds to the hydrate surface, the more disruptive the inhibitor is to the structure of forming hydrate nuclei.

4.2.2 The University of Warwick group (UOW)

Recently the UOW researchers has suggested that it is the surface energy effect of the PVP oligomers that is responsible for their inhibition effectiveness (Moon et al. 2007). They compared the PVP results with those from their earlier study for PDMAEMA, Poly (dimethylaminoethylmethacrylate) (Hawtin and Rodger 2006). This work hypothesized that PVP inhibits hydrate formation by increasing the surface energy of the interfacial region, whereas PDMAEMA inhibits by adsorbing to the surface of hydrate nanocrystal. PVP is present in the interfacial region without binding irreversibly to the hydrate crystal. The inhibition caused by PVP can be explained as follows:

1. Transient filaments of hydrate water molecules are formed, starting from the pyrrolidone groups. Several filaments can form on the same oligomer but they are mostly inconsistent with each other and so prohibit, rather than reinforce, hydrate formation.

2. Halo region is created around the hydrate due to initiation of transient filaments around the hydrate cluster. The inconsistent filaments arising from the PVP disrupt this halo region. The halo effect caused by the insertion of PVP forms a viable mechanism to explain the kinetic inhibition of hydrate formation.

4.2.3 The University of Bergen (UIB)

Kvamme et al. (2005) at the UIB suggested a theory based on interactions between hydrate water and inhibitor (Kvamme et al. 2005). It was proposed that stronger the interaction between inhibitor-hydrate water, the higher the inhibition efficiency. Several inhibitors like

PVP, PVCap and VC-713 were studied. Based on the analysis, the following conclusions were drawn:

A. Both PVP and PVCap have the tendency to position themselves at hydrate – liquid interface & form hydrogen bonds between hydrate water and carbonyl oxygen, thus potentially inhibiting further growth.

B. PVCap will outperform PVP as KHI since the potential energy of the inhibitor – hydrate interactions was significantly lower for PVCap then for PVP with both Coulomb and Lennard – Jones contributions favoring PVCap over PVP.

Later a hypothesis was put forward suggesting that the PVP will reduce the contact area and limit the mass transport between water and hydrate former causing further delay in hydrate formation and growth (Kvamme and Asnes 2006). To explain this, the initial system at conditions unfavorable for hydrate formation is indicated to the left side of Figure 4-6 and the right side indicates the onset of nucleation when the system is brought in hydrate stable region by either cooling or pressurization.

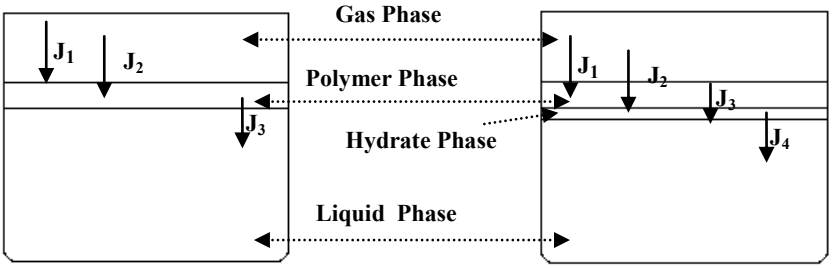

Figure 4-6: Left: Prior to hydrate formation, Right: After hydrate formation, (J is for flux).

In this hypothesis, PVP is assumed to form a separate phase by creating a layer in-between the water and the gas phase. Diffusion of hydrate former through the polymer phase was thus suggested as a limiting factor in the hydrate formation process.

5 Computational methods

Scientific method is the technique used to investigate a hypothesis through, observations and testing, acquire new knowledge or correct and integrate previous knowledge (Bauer 1994).

Typical apparatus used for testing KHIs are rocking cell chambers, flow loops, autoclave cells, Magnetic Resonance Imaging, etc. In order to get sufficient statistics, many time-consuming experimental runs need to be performed. Another important limitation of experimental approach is due to the fact that it is impossible to access all the time scales of motion with atomic resolution. Computational methods are often used to simulate theoretical models as well as to provide insights to experimentalists for further investigations. Large-scale experiments frequently employ computer simulations to analyze their potential outcomes. This branch of science thus helps both theorists and experimentalists to go beyond their inherent limitations.

Molecular Dynamics (MD) is the powerful simulation method used to explore the behavior of solids, liquid and gases by analyzing their motion through the calculation of forces acting on the model systems (atoms, molecules etc.). This approach is well suited for simulations of flexible molecules, mixtures interacting by force field in a periodic boundary cell. Once sufficient information on the motion of the model system in the phase space (coordinates plus momentum) is gathered, it becomes possible to investigate the detail mechanisms related to these properties and compare them with theory and experiment. Bulk properties like the structure; thermodynamics, etc. can also be calculated through statistical mechanics. In this thesis, we aimed to obtain insights into a nucleation process with and without KHI and understand how KHI delays nucleation at molecular level by means of an extended version of md43 package to run the simulation. This package was originally written by (Lyubartsev and Laaksonen 2000) and later modified to add support for quaternion treatment of molecules, pdb and dcd output (Kuznetsova 2001). Visual Molecular Dynamics (VMD) (Humphrey et al. 1996) was used to visualize the motion of molecules and analyze the data. The molecules used for simulation needs to be modeled correctly to reproduce the reality. The charges on the PVCap need to be appropriate, as they will strongly affect the system's behavior. Quantum mechanics (QM) describes the molecules and atoms at the atomic and subatomic (electrons,

protons) level. Hence, the partial atomic charges on PVCap were estimated using quantum mechanics techniques. The next sections will give the overview and describe more QM and MD in detail.

5.1 Quantum mechanics

The basic theory of quantum mechanics can be used to explain not only the structure and properties of atoms, molecules and solids, but also those of nuclei and of 'elementary' particles such as protons and neutrons (Rae 2002). Quantum mechanics explicitly account for electrons in calculations. This makes it possible to derive properties that are dependent on the electronic distribution. A wave function Ψ(position, time) is a fundamental concept of quantum mechanics. Its square gives the probability distribution of the particle being at a given point in space at a given time.

5.1.1 The Schrödinger equation

A central problem of quantum mechanics is calculating the wave function Ψ for any system of interest (McQuarrie 2000). The Schrödinger equation must be solved to find this wave function. The time-independent form of the Schrödinger equation is given by:

$$\widehat{H}\Psi = \mathrm{E}\Psi \qquad \textbf{(5-1)}$$

Where, $\widehat{H}$ is Hamilton operator, and E is a scalar quantity corresponding to the total energy of the system.

5.1.2 Basis sets

Molecular orbital (MO) is a mathematical function describing the electron cloud surrounding the molecule. As shown in Figure 5-1, the MO is most commonly represented by a linear combination of atomic orbitals (LCAO). Basis sets are used to approximate MOs. Any unknown arbitrary function, like MO can be rigorously expanded as a sum of known basis-set functions if the basis set is complete. However, the smaller the basis set used, the poorer is the representation. The accuracy of MO approximation is also influenced by the type of basis set used (Jensen 2007).

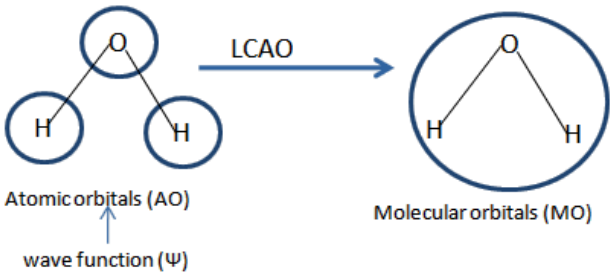

Figure 5-1: Linear combination of atomic orbital (The Shodor Education Foundation 1999-2000).

Primitive functions most commonly used in basis sets are Slater Type Orbital (STO) and Gaussian Type Orbital (GTO). STO sets require more calculations, take longer time and are more accurate than GTO. However, it is possible to reproduce the STO accuracy by combining several GTOs. As the number of GTOs combined increases, the modeling of STO equation gets better. When using GTO to model STO, the equations are identified as STO-NG equations where the number "N" before "G" is the number of Gaussian primitives (GTO) used to simulate the STO equation. The basis set equation of this form with STO-NG, describes only the most basic aspects of the orbitals and are considered the "minimum" basis sets. For example, in STO-3G, 3 GTOs will be used to mimic one STO. Commonly used minimal basis sets are STO-3G, STO-4G, STO-6G, etc. The "extended" basis sets are the ones that consider the higher orbitals of the molecules. Minimum basis set describes the broader features of the molecules whereas the extended basis sets are fine-tuning this description.

Split–Valence basis sets are a further improvement on the minimum basis sets. Since it is the valence electrons, which principally take part in the bonding, and it is therefore common to represent valence orbitals by more than one basis function to recognize this fact. Each of the basis function can in turn be composed of a fixed linear combination of primitive Gaussian functions. Minimum basis sets are fixed and are unable to adjust to different molecular environments. Since the different orbitals of the split have different spatial extents, their combination allows the electron density to adjust its spatial extent appropriate to the particular molecular environment. The justification behind this approach is that, it would be extremely tedious to calculate the expression for every single atomic orbital. Instead, by combining an expression for atomic orbitals, which are larger and smaller than the orbital of interest, we can approximate the orbital we are looking for. This method requires the combination of two or more STOs in order to describe an orbital. Since the different orbitals of the split have

different spatial extents, the combination allows the electron density to adjust its spatial extent appropriate to the particular molecular environments. Basis sets in which, there are multiple basis functions corresponding to each atomic orbital, including both valence orbitals and core orbitals are called valence double, triple, quadruple-zeta, etc. basis sets.

Some of the split-valence basis sets developed by the group of John Pople are STO-3-21G, STO-6-311G. In STO-3-21G, the number 3 stands for the 3 Gaussian primitives used to calculate the s-shell, the number 2 represents the number of GTOs for one of the sp-shells and the number 1 represents the number of GTO for the other sp-shell. In this case, the presence of two numbers [2 and 1] after the hyphen indicates, that this basis set is a split-valence double-zeta basis set.

When the two atoms or molecules are brought close to each other, it results in their polarization. This polarization effect accounts for the d and f-shells that are derived by adding STOs of higher orbital angular momentum. The asterisk '*' is the symbol denoted to account for polarization. One-asterisk accounts for the d-shell and two asterisks symbolize the f-shell. Standard polarization basis sets are STO-3-21G* and STO-6-31G*. Another common addition to basis sets is the addition of diffuse function, denoted by the addition of a plus sign '+', to the basis set designator, for example, 6-31+G. A double plus sign (6-31++G) indicates that the diffuse functions are also added to light atoms, like hydrogen's. Diffuse functions are useful when dealing with anions, systems in an excited state and system with some significant negative charge attached to it.

To do the geometry optimization of the PVCap model in vacuum, STO-3G/STO-3-21G/STO-6-31+G** basis sets were used.

5.1.3 Density functional theory

The wave function Ψ is a quantity, which is experimentally inaccessible. The treatment based on this will quickly reach an unmanageable size for system containing many atoms and many more electrons. Electron density can rather provide complete information needed about atomic and molecular system for instance where the nuclei are and how many electrons are in the molecule. Density functional theory (DFT) is used to investigate the electronic structure of

atoms and molecules. It is a type of Self Consistent Field (SCF) method where the orbital equations have to be iterated until self-consistency is achieved. DFT is based on the Hohenberg-Kohn theorem (Hohenberg 1964), which states that the exact energy of a system can be expressed as a functional depending only on the electron density. The total electronic energy as a function of the electron density ρ can be expressed as:

$$E_{DFT}(\rho) = T_S(\rho) + E_{ne}(\rho) + J(\rho) + E_{xc}(\rho) \quad \textbf{(5-2)}$$

Where, $T_S(\rho)$ is kinetic energy, $E_{ne}(\rho)$ is the electron-nuclear interaction term, $J(\rho)$ is the electron-electron Coulombic energy and $E_{xc}(\rho)$ contains the exchange and correlation contributions. All the electron-electron interactions are thus contributed by J and E_{xc} terms (Jensen 2007). The crucial problem with DFT is that the exact functional for exchange and correlation are not known except for the free electron gas. Hybrid functional approximates to the exchange-correlation energy functional in DFT.

QM calculation employed in this thesis used hybrid exchange correlation function called Becke, three-parameter, Lee-Yang-Parr (B3LYP). Becke stands for the exchange part and Lee, Yang and Parr for the correlation part. The B3LYP method is defined by the following equation (Becke 1993; Stephens et al. 1994).

$$E_{xc}^{B3LYP} = (1-a)E_x^{LSDA} + aE_x^{exact} + b\Delta E_x^{B88} + (1-c)E_c^{LSDA} + cE_c^{LYP} \quad \textbf{(5-3)}$$

Where, E_x^{LSDA} and E_c^{LSDA}contributes to the exchange and correlation part respectively of Local spin density approximation (LSDA); E_x^{exact} is for exact energy from Hartree-Fock theory; E_x^{B88} is the exchange correction to LSDA proposed by Becke and E_c^{LYP} for Lee, Yang and Paar electron correlation functional. Parameters a, b, and c are determined by fitting to experimental data with typical values being a~0.2, b~0.7 and c~0.8.

5.1.4 Continuum solvation models

Most chemical processes occur in presence of solvent and hence it is important to consider the effect of solvent on the behavior of the system. In some cases, solvent molecules are so tightly bound that they become the integral part of the system. In some other cases, the solvent does not explicitly interact with solute but it provides the environment that strongly affects the nature of solute. In the third case, solvent can merely act as “bulk medium” but can still

significantly influence the solute behavior with the dielectric properties of the solvent being of particular importance. The solvent acts as a perturbation on the gas-phase behavior of the system. This is the basic assumption of the 'continuum' solvent models (Smith and Pettitt 1994), where, the solute is assumed to be inside a cavity of appropriate shape and dimension within an infinite continuum dielectric resembling the solvent (Mennucci and Cammi 2007). The solvation free energy, the energy change due to transfer of molecule from vacuum to solvent is calculated in continuum models. A considerable variety of the continuum models have been proposed, for use with both quantum mechanics and empirical models. The discussion here will be restricted to 'Solvation Model 6' (SM6) as the software package used in this work (Jaguar) utilizes SM6 for treating solvated PVCap model.

SM6 calculates the aqueous solvation free energy, which is separated into two different components: The one arising from long-range bulk electrostatic effect and second from short-range interactions between the solute and solvent molecules in the first solvation shell (Kelly et al. 2005). Water is the solvent used in SM6. In this thesis, this solvation model was used to do the single point energy calculation with STO-6-31+G** basis set and subsequently to calculate the partial charges on solvated atoms of PVCap dodecamer. Partial atomic charge is not a quantum mechanical observable and therefore there is no formally "correct" method for assigning charges on atoms in molecule (Storer et al. 1995). SM6 uses Löwdin population analysis (LPA) utilizing the defined basis sets to perform the first partial charges estimate, and then applies the repartition of the diffused part of electron density using Redistributed Löwdin population analysis (RLPA). The final partial charges are obtained by means of Charge Model 4 (CM4), which empirically maps atomic charges obtained from LPA or RLPA.

5.1.5 Partial atomic charges

Löwdin's method proposes a prescription for partitioning the electron density into atomic contributions. It tries to eliminate the arbitrariness of equal partitioning of overlap density by transforming to a uniformly orthogonalized basis before the population analysis is carried out (Thompson et al. 2002). In this method, the partial atomic charges assigned are sensitive to basis set size and often predicts unphysical charges in case of extended basis sets that includes diffuse function like 6-31+G*. This is due the fact that large or diffuse basis set on a given

atom can mathematically describe electron density on neighboring atoms. LPA has also been found to exhibit rotational dependency and predicts non-equal population for equivalent atoms, if, the later are oriented differently. The dipole moments predicted by LPA were found to be more accurate than those predicted by Mulliken's approach. The Löwdin charge, q_k (Löwdin), on an atom k is given by:

$$q_k(Löwdin) = Z_k - \sum_{i \in k} (S^{1/2} P_e S^{1/2})_{ii} \quad \textbf{(5-4)}$$

Where, Z_k is nuclear charge on atom k, P_e is the electron density matrix, $S^{1/2}$ is the square root of the overlap matrix, and the summation index i runs over all basis function centered on the atom k. When the diffuse basis set like 6-31+G* is used, the second term in equation (5-4) can be readily partitioned into a contribution from orthogonalized tight basis function and contribution from orthogonalized diffuse basis functions. To correct for the fact that these diffuse basis functions carry excess charge that perhaps should not be assigned to the atom k, this charge will be redistributed to other atoms based on the diffuseness of the function in question and on the geometry of the molecule. This redistribution method is called as Redistributed Löwdin population analysis (RLPA).

Charge Model 4 (CM4) has been designed to map the charges obtained from LPA (in case of one-electron basis sets without diffuse function used) or RLPA (in case of diffuse basis set) to accurately reproduce experimental dipole moments (Olson et al. 2007). The charges, ${q_k}^1$on atom k for the CM4 model are mapped using equation (5-5) below.

$${q_k}^1 = q_k + \sum_{k \neq k'} {T'}_{kk'}(B_{kk'}) \quad \textbf{(5-5)}$$

Where, q_k is the input from LPA / RLPA partial atomic charges, ${T'}_{kk'}$ is a quadratic function of the Mayer bond order ($B_{kk'}$). The Mayer bond order is a function of one-electron basis set.

$${T'}_{kk'}(B_{kk'}) = (D_{Z_k Z_{k'}} + C_{Z_k Z_{k'}} B_{kk'}) B_{kk'} \quad \textbf{(5-6)}$$

The values of $C_{Z_k Z_{k'}}$ and $D_{Z_k Z_{k'}}$ are the CM4 parameters and these parameters depends on choice of the charges (LPA/RLPA/Mulliken) used to generate the initial q_k charges, the density functional, and the one-electron basis set. Note that in the original paper by (Olson et

al. 2007) the above equation (5-6) (equation number 2 in the paper) has a typo error where the term $C_{Z_k Z_{k'}}$ is written as $C_{Z_k} Z_{k'}$.

5.2 Molecular dynamics

Molecular dynamics (MD) is a type of computational simulation used to mimic the behavior of atoms and molecules at micro level (Leach 1996). In its simplest form, MD considers a box consisting of N number of particles and calculates their relative positions ($\overrightarrow{x_i}$), velocity ($\overrightarrow{v_i}$) and acceleration ($\overrightarrow{a_i}$) using Newton's second law of motion. Integrating equation (5-7), in which m_i is the mass of atom, yields position and velocity of each atom at any given time. The forces $\overrightarrow{F_i}$ are derived from a potential energy U (x^N) where $x^N = (x_{1,} x_{2,\ldots} x_N)$ represents the complete set of 3N atomic coordinates.

$$\overrightarrow{F_i} = m_i \overrightarrow{a_i}$$
$$-\frac{\partial U}{\partial x_i} = \overrightarrow{F_i} \qquad \textbf{(5-7)}$$

To calculate the trajectory, the initial positions of the atoms along with initial distribution of velocities and acceleration need to be defined. These initial velocities for all the atoms are reasonably assigned using Boltzmann distribution.

5.2.1 Verlet algorithms

There have been numerous algorithms for integrating the equation of motion. Verlet algorithm (Verlet 1967) is one of the most widely used one. This algorithm can be derived using Taylor expansion of $\overrightarrow{x_i}$ (t) for particle *i* from time t to t + δt and t – δt as shown in equations below.

$$\overrightarrow{x_i}(t + \Delta t) = \overrightarrow{x_i}(t) + \left(\frac{d\overrightarrow{x_i}}{dt}\right)_t \Delta t + \frac{1}{2}\left(\frac{d^2\overrightarrow{x_i}}{dt^2}\right)_t (\Delta t)^2 + \cdots \qquad \textbf{(5-8)}$$

$$\overrightarrow{x_i}(t - \Delta t) = \overrightarrow{x_i}(t) - \left(\frac{d\overrightarrow{x_i}}{dt}\right)_t \Delta t + \frac{1}{2}\left(\frac{d^2\overrightarrow{x_i}}{dt^2}\right)_t (\Delta t)^2 + \cdots \qquad \textbf{(5-9)}$$

Combining equation (5-8), (5-9) and assuming that third order and higher terms are negligible we get the prescription for finding new positions at time $t + \Delta t$ from position obtained from previous steps.

$$\overrightarrow{x_i}(t + \Delta t) = 2\overrightarrow{x_i}(t) - \overrightarrow{x_i}(t - \Delta t) + \left(\frac{d^2\overrightarrow{x_i}}{dt^2}\right)(\Delta t)^2 \quad \textbf{(5-10)}$$

This is known as Verlet algorithm. The final form of Verlet algorithm contains no explicit velocities $\overrightarrow{v_i}(t)$, but they can be obtained from the finite difference formula(Hinchliffe 2008).

$$\overrightarrow{v_i}(t) = \frac{\overrightarrow{x_i}(t + \delta t) - \overrightarrow{x_i}(\mathrm{t} - \delta \mathrm{t})}{2\delta \mathrm{t}} \quad \textbf{(5-11)}$$

This algorithm uses positions and accelerations at time t and the position at time t - Δt to calculate a new position at time t +Δt. These values need to be stored for each iteration. Verlet algorithm is time reversible and conserves the energy well even for long time steps.

5.2.2 Canonical ensemble

Canonical Ensemble is an ensemble whose thermodynamic state is characterized by a fixed number of atoms, N, a fixed volume, V, and a fixed temperature, T. The function Ω_{NVT} is the central statistical thermodynamic function of the canonical ensemble and is called canonical partition function (McQuarrie 2000).

$$\Omega_{NVT} = \sum_{j=1}^{N} e^{-E_j(N,V)/k_B T} \quad \textbf{(5-12)}$$

Where, k_B is the Boltzmann constant and E_j's are the energy states of an N-body system.

This partition function serves as a bridge between the quantum mechanical energy states of a macroscopic system and the thermodynamic properties of that system. Helmholtz free energy A is the thermodynamic function in the canonical ensemble and can be written in terms of Ω_{NVT} from statistical mechanics as:

$$A = -k_B T \ln \Omega_{NVT} \quad \textbf{(5-13)}$$

The temperature of the system is related to kinetic energy as exemplified in equation (5-14) for translational energy, from statistical thermodynamics. A number of thermostat methods are available to add and remove energy from the boundaries of an MD system in a realistic

way, approximating the canonical ensemble. The simplest way to control the temperature of the system is velocity scaling. In this method, the particle velocities are scaled up and down to keep the temperature constant. This method however will in general not give true canonical partition function.

$$\frac{1}{2}m_i\vec{v}_i^2 = \frac{3}{2}k_BT \tag{5-14}$$

The criteria for a theoretically acceptable thermostat is that the molecular dynamics simulation should capture the Boltzmann distributions over energy states involved in the canonical partition function in equation (5-12) (the requirement of ergodicity). It is still not verified that any of the simpler control algorithms like that of Nosé (Nosé 1984) and the simplified real time formulation due to Nosé-Hoover (Nosé 1991) is ergodic. However, a better approximation of canonical ensemble is achieved by using Nosé-Hoover thermostat.

5.2.3 Periodic boundary conditions

With the help of periodic boundary conditions (PBC) a simulation can be performed using relatively small number of particles, in such a way that the particles experiences forces similar to that in bulk fluid avoiding the influence of container walls (Leach 1996). A two-dimensional box is shown in Figure 5-2. Due to PBC, in two dimensions, each box will be surrounded by 8 neighbors; in three dimensions, each box will have 26 replicated nearest neighbors.

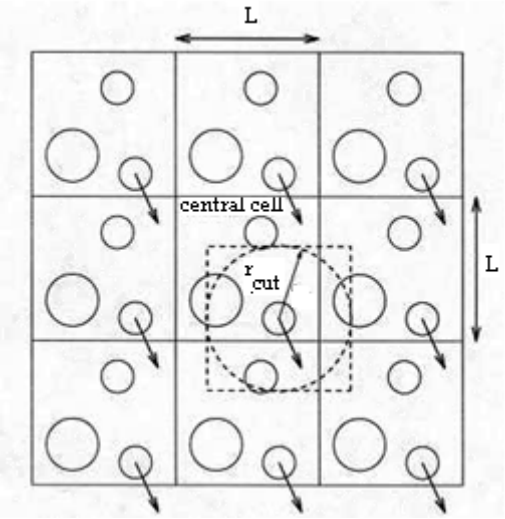

Figure 5-2: Periodic boundary conditions in two dimensions (Førrisdahl 2002).

Thus, the particle leaving the box during simulation will reappear at the opposite side of the primary cell with velocities identical to the one leaving. In this way the number of particles, N will remain constant in the simulation box.

5.2.4 Molecular interactions

Molecular interactions includes various types of intermolecular and intra molecular interactions between atoms and molecules. Atoms and molecules repel each other when they are too close and attract when they are far apart whereas they are stable at equilibrium bond length between them (Dill et al. 2003).Non-bonded molecular interactions are treated using Lennard-Jones potential while the electrostatic interactions are treated using long range Coulombic forces.

5.2.4.1 Bond stretching

Bond stretching is the oscillatory motion of two bonded atoms relative to each other. This motion consist of the two bonded atoms stretching passed their equilibrium position, then returning to their equilibrium position, and finally contracting passed their equilibrium position (Baird and Cann 2004).

Figure 5-3: Bond stretching.

As represented by the Hooke's law, each bond stretch between atom types A & B contributes to the total molecular potential energy (U_{AB}) . In equation (5-15), K_{AB} is the force constant, l_{AB} the instantaneous bond length and $l_{e,AB}$ the equilibrium bond length (Hinchliffe 2008).

$$U_{AB} = \frac{1}{2} K_{AB} \left(l_{AB} - l_{e,AB}\right)^2 \qquad \textbf{(5-15)}$$

5.2.4.2 Angle bending

All molecules having three or more atoms possess bending vibration. Bending vibration is an oscillation between two atoms A and C bonded to a common atom B but not bonded to each other. Such motion alters the ABC bond angle from its average value.

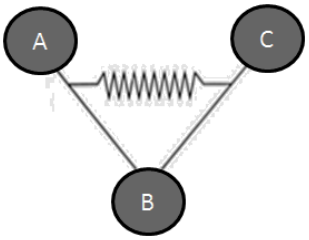

Figure 5-4: Angle bending

For the connected atoms A-B-C as shown in Figure 5-4, the potential energy contributions (U_{ABC}) as used in md43 code can be given by equation (5-16).

$$U_{ABC} = \mathrm{K}_{ABC}\left(\theta_{ABC} - \theta_{e,ABC}\right)^2 \quad \textbf{(5-16)}$$

Where K_{ABC} is the force constant, θ_{ABC} is angle made by atoms A-B-C and subscript 'e' refers to equilibrium.

5.2.4.3 Dihedral motion

Dihedral angle ABCD is angle between four bonded atoms A, B, C and D as shown in Figure 5-5.

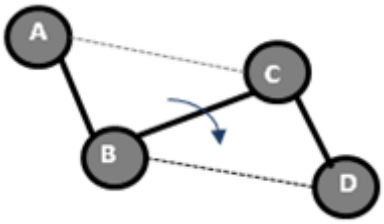

Figure 5-5: Dihedral angle

In proper dihedrals, we might expect full rotation about the connecting bond B-C. The torsional energy (U_{ABCD}) contribution in MM3 force field is given by:

$$U_{ABCD} = \frac{V_1}{2}(1 + \cos\omega) + \frac{V_2}{2}(1 - \cos 2\omega) + \frac{V_3}{2}(1 + \cos 3\omega) \quad \textbf{(5-17)}$$

Where V_1, V_2 and V_3 are force constants, ω is the dihedral angle.

5.2.4.4 Lennard-Jones potential

All the short-range non-columbic intermolecular pair potentials were modeled using Lennard-Jones (L-J) 12-6 potential. It takes the following form for interaction between atoms i and j .

$$\varphi_{ij}^{LJ} = 4\varepsilon_{ij}\left[\left(\frac{\sigma_{ij}}{r_{ij}}\right)^{12} - \left(\frac{\sigma_{ij}}{r_{ij}}\right)^{6}\right] \quad \textbf{(5-18)}$$

Where, σ is the collision diameter (the separation for which the energy is zero), and the well depth is ε.These parameters are graphically represented in Figure 5-6.The L-J 12-6 potential is zero at r=∞, and passes through minimum energy at $r_m = 2\sigma^{1/6}$ and depth $= -\varepsilon$ (Leach 1996). The attractive part of the potential varies as r^{-6} to represent the long-range dispersion energy, called London type of van der Waals forces. The short-range repulsive part varies as r^{-12} and dominates the r<σ region. The L-J parameters can be estimated from data on viscosity, the second virial-coefficient and from corresponding state principles (Kvamme 1984) .

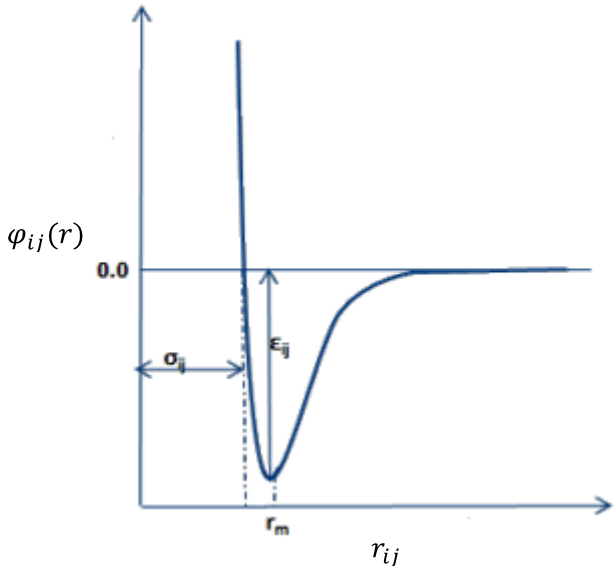

Figure 5-6: Lennard -Jones potential

In this work, all simulations involving more than one type of atoms, the Lorentz –Berthelot mixing rules have been used (Allen and Tildesley 1989). In this rule, σ_{ij} is represented by arithmetic mean of the values of two pure components i and j and ε_{ij} is given as geometric mean:

$$\sigma_{ij} = \frac{1}{2}(\sigma_i + \sigma_j) \quad \textbf{(5-19)}$$

$$\varepsilon_{ij} = \sqrt{\varepsilon_i \varepsilon_j}$$

Due to the PBC, to avoid molecules being influenced by itself, L-J potential can only be calculated up to the cut-off radius (r_{cut}) as illustrated in Figure 5-2. Hence a correction of the non-columbic interactions for $r>r_{cut}$ has to be estimated. Usually this energy correction term is treated as a constant, and is calculated once in the beginning of each simulation.

5.2.4.5 Coulombic interactions

The long-range electrostatic interaction potential energy (U_{ES}) between two molecules having non-uniform charge distribution calculated according to Coulomb's law:

$$U_{ES}(r_{ij}) = \frac{q_i q_j}{4\pi\varepsilon_0 r_{ij}} \quad \textbf{(5-20)}$$

Where, q_i and q_j are partial charges on the sites i and j respectively; r_{ij} is the site-site distance and ε_0 is dielectric permittivity of vacuum.

In a system with PBC, the slowly decaying Columbic energy is calculated by applying Ewald's method. Due to PBC, the infinitely replicated unit cells will form a lattice of electric charges. To evaluate the potential energy these electric charges must be summed up. In the periodically repeated system, the total energy of ion i in the field of all the other ions will be given by the following sum (Kuznetsova 2001):

$$U_{ES}(\vec{r_i}) = \frac{q_i}{4\pi\varepsilon_0} \sum_{\vec{n}=-\infty}^{\vec{n}=\infty} \sum_{j=1}^{N'} \frac{q_j}{|\overrightarrow{r_{ij}} - \vec{n}|} \quad \textbf{(5-21)}$$

Where, $\vec{r_i}$ identifies the position of charge q_i within the central cell (Figure 5-2),

Vector $\vec{n} = \{n_x L_x, n_y L_y, n_z L_z\}$ with $n_x, n_y, n_z = 0$(for central cell), $\pm1, \pm2, ...$,which is position of replicated cells. The prime in the second sum over all the charges in the system indicates the exclusion of self-interaction in the original box.

5.2.5 Radial distribution function

Radial distribution function (RDF), also called a pair correlation function, g (r), is the ratio of the actual density of particles at radius r to the average density ρ (Dill et al. 2003). When local density in a shell is the same as the average density over the whole volume, g(r) = 1.0. If the density of the particles in that shell is higher than ρ, g(r) will be greater than 1.0. Figure 5-7

shows a typical liquid RDF. Since particle cannot overlap, there is a depletion g(r) =0 for small r and then a peak indicates the presence of excess number of particles making first neighbor shell. A second neighbor shell follows this peak. Beyond third or fourth shell, there is little correlation and g(r) =1(Dill et al. 2003).

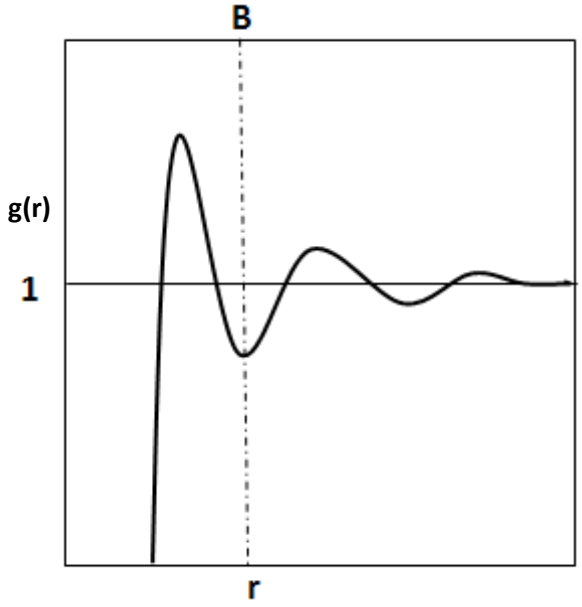

Figure 5-7: Typical liquids RDF. (B is the limit used to define the first shell of neighbors) (Modified from (Dill et al. 2003).

Pair correlation function g(r) can be determined experimentally using X-ray diffraction. From this function, we can find the average number of nearest neighbors of any atom/molecule. At radius, r the volume of a spherical shell is $4\pi r^2 dr$. Hence, the total number of molecules in the first shell of a molecule is the integral known as the coordination number, Nc.

$$N_c = \int_0^B \rho\, g(r) 4\pi r^2 dr \tag{5-22}$$

Where, B is the location shown in Figure 5-7.

5.2.6 Quaternion

For rigid non-spherical molecules, the rotation occurs around the center of mass. The three Euler angles,$\phi, \theta,$ and ψ are often used to describe the orientation of molecules (Hinchliffe 2003). First, we rotate by ϕ about the Cartesian z-axis. This changes the x and y-axes to x′

and y′ as shown in Figure 5-8. Then we rotate by θ about the new x-axis, which changes the y and z-axes. Finally, we rotate by ψ about the new z-axis.

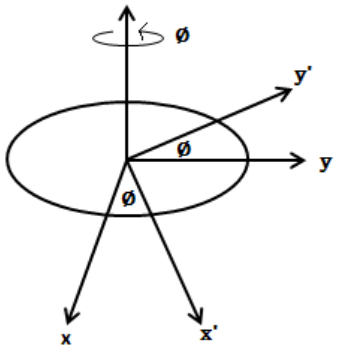

Figure 5-8: First Euler angle.

However, there are two technical problems with the use of Euler angles. First, a uniform distribution is not achieved by random sampling of angles. Second, a rotational matrix contains six trigonometric functions. These trigonometric functions are computationally expensive to calculate and are therefore a disadvantage. The most popular alternative is to use quaternion. A quaternion is a four-dimensional vector such that, its components sum equal to one: $q_o + q_1 + q_2 + q_3 = 1$. They can be related to the Euler angles as follows:

$$
\begin{aligned}
q_0 &= \cos\frac{1}{2}\theta\cos\frac{1}{2}(\phi+\psi) \\
q_1 &= \sin\frac{1}{2}\theta\cos\frac{1}{2}(\phi-\psi) \\
q_2 &= \sin\frac{1}{2}\theta\sin\frac{1}{2}(\phi-\psi) \\
q_3 &= \cos\frac{1}{2}\theta\sin\frac{1}{2}(\phi+\psi)
\end{aligned}
\qquad \textbf{(5-23)}
$$

5.2.7 Constraint dynamics

When considering the polyatomic systems, long chain molecules especially, bending and twisting moment responsible for changes in the angles between bonds and altering torsion angles needs to be considered. These torsional motions are very important and leads to conformational inter-conversion and have a direct influence on polymer dynamics (Allen and Tildesley 1989). It will be unrealistic to assume total rigidity of such molecule. Constraint

dynamics is a technique that handles these effects, in which certain selected degrees of freedom are constrained, while other remain free to evolve under the influence of intramolecular and intermolecular forces. The most commonly used method for applying constraints in molecular dynamics is the SHAKE algorithm. In this constraint dynamic approach (Ryckaert et al. 1977) each constraint is considered in turn and solved using equation of motion. It is necessary to iterate round the constraints until they are all satisfied to within some tolerance as satisfying one constrain may cause another constraint to be violated. The tolerance should be tight enough to ensure that the fluctuations due to the SHAKE algorithm in the simulations are much smaller than the fluctuations due to other sources like cutoffs (Leach 1996). In addition, the constrained degree of freedom should be only weakly coupled to the remaining degree of freedom in order not to affect the motion of the molecules by the application of the constraints. For small molecules, the constraint equations may be solved by straightforward algebra. SHAKE is most easily applied to the velocity Verlet algorithm, in which only positions and acceleration appear, it is then known as RATTLE algorithm (Andersen 1983). A problem with the SHAKE method is that it is not possible to control the rotation temperature explicit. This leads to an uncontrolled "production" of rotation entropy.

5.2.8 Nosé-Hoover thermostat

Simple velocity scaling is efficient in relaxing the system to the target temperature but it does not allow fluctuations in temperature that are present in canonical ensemble. Hence, once the system has reached equilibrium, Nosé-Hoover thermostat must be used to probe the correct canonical ensemble. A brief description of Nosé-Hoover thermostat is presented here. For more detail description on Nosé-Hoover thermostat we refer to (Hünenberger 2005). This thermostat was originally introduced by Nosé (Nosé 1984) and further developed by Hoover (Hoover 1985). The concept was based on considering the heat bath as an integral part of the system by addition of an artificial variable $\tilde{s}$, associated with a "mass" $Q > 0$ as well as a velocity $\dot{\tilde{s}}$. The temperature fluctuations are influenced by the magnitude of Q that determines the coupling between reservoir and the real system. The time scale in the extended system is stretched by the factor $\tilde{s}$.

$$d\tilde{t} = \tilde{s}dt \tag{5-24}$$

The atomic coordinates are equal in both the system leading to:

$$\tilde{r} = r\ , \dot{\tilde{r}} = \tilde{s}^{-1}\dot{r}, \tilde{s} = s\ and\ \dot{\tilde{s}} = \tilde{s}^{-1}\dot{s} \tag{5-25}$$

The Lagrangian for the extended system is chosen to be

$$\mathcal{L} = \sum_i \frac{m_i}{2}\tilde{s}^2\dot{\tilde{r}}_i^2 - U(\tilde{r}) + \frac{1}{2}Q\dot{\tilde{s}}^2 - gk_BT_o \ln \tilde{s} \tag{5-26}$$

The first and second term to the right side in the equation (5-26) represents kinetic energy minus potential energy of the real system. The additional terms are kinetic energy of $\tilde{s}$ and the potential, that is chosen to ensure that the algorithm produces a canonical ensemble where $g = N_{df}$ (total number of degree of freedom) in real time sampling (Nosé-Hoover formalism) and $g = N_{df} + 1$ for virtual –time sampling (Nosé formalism). The time evolution of the variable $\tilde{s}$ is characterized by a second order equation and hence heat may flow in and out of the system in an oscillatory fashion, leading to nearly periodic temperature fluctuations. The stretched time scale of the Nosé equations is not much instinctive and the sampling of a trajectory at uneven time intervals is rather impractical for the investigation of the dynamic properties of a system. The Nosé equation of motion however, can be reformulated and transformed in terms of real system variable by:

$$\begin{aligned} s = \tilde{s}, \dot{s} = \tilde{s}\dot{\tilde{s}}, \ddot{s} = \tilde{s}^2\ddot{\tilde{s}} + \tilde{s}\dot{\tilde{s}}^2 \\ r = \tilde{r}, \dot{r} = \tilde{s}\dot{\tilde{r}}, \ddot{r} = \tilde{s}^2\ddot{\tilde{r}} + \tilde{s}\dot{\tilde{r}}^2 \end{aligned} \tag{5-27}$$

Substituting,

$$\gamma = \frac{\dot{s}}{s} \tag{5-28}$$

The Lagrangian equation of motion can be written as:

$$\begin{aligned} \ddot{r_i} = \tfrac{F_i}{m_i} - \gamma r_i, \\ \dot{\gamma} = \frac{-k_B N_{df}}{Q} T(t)\left(\frac{g}{N_{df}}\frac{T_o}{T(t)} - 1\right) \end{aligned} \tag{5-29}$$

The friction mass Q and the extended system energy must be chosen carefully. If the value of Q is too large (loose coupling), the poor temperature control will be caused and the canonical distribution will only be obtained after very long simulation times. However if the value is too

small (tight coupling), high frequency temperature oscillations may result. As a better choice for the coupling strength, the Nosé equation of motion can be expressed as

$$\dot{\gamma} = \frac{-1}{\tau_{NH}}\left(\frac{g}{N_{df}}\frac{T_o}{T(t)} - 1\right) \tag{5-30}$$

With the effective relaxation time of

$$\tau_{NH}^2 = \frac{Q}{N_{df}k_B T_o} \tag{5-31}$$

The relaxation time can be calculated when estimating the frequency of the oscillations for small deviations $\delta\tilde{s}$ from the average $\langle\tilde{s}\rangle$.

6 Previous simulational work

Right choice of scientific method was needed to analyze the proposed hypotheses by different groups. Most of the theories were based on finding the phenomenon of nucleation, as this is the first step towards hydrate formation and then studying the further hydrate growth inhibition. Since nucleation step is a microscopic phenomenon it is difficult to observe experimentally and therefore, there was a need to perform molecular level simulations. Molecular Dynamics simulations were used to test the various hypotheses suggested in section 4.2.

To evaluate their two-step hypothesis, MIT considered fully dynamic water molecules in the hydrate crystal (Anderson et al. 2005). The water-soluble inhibitor monomers were placed in the liquid water phase. The TIP4P model was used for water, with PVCap monomers tested along with other KHIs. The work is focused on estimating the binding energy of inhibitor to the hydrate crystal surface. As shown in Figure 6-1, the energy of binding of PVCap was found to be -37.5 + 3.4 kcal/ mol, about 20 kcal/mol more than PVP concluding PVCap as a stronger binder to the hydrate crystal surface. This difference in binding strength mirrored PVCap and PVP relative efficiencies as hydrate inhibitors.

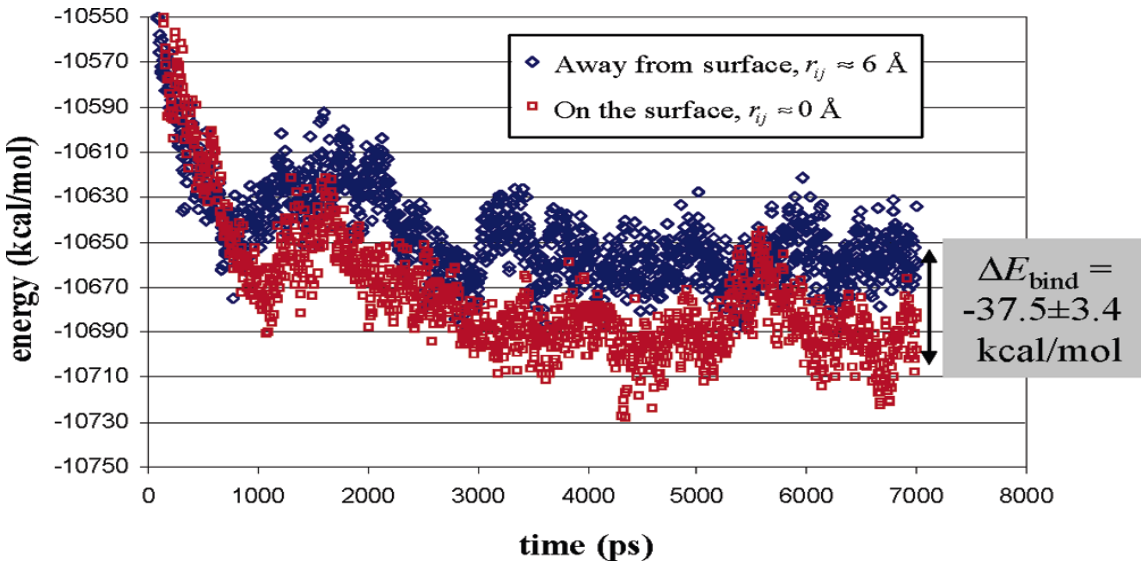

Figure 6-1: Dynamic energy of the PVCap -hydrate surface (Andersen et al. 2005)

One must note, these types of conclusions have to be taken with a grain of salt as their validity depends on types of inhibitors and corresponding interactions with hydrate but also subject to differences in characterization of the atoms.

Structural effects due to presence of an inhibitor molecule were probed by calculating the radial distribution functions (RDF), g(r), of the carbonyl oxygen on the inhibitor molecules with the oxygen of water in either the hydrate (bound inhibitor) or the liquid phase (unbound inhibitor). To get better understanding of how the monomer fits into the water structure and how it affects the water structure oxygen –oxygen RDFs for monomer – water interactions were compared with H2O–OH2 RDFs. As represented in Figure 6-2, the carbonyl oxygen falls into a lattice position typically occupied by a water molecule, thus leading to a strong binding energy and favorable free energy of "binding reaction". In liquid phase, this carbonyl oxygen of PVCap coordinated in the manner similar to water oxygen.

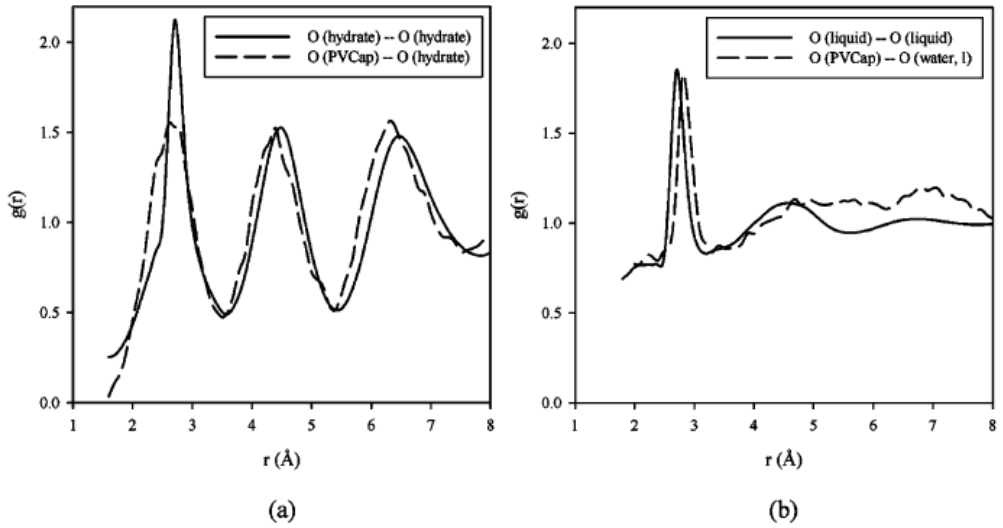

Figure 6-2: RDFs between carbonyl oxygen on PVCap and oxygen on water when the PVCap is (a) bound to hydrate surface (b) in the solution away from hydrate surface (Anderson et al. 2005).

These molecular simulations identified two molecular characteristics that lead to the strong binding of PVCap. (1)A charge distribution on the PVCap edge mimicking the charge separation in the water molecules on the surface of the hydrate, and (2) the congruence of the PVCap's size with respect to the available space at the tetrakaidecahedron binding site.

Moon et al. used classical molecular dynamics simulations to simulate the nucleation process for methane hydrate and study the effect of additives on the nucleation and growth (Moon et al. 2007). Data were presented for a number of different PVP oligomers that varied in

tacticity, initial conformation, and molecular weight. These data were compared with existing data for PDMAEMA, poly (dimethylaminoethylmethacrylate). The results showed that the PVP was effective in delaying nucleation by increasing the induction time and destabilizing hydrate clusters in the system where the growth has not occurred substantially beyond the critical cluster size (ca. 200 water molecules). However, once the hydrate grows to critical cluster size (ca. 400 water molecules), PVP was ineffective in modifying growth and inhibiting further growth. Simulation results indicated that PVP remained at least 5–10 Å away from the hydrate surface, and that the liquid water present near PVP is restructured by suppressing its hydrate phase consistency. The 5–10 Å separation between the PVP amide groups and the hydrate surface indicated that the PVP was present in the interfacial region, though without binding irreversibly to the hydrate crystal. Thus, continued growth will still be feasible once a critical nucleus has been formed.

It was evident from the simulations that filaments of hydrate water molecules do form from the pyrrolidone groups, but that they are transient. Several filaments can form from the same oligomer but they are mostly disproportionate with each other and so prohibit, rather than reinforce, hydrate formation. Such transient filaments were also initiated around the hydrate clusters and created a halo region around the hydrate that would be disrupted by the disproportionate filaments arising from the PVP. It was therefore concluded that this halo effect caused by the insertion of PVP, forms a viable mechanism to explain the kinetic inhibition of methane hydrate formation.

This mechanism is not expected to be universal as surface adsorption has been shown to be viable in PVCap (Anderson et al. 2005) and PDMAEMA in contrast to PVP which inhibits by increasing the surface energy of the interfacial region. However, it may well be accountable for the synergistic effect whereby co-polymers of PVCap and PVP are found to be more active inhibitors than PVCap alone (Larsen et al. 1999). It does also provide a new insight into the origins of LDHIs activity that should prove beneficial in designing inhibitors that are more active. This is in agreement with the results of (Anderson et al. 2005) whose calculations indicated that there was no free energy driving force ($\Delta G_{adsorption}$ = 0.4+3.9 kcal/mol) for the adsorption of VP monomers onto the surface of an aqueous methane hydrate crystal.

Kvamme et al. (2005) tested hydrate nucleation theory by implementing molecular dynamic to several kinetic inhibitors in liquid water and hydrate /liquid water system (Kvamme et al. 2005). The first system consisted of hydrate block placed besides liquid water with two monomers of PVCap place in liquid water phase. It was observed that after 250 picoseconds of simulation run, one of the PVCap monomers approached hydrate – liquid interface and stayed there for the rest of the run positioning it to form hydrogen bonds with the hydrate phase while other remained in the bulk liquid phase. When dimers of PVCap were used instead of monomers, the dimers stayed close to each other without significant displacement seen for the entire run of 900 picoseconds and kept the distance from the hydrate – water interface. Another system was studied with multiphase environment, where a layer of liquid water was replaced by liquid propane thus creating two competing interfaces namely water – hydrate and water – hydrocarbon. One of the PVCap monomer positioned at the water – hydrate interface at the start of the run and remained there. This PVCap molecule oriented to enable hydrogen bonding with the hydrate while other monomer moved to the water – propane interface, fully immersed in the propane phase with carbonyl oxygen forming hydrogen bonds with water. When comparing the results for PVP as shown in Table 6-A from the previous paper (Kvamme et al. 1997), a conclusion was drawn that PVCap will outperform PVP as a KHI since the potential energy of the inhibitor – hydrate interactions was significantly lower for PVCap then PVP with both Coulomb and Lennard – Jones contributions favoring PVCap over PVP.

Table 6-A: Properties of composite PVCap and PVCap-modified system (Kvamme et al. 2005)

System	PVP			PVCap			PVCap-modified		
Property	Total	Coul.	L–J	Total	Coul.	L–J	Total	Coul.	L–J
Total potential energy (kJ/mole)	−42.71			−43.06			−43.12		
Hydrate water–inhibitor (kJ/mole)	−41.08	−26.01	−15.07	−46.15	−37.51	−8.63	−62.38	−42.48	−19.90
Liquid water–inhibitor (kJ/mole)	−17.02	−9.54	−7.47	−25.77	−8.64	−17.13	−24.56	−19.23	−5.33

'Coul.' stands for electrostatic contributions; 'L–J', short-range Lennard–Jones contributions to the total energy.

A modified version of PVCap monomer, with a hydroxyl group added to the ring, increased its potential for attachment to hydrate surface even further. The paper also suggested that a monomer of inhibitor molecule would be rather ineffective as a KHI. The molecular weight and longer chain length distribution will have a specific macroscopic effect in packing of

these polymers at the interface and adsorbing to the forming hydrate surface, which will increase the induction time for massive hydrate growth.

Sapronova and Johannsen (2008) at the UIB also studied the mechanisms of gas hydrate formation and dissociation in the presence of PVCap using NPT molecular dynamics simulation (Sapronova and Johannsen 2008). Their specific objectives were:

a) Investigate the kinetics of dissociation of gas hydrate (GH) by undertaking sufficient number of independent MD runs.
b) Examine the fluctuations in GH cavity size while dissociating with respect to time in the presence of PVP & PVCap monomers.
c) Study the effect of methane composition and crystallite size on dissociation of GH.
d) Examine the effect of different potential for the evaluation of interactions on the dissociation of GH.

Partially built $5^{12}6^2$ hydrate cavity was chosen as hydrate model and then this model with inhibitor monomer was submitted for HF/6-311+G* geometry optimization. Two cells consisting of water – methane mixture along with hydrate cavity and KHI monomers were considered whereas one other cell without KHI was considered. The simulations were performed for systems at three constant temperatures of 280, 290, and 300 K and three pressures 30, 50, and 100 bars. The results are as shown in Table 6-B. During simulations, it was found that the hydrate crystallites with built-in inhibitors were not stable and tended to dissociate within about 9 nanoseconds at 290-300K temperature range and 30-50 bar pressure, while inhibitor-free baseline system dissociates at higher pressure (50-100 bar) and lower temperatures. The performed MD simulations was also compared and confirmed experimental evidence that conditions for the hydrate dissolution are displaced towards higher temperatures or lower pressures.

Table 6-B: Calculated percentage value of GH crystal dissociated after t =9ns. (Modified from (Sapronova and Johannsen 2008)

PVP	280 K	290K	300K
30 bar	14.5	29.0	38.2
50 bar	9.7	12.2	30.6
100 bar	6.2	6.1	31.9

PVCap	280 K	290K	300K
30 bar	21.3	26.2	39.8
50 bar	9.5	16.2	37.2
100 bar	4.5	9.8	28.9

No inhibitors	280 K	290K	300K
30 bar	24.3	34.6	49.2
50 bar	19.9	27.3	38.0
100 bar	13.5	15.5	36.9

7 Strategy

The main purpose of any study is its applicability to the problem at hand. The study of kinetic inhibition in case of PVCap was proposed to develop this knowledge further to find the solution to problems caused by hydrate formation. Once the correct mechanism has been pinpointed, KHIs that are more effective can be designed and used. Strong binding of PVCap depends on correctly estimated partial charges (Anderson et al. 2005). Accurate molecule modeling, the chain length and chain length distribution of PVCap may have a significant influence because they will affect interface coverage and coupling to the forming hydrate. The effect of PVCap needs to be analyzed in both, before hydrate nucleation in the presence of aqueous water and hydrocarbon phase and after hydrate formation (presence of hydrate crystal, liquid water and hydrocarbon phase). How the PVCap will behave when the driving force for hydrate formation is high for instance, at high concentration of methane also needs to be studied. All these questions have to be addressed to get a more comprehensive understanding of the inhibition effect caused by PVCap.

If the correct mechanism is understood, working of KHIs will no more be a mystery, and KHIs could be used effectively for inhibiting hydrate formation process. In order to get the insight into the mechanism of KHIs at molecular level, the following steps were decided on:

Creating a PVCap Model: It was decided to model a 12-unit PVCap oligomer with molecular weight of 1657.2 gram/mole. To obtain correct partial atomic charges, the Jaguar/ Maestro (Schrodinger 2008) software was chosen to perform geometric optimization first in vacuum and then in solvated water using SM6 (Kelly et al. 2005). The MM3 force field parameters were used for angles and torsions. To investigate the effect of partial charges on behavior of molecule, charges obtained from both, Löwdin population analysis and Charge Model 4 were used in separate runs.

Study the effect of PVCap before hydrate formation at different driving forces: System containing liquid water and methane at different densities in presence of PVCap dodecamers needed to be studied. Reference system without PVCap was also explored to isolate the effect of presence of PVCap.

Effect of PVCap concentration: To probe the effect of PVCap's concentration on the inhibition efficiency, systems containing two and nine PVCap oligomers were used.

Growth inhibition effect of PVCap after hydrate formation: This step demanded a system with stable hydrate phase so that the correct effect of PVCap could be tested. In order to do so a goal was set to create a system consisting of stable hydrate phase in presence of liquid water and hydrocarbon and then insert PVCap molecules.

The next chapter outlines the force field used to model the molecules, as well as simulational systems and their setups.

8 Simulational details

This chapter is divided into two sections. Section 8.1 describes the choice and development of the molecular models and force fields. It is followed by section 8.2 in which the setup of simulation system containing these models is discussed.

8.1 Molecular models

Three different molecules are used in the simulations, water, methane and PVCap. The models used are as presented below.

8.1.1 SPC/E water model

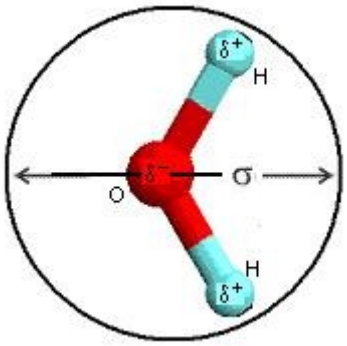

Figure 8-1: Three sited SPC/E water model.

Simple Point Charge/ Extended (SPC/E) Model was used for water. This is a three-point charge model (on hydrogens and oxygen) with a L-J 12-6 potential located on the oxygen site only. The parameters were taken from (Berendsen 1987) and are listed in Table 8-A.

Table 8-A: SPC/E Water Parameters

Site	Atom	Charge, q [Q]	σ [Å]	ε [kJ/mo]
1	O	-0.8476	3.166	0.6507
2	H1	0.4238	0	0
3	H2	0.4238	0	0

The oxygen-hydrogen bond length is kept constant at 1Å, while the angle between the two hydrogen atoms has the equilibrium value of 109.47 degrees. Force constant of 191.5 kJ/mol $(\text{degree})^2$ was applied to the angle.

8.1.2 OPLS one-site methane model

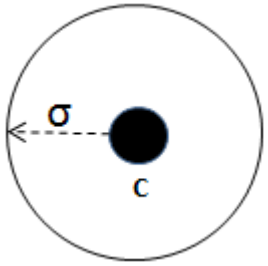

Figure 8-2: One-site OPLS methane.

One-site OPLS (Optimized potential for liquid simulations) model for methane (CH_4) was used. This model represented molecule with a L-J 12-6 potential considered at the centre of the carbon atom. The parameters are taken from (Jorgensen 1984) and are listed in Table 8-B.

Table 8-B: OPLS one-site methane parameters.

Site	Atom	Charge [Q]	σ [Å]	ε [kJ/mo]
1	CH_4	0	3.73	1.2309

8.1.3 PVCap dodecamer model

PVCap consists of a seven-member lactam ring with oxygen attached to the carbon atom adjacent to nitrogen. The formula for monomer unit of PVCap is CH(2)CHNCOC(5)H(10). A 12-unit oligomer forming PVCap (dodecamer) was built using quantum mechanics package Maestro / Jaguar (Schrodinger 2008) with DFT/B3LYP. Figure 8-3 shows how each unit of the PVCap molecule consists of carbon ring attached to backbone. In this figure, carbon atoms are indicated in cyan, nitrogen in blue, oxygen in red and hydrogen atoms in grey color. The nitrogen atom present in the ring is attached to the backbone carbon atom. Maestro package was used to construct the PVCap dodecamer model consisting of 275 atoms and make the input file for Jaguar. This input file was then used by Jaguar to perform geometry optimization with sequentially increasing basis sets. At first the geometry optimization was done in vacuum starting with minimal basis set of STO-3G, followed by STO-3-21G and at the end STO-6-31+G**(See section 5.1.2 for details). After the convergence of geometry optimization, Single point energy calculation was performed in Jaguar to obtain the initial charges from vacuum estimates using the STO-6-31+G** basis set. SM6 (Kelly et al. 2005) was used afterwards to perform calculation for PVCap solvated in water. As discussed in section 5.1.4, SM6 first calculates partial charges using LPA and then redistributes the

charges utilizing RLPA, and finally applies CM4 to get partial atomic charges in accordance with experimental dipole moment. LPA, RLPA and CM4 methods for obtaining partial atomic charges are discussed in section 5.1.5.

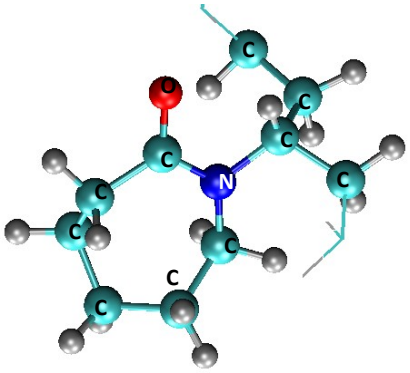

Figure 8-3: The PVCap ring and backbone.

Since, SM6 can calculate partial atomic charges only from these three methods it was decided to make the PVCap model with the two sets of charges obtained from LPA (least accurate) and CM4 (most accurate). Figure 8-4 and Figure 8-5 were snapshot taken using VMD to represent the final PVCap model with charges obtained from LPA and CM4 respectively (Humphrey et al. 1996). The most positively charged atoms are represented by red color whereas the most negatively charged atoms are represented with navy blue color. White color is for neutral charges. Charges obtained from LPA indicate that all the hydrogen atoms are positively charged thereby forming the external positively charged surface of PVCap. In contrast to this, CM4 charges on hydrogen atoms are almost neutral. The double-bonded (carbonyl) oxygens are the most negatively charged atoms in both cases, with their charges being more negative in case of LPA. Carbonyl carbon and nitrogen are more positively charged in CM4 than in LPA. The other two carbon atoms attached to negatively charged nitrogen are slightly negatively charged in LPA, whereas they are slightly positively charged in CM4. The other carbon atoms in the ring are negatively charged in LPA and are close to neutral for CM4. The study and comparison of these charges indicate that charges obtained from LPA and CM4 are quite different and can affect the behavior of the molecule. Since diffuse basis set was used in calculation of partial atomic charges, the previous studies report that LPA will produce significant errors (Thompson et al. 2002) and may distribute more negative charge on some of the atoms. As discussed above, the backbone carbon atom attached to nitrogen and the carbonyl oxygen was more negatively charged in LPA than in CM4. This indeed proves that LPA method assigns more negative charges to these atoms than

CM4. Since PVCap interaction with water and methane should in theory be significantly affected by the charge distribution, it was decided to study the effect of different charge sets and its inhibitor efficiency on the behavior of the molecule. To achieve this separate simulation runs were carried out utilizing LPA and CM4 separately in each case. The charges obtained from both the methods are listed in Appendix A. The complete *.mol files used in the simulations are presented in CD attached along with this thesis.

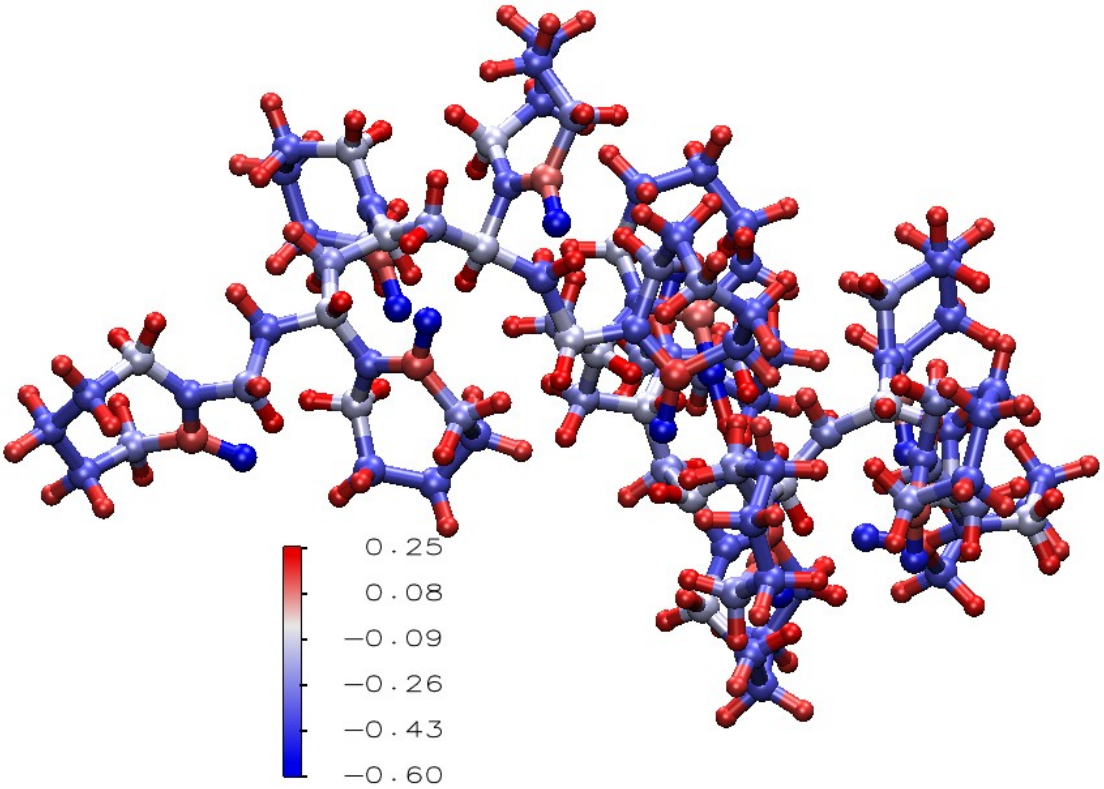

Figure 8-4: Partial atomic charges obtained from LPA (red for atoms with maximum + charge and navy blue for atoms with maximum – charge).

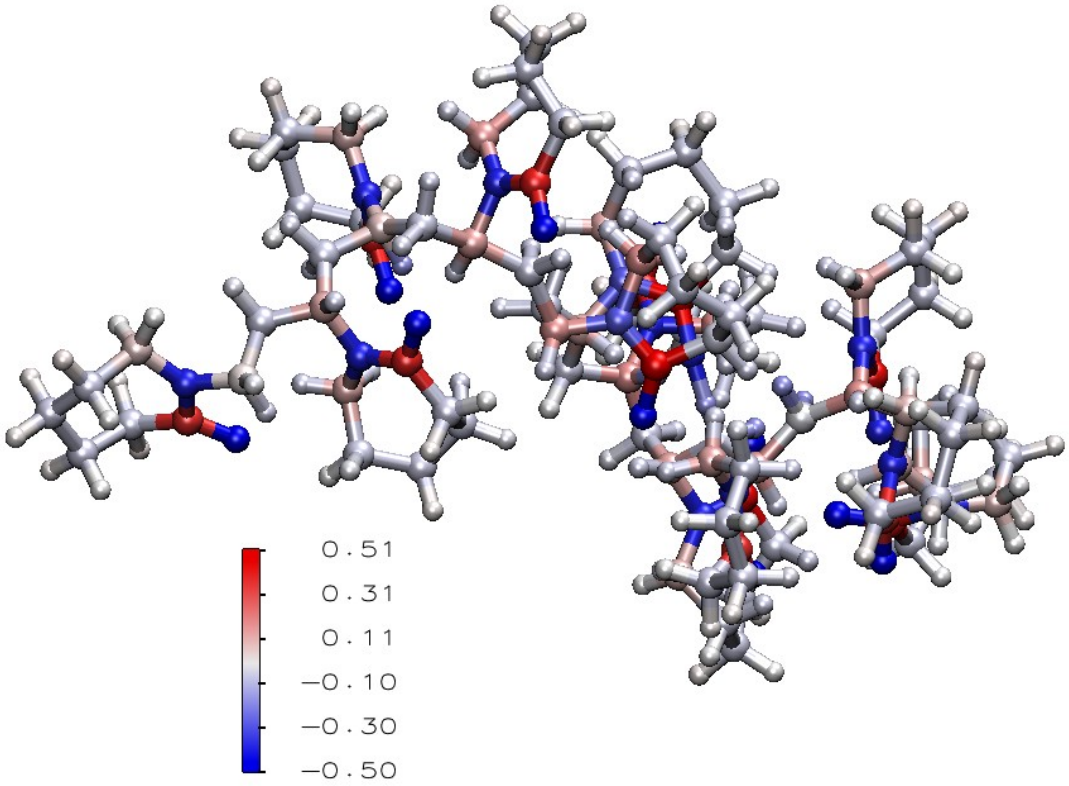

Figure 8-5: Partial atomic charges obtained from CM4 (red for atoms with maximum + charge and navy blue for atoms with maximum – charge).

The OPLS-AA Lennard-Jones potential parameters were used for PVCap and are listed in Table 8-C (Kaminski and Jorgensen 1998). All the bond lengths were kept constant using constraint dynamics. Since the torsional and angle bending motions are very important and must be depicted correctly, the MM3 force field parameters were used (Allinger et al. 1989; Allinger and Durkin 2000) for the backbone C-C-C angles and all dihedrals. The force constant value of 201.77 kJ/mol (rad) ^{2} was utilized for all the 21 number of C – C – C backbone angles.

Table 8-C: OPLS-AA, Lennard-Jones 12-6 parameters.

Atom Type		Description	σ [Å]	ε [kJ/mo]
1	C	sp^3 Carbon (ring)	3.5	0.27614
2	C	sp^3 Carbon (backbone)	3.5	0.27614
3	C	Carbonyl Carbon (C=O)	3.75	0.43932
4	N	sp^2 Nitrogen (Amide)	3.25	0.71128
5	O	Carbonyl Oxygen (O=C)	2.95	0.87864
6	H	Hydrogen on sp^3	2.5	0.12552

L J parameters taken from (Kaminski and Jorgensen 1998)

Table 8-D lists the force field parameters (V1, V2, and V3) used for the different types of dihedrals. In all, there were 286 bonds, 570 angles and 230 dihedrals excluding the dihedrals formed by hydrogen atoms.

Table 8-D: Dihedral parameters.

Dihedral Type		V1 (kJ/mol)	V2(kJ/mol)	V3(kJ/mol)
1-1-1-1	C-C-C-C	0.774	0.711	4.853
2-2-2-2	C-C-C-C	0.774	0.711	2.176
3-1-1-1	C-C-C-C	0	1.674	6.778
1-1-3-5	C-C-C-O	-1.912	4.628	-0.669
1-4-3-5	C-N-C-O	-2.51	46.246	0
2-2-2-4	C-C-C-N	-1.264	2.912	2.088
4-1-1-1	N-C-C-C	-1.264	2.912	5.69
2-2-4-1	C-C-N-C	4.008	-0.649	3.205
2-4-1-1	C-N-C-C	4.008	-0.649	5.69

Dihedral parameters taken from (Allinger et al. 1989; Allinger and Durkin 2000)

In order to find the density of PVCap, the parachor values method was utilized. The parachor P_r, for any substance is a constant and is relatively independent of temperature. The contributions to the parachor of a compound made by various atoms, bonds and structures are given in Table 8-E .

Table 8-E: Parachor values taken from [a](Quayle 2002), [b](Sewell 1973).

Group / Atom	Parachor contribution	Bond or structure	Parachor contribution
CH2[a]	40.0	7-membered ring[a]	4.0
C[a]	9.0	Double Bond[b]	23.2
N[a]	17.5		
O[a]	19.8		
H[a]	15.5		

C=Carbon, H=Hydrogen, N=Nitrogen, O=oxygen

The molar volume, V_{m} in cubic centimeter was calculated using equation (8-1) (Sewell 1973). The molar volume of a model molecule can be substantially different from that of a real molecule and different PVCap models will have different molar volumes. Model molar volumes for model molecules can be estimate from a NPT simulation of the pure substance.

$$V_{\mathrm{m}} = \frac{P_r + 7.7}{2.596} \qquad \textbf{(8-1)}$$

Final value obtained for PVCap was P_r= 4047 (additive of all atoms, bonds and structures), Solving equation (8-1) we get, V_{m}=1561.9 cm^3/mole. Once the molar volume is known, density can be calculated dividing molecular weight by molar volume.

$$\text{Density} = \frac{\text{M.W}}{V_{\mathrm{m}}} = \frac{1657.2}{1561.9} = 1.061\ \text{gram/cm}^3$$

The density of Vinyl Caprolactam as given by BASF at 40°C is 1.01 gram/cm^3, which is quite close to the value, calculated using the parachor method. One drawback of using parachor is that the calculated density is considered independent of temperature, which may not be the case.

To check how the angle bending movement is affected by the absence of force field applied, no force was initially applied on angles, and they were allowed to vary freely. After the simulations had run for a while, deviation of angles from average values was checked and it was observed that they did not fluctuate much around the average. Values calculated by the quantum mechanics for angles at different positions varied from 155.73° to 85.52 °. Since the variation was quite large, the 21 number of C-C-C backbone angles were assigned averaged alternating values of 114.63° and 116.34°.

8.2 Setup of simulation systems

NVT ensemble was used as the basis for the simulations, with the primitive different cells containing different combinations of molecules presented in section 8.1. Systems containing PVCap were initially set up, using charges obtained from the LPA, and then the systems were replicated replacing LPA charges with CM4. Due to time constrains, the systems with CM4 charges were run for shorter intervals ranging from 23 nanoseconds to 27 nanoseconds which is still quite long. Initially all the molecules were treated as rigid by setting quaternion treatment to true. The SHAKE algorithm was applied later to implement the bond constraints. Periodic boundary conditions (PBC) were applied in all three directions. Simple velocity scaling was used initially; with 5K as the permissible deviation since, simple velocity scaling is faster, more robust and does not fail for systems far from equilibrium. The temperature was set to 200 K. Short-range molecular interactions were modeled using the Lennard–Jones potential and were truncated at 12 Å, and the partial charges interactions were calculated by

Coulombic term. Electrostatic interactions were handled by means of Ewald summation. The time step was set to 1.0×10^{-15} seconds. Intermediate averaging were performed for every 1000 steps. A sample of MD input file can be found in Appendix B as well as in the CD attached along with this thesis.

At the start of the simulation, velocities were assigned to the molecules according to the Maxwell distribution. The interfacial tension (σ) is calculated in the code by using pressure tensor under the assumption that there are two interfaces normal to the z-axis, in the system (due to PBC), In order to achieve the bulk behavior in the center of methane and liquid phases, the phases had to be extended in z-direction. The following equation was used to calculate σ:

$$\sigma = 0.5 \times \overline{h_z}\left\{P_z - \frac{1}{2}\left[P_x - P_y\right]\right\} \quad \textbf{(8-2)}$$

Where P_i is the average system pressure in the i^{th} direction and $\overline{h_z}$ is the box length in the direction normal to the interface.

To implement parallel computation, the Message Passing Interface (MPI) was used. The initial simulation runs were carried out on the local Linux cluster with 24 8-processor machines. Due to this, one nanoseconds of simulation took around three weeks for most of the systems. The other Linux cluster available could not be used since the md43 code had problems with compilers. The code was later successfully compiled on the Hexagon clusters (the supercomputer provided by Bergen Center for Computational Science). This made it possible to continue the simulations on the Hexagon cluster during the last three months, which made the simulation runs faster and more efficiently because of the availability of more CPUs. However, the limitation of md43 coding did not support the use of more than 64 CPUs for System IV and 80 CPUs for other systems.

Reference System I and II will be discussed together since they differ only in methane concentration. This was done to draw comparisons between the two systems and highlight the impact of a higher driving force for hydrate nucleation. To serve the same purpose, PVCap System I & II are also described together.

8.2.1 Reference systems I and II

Reference system I (RSI) consisted of 1306 SPC/E water molecules and 260 OPLS methane molecules. To create an interfacial 2-phase system from the start, 1306 SPC/E water molecules were first placed in a Face Centered Cubic (FCC) lattice with dimensions of 36.09 Å x 36.09 Å x 30.0 Å to achieve the experimental water density of 0.999 g/cm^3. The water molecules were randomly oriented and the system was equilibrated for 50000 time steps. Secondly, a box with dimensions of 36.09 Å x 36.09 Å x 20.0 Å and 260 OPLS methane molecules was created, with the density of 0.265 g/cm^3 corresponding to that of bulk methane at 200 K and 100 bars. This box was then equilibrated for 50000 time steps. After this, the two boxes were stacked in the z-direction with the composite system as shown in Figure 8-6.

The final box size was 36.09 Å x 36.09 Å x 50.05 Å with the overall density of 0.6992 g/ cm^3. To avoid the unnatural forces that may arise due to two boxes placed closed to each other, the system was equilibrated for 29 nanoseconds with quaternion set to true. The quaternion treatment was then set to false and the free rotational motion was allowed for all the molecules.

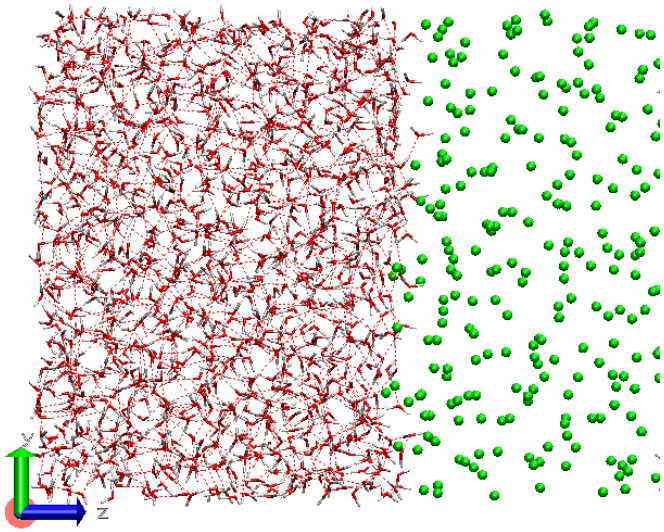

Figure 8-6: Reference system I (water molecules are red & white lines, and methane are green balls)

Reference system II (RSII) was created similarly to the RSI. The procedure followed to set up this system was same except that the number of methane molecules was doubled to 520 and the overall density of the system was 0.8045 g/ cm^3. At the start, the rotational motion of molecules around the center of mass was handled using quaternion treatment. The system was equilibrated for 22 nanoseconds before setting quaternion to false.

8.2.2 PVCap systems I and II

These systems were similar to reference systems described above except for that it contained 2 PVCap molecules in addition. To create PVCap system I, 2 PVCap molecules and 1306 water molecules were initially placed on a FCC lattice on a box measuring 120Å x 120Å x 120 Å. The orientation of all molecules was assigned at random. The size of the box was then gradually decreased to 40 Å x 40 Å x 40 Å and equilibrated for 10000 time steps. The time step used for equilibration was 1.0×10^{-16} sec. This box was then combined along the z direction with the box containing 260 OPLS methane molecules similar to that used in RSI (Figure 8-7).

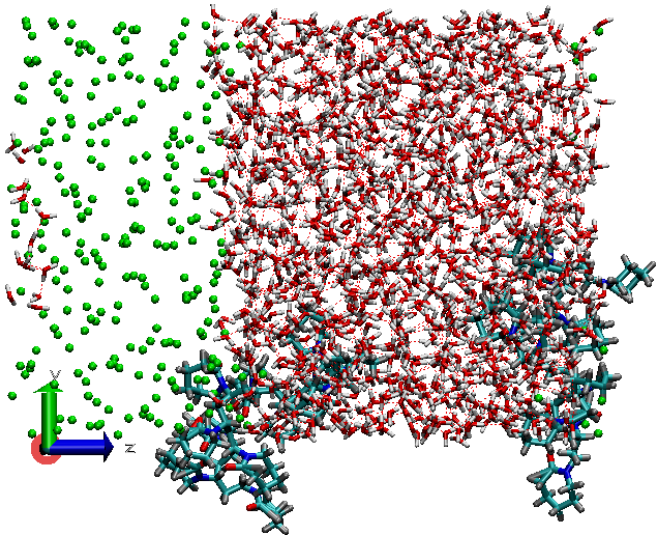

Figure 8-7: PVCap system I (water molecules are red & white lines, methane are green balls, PVCaps are blue, white and red)

To avoid the overlap forces and possible system blowup, quaternion treatment was set to true and the fused box size was increased to 50Å x 50Å x 100Å. The size of the box was gradually decreased to 36.09 Å x 36.09 Å x 50.05 Å and the system was equilibrated for another 2 million time steps. At this point, the quaternion was set to false and the rotational motions of the molecules were allowed. The time step was changed to 1.0×10^{-15} seconds. The final density of the system was 0.7830 g/ cm^3.

PVCap system II was identical to that of PVCap system I apart from that the concentration of methane was doubled in system II (520 methane molecules). The box size was the same as well and the total density was 0.8883 g/ cm^3.

Both PVCap system II and I were run using two different PVCap models, one utilizing partial charges obtained from LPA and other using those obtained from CM4.

8.2.3 PVCap system III

To build this system from two building blocks, the procedure similar to that used in PVCap system I was tried. For this, first a system consisting of 9 PVCap and 1306 water molecules, randomly distributed on the FCC lattice with dimensions 120Å x 120Å x120Å was build. This system was then gradually compressed to 36.5 Å x 36.5Å x 36.5Å in size and equilibrated for 0.2 million time steps with time step of 1 x 10^{-15} seconds. This box was then stacked together with a slab containing 520 OPLS methane molecules following the similar procedure as in RSI. In order to overcome the overlaps, the overall size of the final system was increased again to 100 Å x 100 Å x 125 Å. Constraint dynamics repeatedly failed in this system, and therefore a run with fully flexible molecules was initiated. Figure 8-8 shows the final system setup.

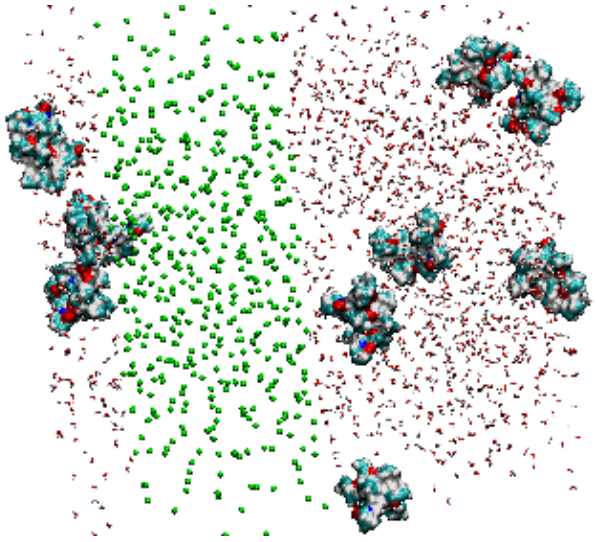

Figure 8-8: High PVCap content system

However, blowing up the system to overcome the overlaps did not work in this case. Some overlaps were reduced but certain water molecules remained too close to PVCap and caused the system to generate large forces and to destabilize. Reduction in time step further to 1 x 10^{-18} seconds did not help either. Due to this problem, the system was not run further and it was decided to put all the molecules in one box from the start. A new system was then set up as follows.

All the molecules, i.e. 9 PVCap dodecamer + 1306 Water molecules + 260 Methane molecules, were placed on the FCC lattice with initial dimensions 100Å x 100Å x 100 Å. The orientation of all molecules was initially assigned at random. The size of the box was gradually decreased to 60.0 Å x 60.0 Å x 60.0 Å, and the system was equilibrated for 37000 time steps using the time step of 1.0×10^{-16} sec (Figure 8-9). At this point the time step was increased to 1.0×10^{-15} sec and the molecules were made fully flexible by setting both quaternion and constraint dynamics to false to allow the molecules to reorient themselves into most favorable position. Constraint dynamics was then set to true. The box size was further gradually reduced to 37.09 Å x 37.09 Å x 50.5 Å, and the system was equilibrated for 1-million time step. The density of the system was 1.0188 g/ cm^3. Two separate runs were set for System III, one using partial charges obtained from LPA and the other utilizing the CM4-derived charges.

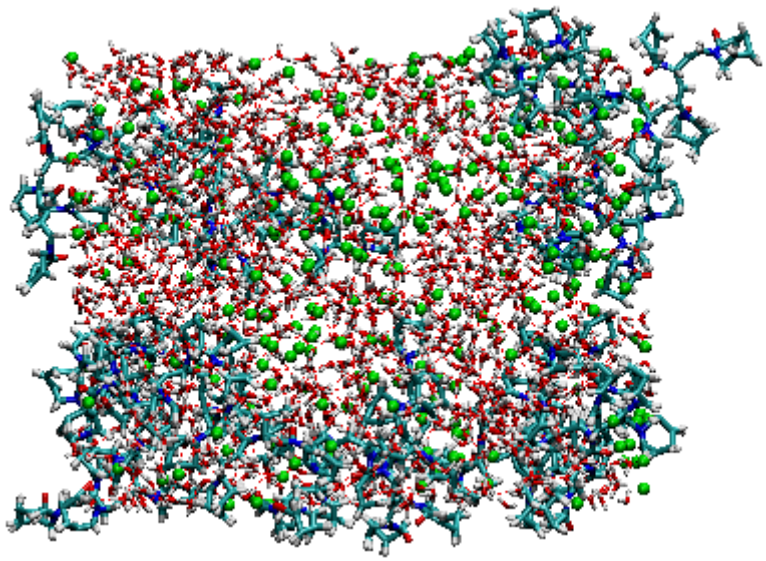

Figure 8-9: System III (water molecules are red & white lines, methane are green balls, PVCaps are blue, white and red)

8.2.4 System IV

An in-house program created 3 × 3 × 9 units of structure I hydrate from the known crystallographic coordinates of water and methane. 3726 water molecules and 648 methane molecules were used. Water molecules had only rotational motion during initial equilibrium, while translational movement was allowed for methane molecules. The system was then equilibrated for 0.05 million-time steps to obtain representative structure I hydrate with both

the small and large cavities occupied by methane. The [110] crystallographic plane of the hydrate was exhibited at the box boundaries. The primary cell measured 36.09 Å × 36.09 Å × 108.27 Å.

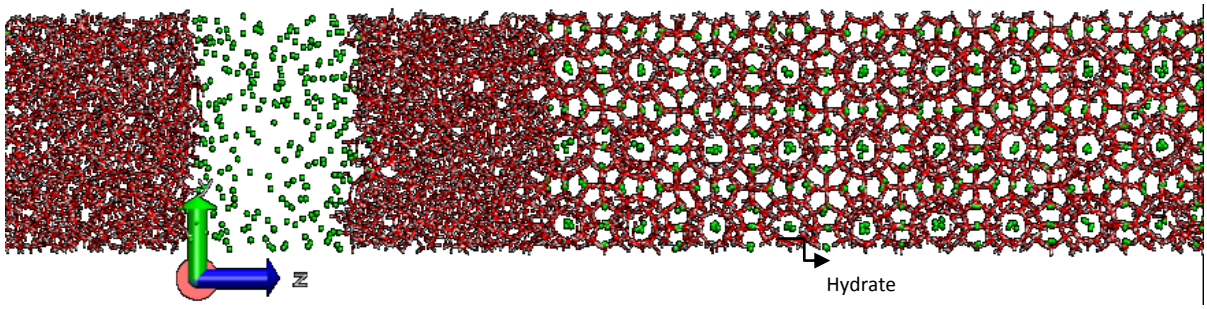

Figure 8-10: System IV (water molecules are red & white lines, and methane are green balls)

Secondly, a system similar to RSI but with an additional slice of the water replicated, was fused along the z-axis. The system was equilibrated and then combined with the structure I hydrate slab from the first step. The resulting composite system is shown in Figure 8-10. This system was meant to test the stability of hydrate in contact with liquid water and find the right temperature before PVCap could be placed in the system. To achieve this, system was simulated at two different temperatures, 200 K and 240 K.

9 System evolution, results and discussion

This section analyzes the model systems studied in this thesis. Detailed description of sampling that map the time evolution of the model system is presented. Close to the end of the simulations run, Nosé –Hoover thermostat was switched on for temperature control instead of simple velocity scaling to achieve the better approximation of canonical ensemble. The translational and rotational parameters in Nosé –Hoover thermostat were set to 100 femtosecond with internal parameter set to 50 femtosecond. This enabled more accurate sampling of the final thermodynamic properties.

To calculate the density profiles with x-y averaged quantities of interest, an in house MATLAB code was used, with the DCD files generated by md43 code serving as input. The simulation box was partitioned into discrete bins in the z direction. RDFs for various atomic pairs and the number of hydrogen bonds formed between PVCap and water molecules were calculated using the corresponding VMD plug-in. Wherever not specified, snapshots taken by VMD use following coloring convention: methane in green, water in red whereas PVCap molecules as blue, white and red continuous surfaces.

9.1 Reference system I & II

Reference System I (RSI) was simulated for 111 nanoseconds. The time step of 1 x 10^{-15} seconds was used during the entire simulation run. The time evolution of the system is shown in Figure 9-1. To illustrate the water and methane molecules packing at close distances, different types of representation are used. Large green balls are used for methane close to water, and red and white sticks for water molecule close to methane. The diffusion of methane inside water began about 29 nanoseconds into the simulations. The number of dissolved methane molecules increased as the simulation progressed. After 102.6 nanoseconds into the simulation run, Nosé –Hoover thermostat was switched on. By the end of 111 nanoseconds, there were 8 molecules of methane completely dissolved inside the water phase. Visual inspection showed the reorganization of water molecules around methane, due to the latter's hydrophobic nature. As soon as methane diffused inside water, partial cavities and hydrogen bonding network of water started to form and break around methane. Methane molecules dissolved in water were in general quite far from each other with no formation of

stable cavities or sharing of rings between two methane molecules observed. These methane molecules formed hydration shells at different locations instead.

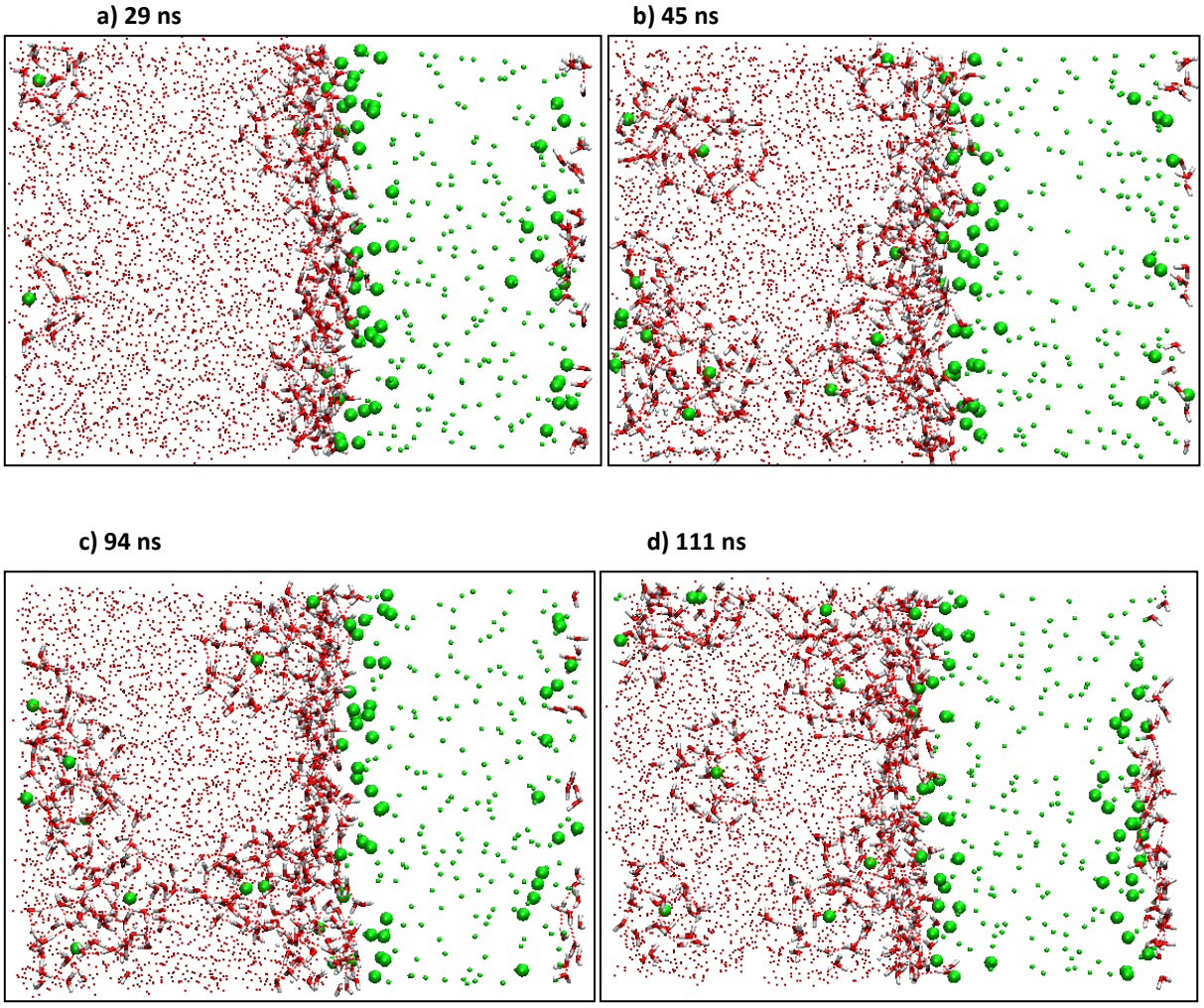

Figure 9-1: Simulation progress over time. a) After 29 ns b) after 45 ns c) after 94 ns d) 111ns.

The density profiles for methane and water distribution over the entire box were calculated. The profiles were generated by partitioning the simulation box into 100 bins in the z direction. The system ranged 50.5 Å in z direction. Due to PBC applied, the system drifted very fast across the box and hence the density profile used five frames corresponding to 5000 time steps. The initial state of the system was first studied to determine the initial distribution of molecules. Figure 9-2 presents the initial density profile just after the start of the production simulation run. The red dotted line indicates the average density of the liquid water as a function of z and green bold line indicating the average density of methane. The average density of bulk water phase was 0.999 g/cm^3 and bulk methane phase, 0.265 g/cm^3 also seen in the Figure 9-2 with the peaks seen in the bulk water phase fluctuating 1.21 g/cm^3 to 0.78

g/cm^3. A sharp interface between water and methane phase can be seen in figure. This sharp interface is unrealistic, and depicts conditions in the system after equilibration. The molecules overlap at the interface but at the start of simulation, there was no transition of molecules from one phase to another. The final density profile is shown in Figure 9-3.

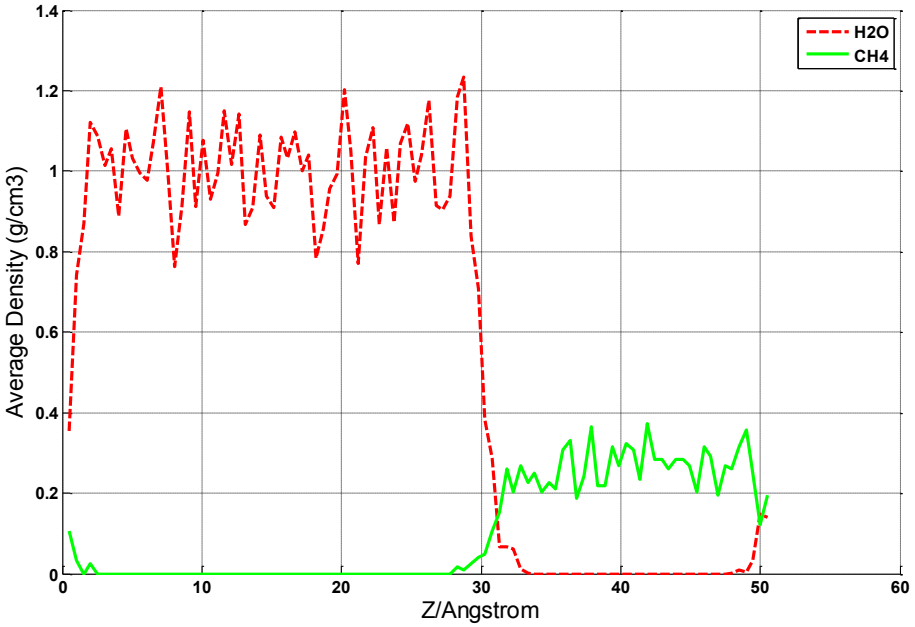

Figure 9-2: Density profile at the start of the simulation

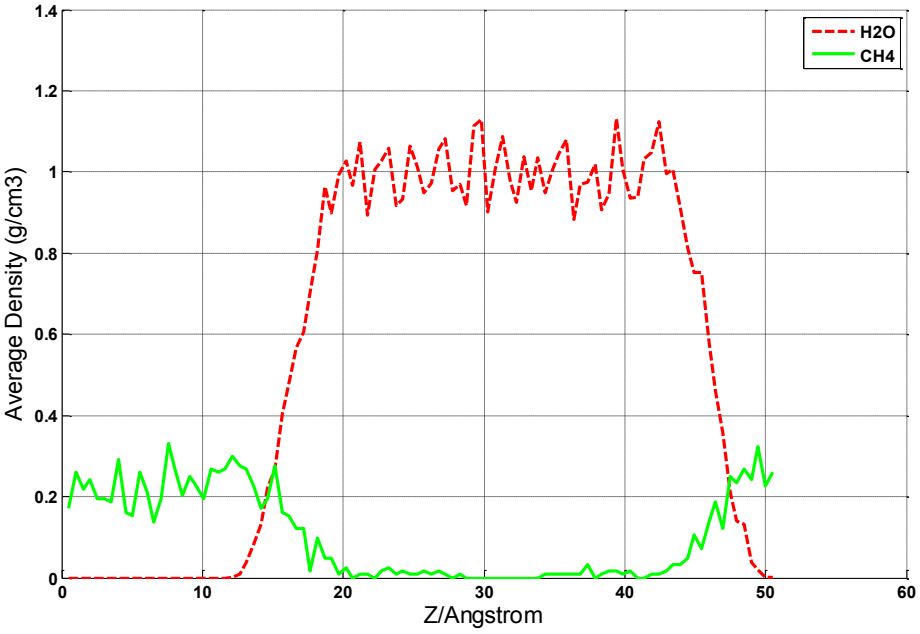

Figure 9-3: Density profile at the end of simulation.

This profile represents the final simulation run as shown in the snapshot taken after 111 nanoseconds. A more diffuse interface has been achieved with the methane density gradually

decreasing from interface to the bulk water phase. The small peaks of methane seen in the bulk water phase are due to the diffusion of methane inside the water phase. Water looks more structured with more uniform peaks, fluctuating from maximum value of 1.15 g/cm^3 to minimum of 0.9 g/cm^3. Since methane is hydrophobic, diffusion of methane inside bulk water will lead to restructuring of water around methane.

To probe the nature of hydration shells formed around methane, pair correlation function between diffused methane and hydrogen atoms of water (HW) close to methane were calculated. These were then compared with the CH4 – HW RDFs typical for hydrate. As demonstrated in Figure 9-4, the first peaks in both cases occur at very similar positions. In liquid, it is at 3.55 Å and in hydrate 3.65 Å. The major difference lies in second peak and further onwards, which mainly reflects the structuring effect of methane. A small shoulder-like second peak at 4.35 Å followed by the third peak at 6.95 Å is seen in liquid water RDFs. In a hydrate system, the first peak has a corresponding valley at 6.25 Å, followed by the second peak extended further outward at 7.25 Å, followed by third peak at 9.45 Å.

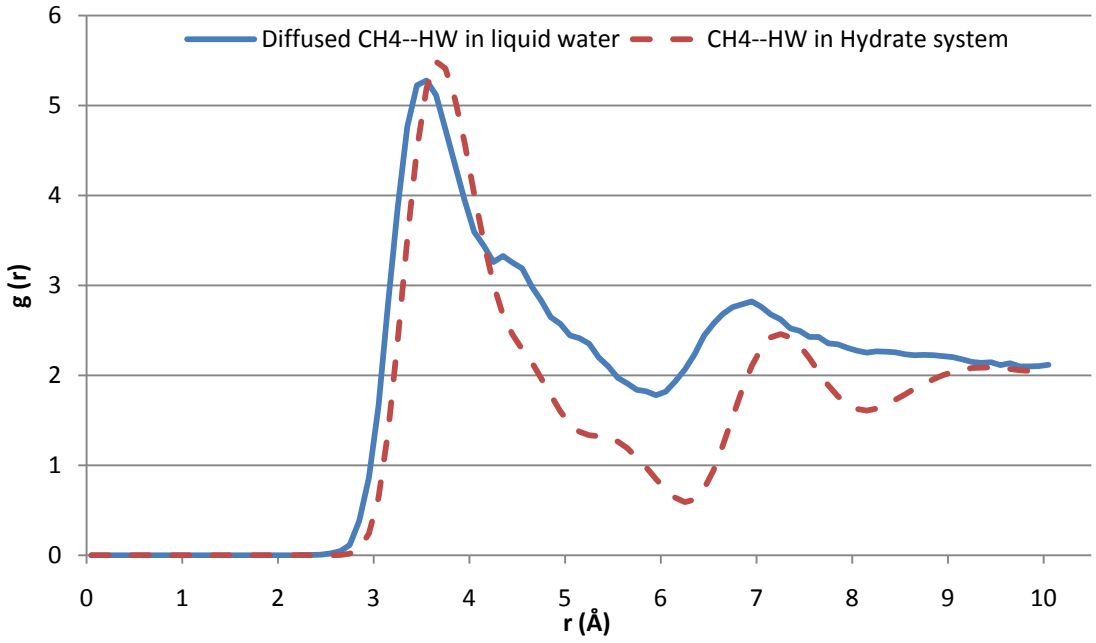

Figure 9-4: RDFs for methane—water hydrogen pair correlation.

The RDF of methane and water oxygens (OW) were also studied and showed very similar behavior. Integration of the CH4-OW RDFs to the first minimum at 5.5 Å resulted in a coordination number of 20 $\pm$ 1 water molecules, which is very close to the coordination

number for water in hydrate (21 $\pm$ 1). It can be stated that solvation cages formed around methane in liquid water shows a great resemblance to those formed in hydrate crystal.

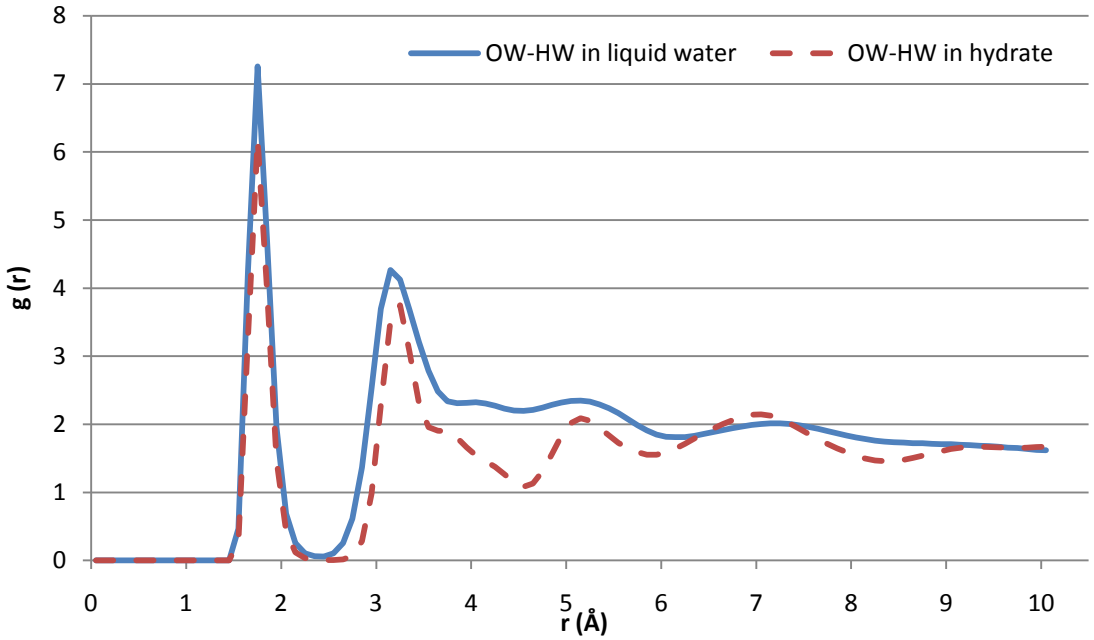

Figure 9-5: RDFs for water oxygen—water hydrogen pair correlation.

Further insights into processes occurring during the initial stage of nucleation can be inferred from the behavior of OW – HW correlation functions. Figure 9-5 illustrates the RDFs for OW - HW both in liquid water and in hydrate. The first (1.75 Å) and the third (5.15 Å) peaks in both liquid water and hydrate coincide with each other but the second peak is slightly shifted by 0.1 Å in hydrate. This may be due to hydrate being less dense than liquid water. Beyond the third peak the peaks are broader in liquid water than in hydrate. The RDFs indicated that the hydrogen atoms of liquid water orient themselves around oxygen atoms of liquid water very much like in hydrate water.

To study the effect of increased concentration of methane, Reference system II (RSII) was used; it will be discussed below.

The time evolution of RSII is presented in Figure 9-6. This system was run for a total of 102 nanoseconds. Nosé –Hoover thermostat was used after 99 nanoseconds to control the temperature. The higher methane concentration in this system would increases the driving force for hydrate formation. Early onset of nucleation was observed immediately after 1.3

nanoseconds in this supersaturated system as compared to RSI where the process was delayed until 29 nanoseconds. It demonstrated that the rate of diffusion of methane inside water phase increases with driving force.

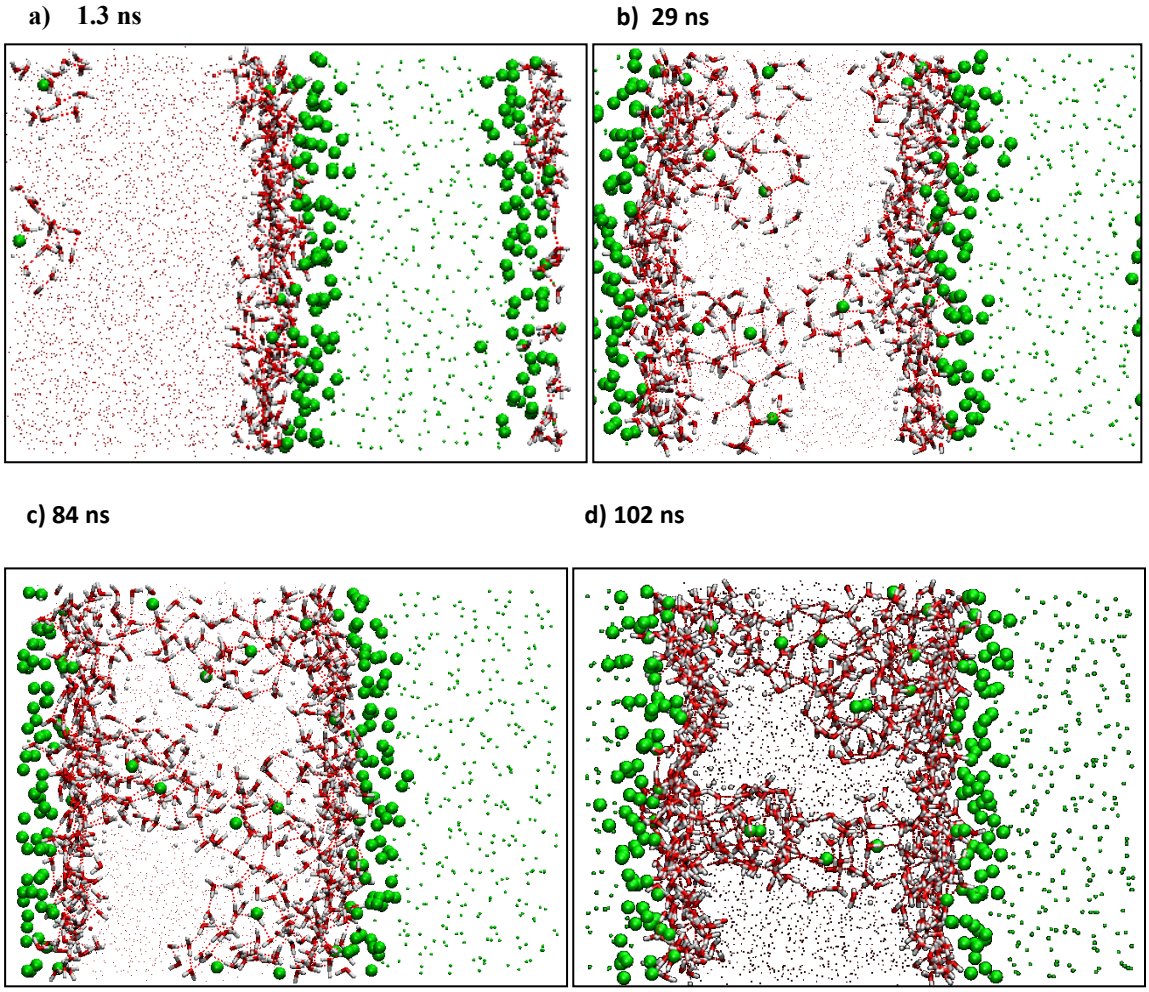

Figure 9-6: Reference system II, progress over time. After a) 1.3 ns b) 29 ns c) 84 ns d) 102ns.

The figure shows a vigorous diffusion of methane inside water phase. Water restructuring around methane resulted in formation of loose small and large cavities distributed throughout the water film. Eventually, there were 13 number of methane molecules completely dissolved in water. The interface between water and methane became more diffuse and wave-like. At some instances, the cavities exhibited facet sharing and attachment to the adjacent cavity formed by the new methane molecule. To obtain a closer look of cavity formation and face sharing, three diffused methane molecules close to each other were chosen and, they formed cavities by sharing facets as demonstrated in Figure 9-7. Only oxygen molecules of water are

presented to get a clearer picture. Oxygens at the maximum distance of 5.5 Å away from methane were selected.

The cut off distance and angle for hydrogen bonds in the VMD hydrogen-bond plugin, were set to 3.0 Å and 30°, respectively. The calculations indicated that liquid water in both RSI and RSII systems forms 1.42 bonds per oxygen atom on average. Orange colored oxygen represents the pentagonal phase shared. No facet sharing was observed between methane molecules labeled 1 and 2. It appeared that both 1 and 2 together was surrounded by water molecules. Pentagonal, hexagonal and heptagonal rings were formed. This is not consistent with SI methane hydrate where only hexagonal and pentagonal rings exist. As discussed earlier in section 3.3, the difference in the SI and SII structure stability is very small. This is also indicated by the fact that methane equally stabilizes both small and large cavity of SI hydrate. In SII, there are more small cavities but a less stabilization of the large cavity occurs due to methane.

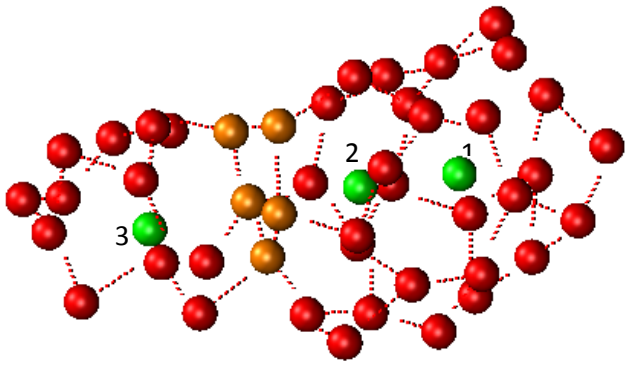

Figure 9-7: Cavity formation. (red dotted lines represent hydrogen bonding between water molecules, red and orange balls represent oxygen atoms of water, green balls are methane trapped inside cavities)

The analysis of density profiles provided a molecular-level view of the average distribution of molecules at the interface and inside the water phase. The profiles were generated using the same procedure as for RSI. At the beginning, the sharp interface between water and methane phase was observed, and was similar to that in RSI except for the average density of bulk methane phase (0.53 g/cm^3). Density profile generated at the end of the run (Figure 9-8) confirms the vigorous diffusion of methane molecules into the water phase. Compared to RSI (Figure 9-3), the interface in this system became diffuse with higher peaks of methane seen in water close to the interface. The water peaks appeared more structured and decrease in water

density corresponding to methane insertion is easily detected. The hydrophobic nature of methane molecules resulted in restructuring of water molecules around it.

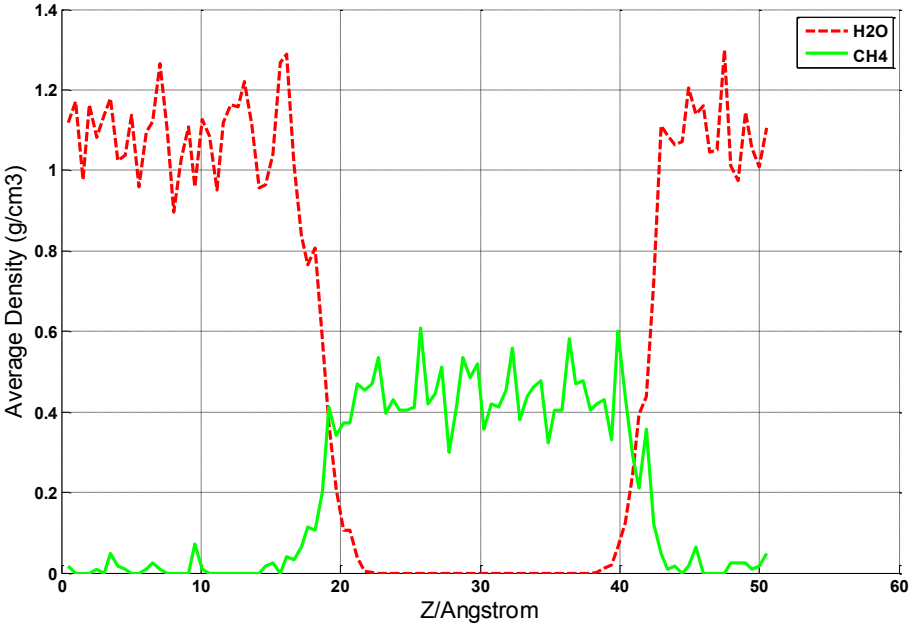

Figure 9-8: Density profile at the end of simulation. (Reference system II)

The structure of the water shell around methane can be characterized by means of CH4- OW pair correlation function. These were generated for methane and water oxygen close to the methane. Figure 9-9, indicated that the typical carbon-oxygen distance in the liquid water was about 3.55 Å, compared to about 3.85 Å in the hydrate. The water shell around methane in liquid water is therefore tighter than the one in hydrate. The liquid water second peak was shifted inwards to 6.35 Å as compared to 6.65 Å in case of hydrate, due to the lower density of hydrate. The peaks beyond the second one are flattened in liquid water in contrast to more structured peaks in crystal hydrate. By integrating the RDF of CH4-OW to its first minimum at r = 5.5 Å, the methane coordination number in the liquid was found to be 17 $\pm$ 1 water molecules. This is considerably smaller than the 21 $\pm$ 1 water molecules in hydrate and 20 $\pm$ 1 water molecules in RSI. RDFs for methane and liquid water hydrogens (HW) exhibited behavior closely resembling that of the RSI.

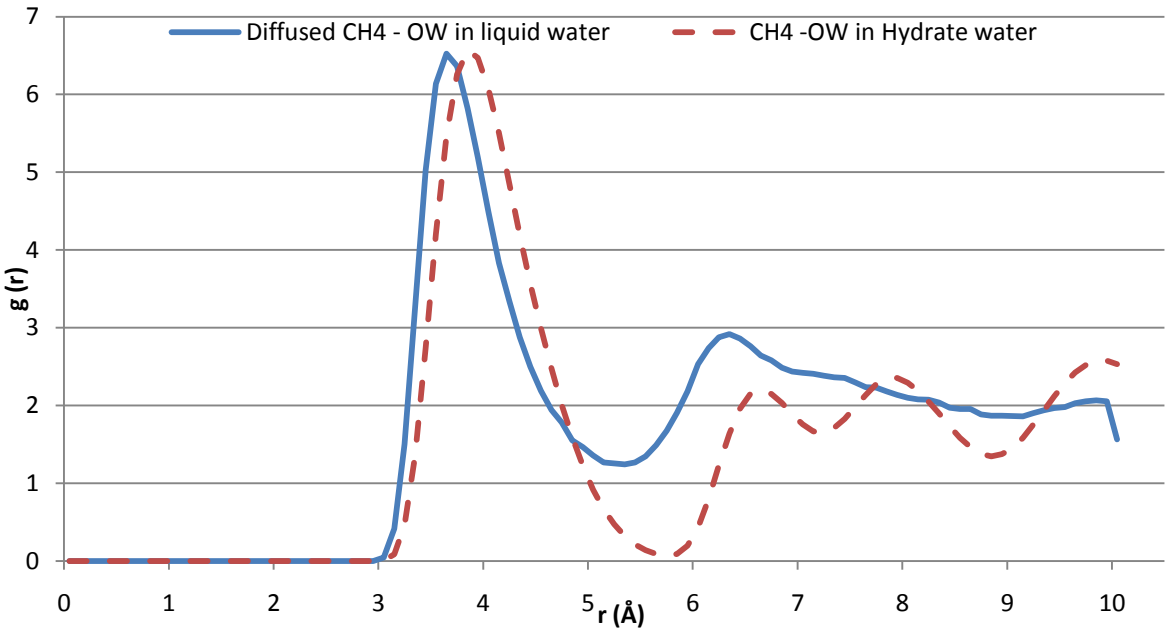

Figure 9-9: RDF for methane—water oxygen in liquid water and hydrate system.

Figure 9-10 presents the comparison of RDFs for OW – OW in liquid water both beyond and within 6.0 of dissolved methane with that in hydrate. The first peak is at same position of r = 2.75 Å in all the cases, indicating the distance between the nearest two oxygen atoms in water. The second liquid water peak is shifted inward compared to hydrate, while the third peak is somewhat flattened in liquid water.

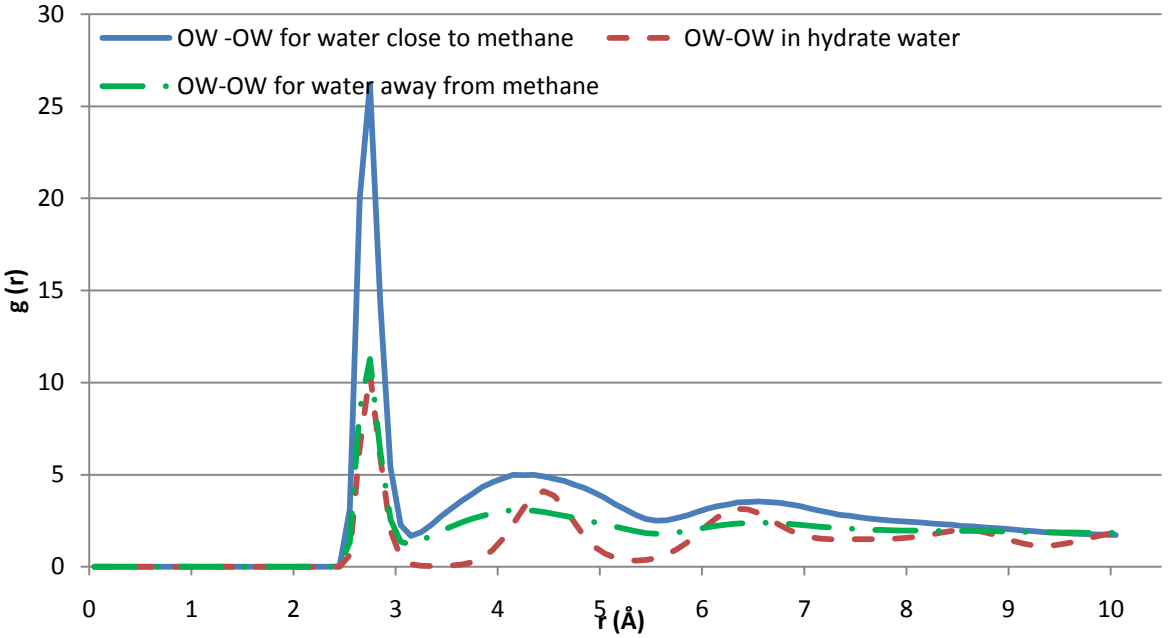

Figure 9-10: RDFs for water oxygen—water oxygen (Reference system II).

Except for the heights, the general RDF behavior in liquid water was very similar for water oxygen far way and close to methane. The second and third peak emphasizes the structured nature of solid hydrate. The structuring of water molecules close to the dissolved methane indicates that the nature of the hydration shell in liquid water is somewhat similar to that in the hydrate crystal.

The intermolecular energies estimated for both RSI and RSII are listed in Table 9-A. Note that the energies obtained are given on the whole system basis and refers the total number of moles present in the system. Short-range interaction potential energies points to the more attractive nature of molecules in RSI than RSII. The electrostatic attraction between water molecules is more favorable in RSII than RSI.

Table 9-A: Intermolecular Energies (RSI & RSII)

	Short Range interaction energies (kJ/mol of the total system)		**Electrostatic intermolecular energies (kJ/mol of the total system)**	
	RSI	**RSII**	**RSI**	**RSII**
$H_2O—H_2O$	12.8326 $\pm$ 0.0021	12.8568 $\pm$ 0.0025	-73.7099 $\pm$ 0.0677	-74.9382 $\pm$ 0.0778
$H_2O—CH_4$	-2.7373 $\pm$ 0.002	-2.2325 $\pm$ 0.0006	0.0	0.0

9.2 PVCap system I

To distinguish between the two sets of partial charges used, the system using PVCap model with the LPA charges will be referred to as PSI-L, and the system with the CM4 charges, as PSI-C. In this section, we will first discuss the results obtained from the PSI-L. The final state of the PSI-L system is shown in Figure 9-11. PVCap is represented by a continuous surface. The total run duration in this system was 118.8 nanoseconds. Right from the start of the simulation, the two PVCap molecules showed the tendency to position themselves close to the water - methane interface. Initially, the bulk of PVCap1 was positioned on the waterside of the interface and it gradually drifted more towards methane side by the end of simulation. To sample the thermodynamic properties and get the approximated canonical ensemble, Nosé – Hoover thermostat for temperature control was switched on after 96 nanoseconds of simulation. In the RSI, the early diffusion of methane in water phase was observed after 29 nanoseconds as opposed to the present system containing two PVCap dodecamers, for which

no significant diffusion of methane in water phase was observed. It was concluded that PVCap slowed down the diffusion of methane in water phase.

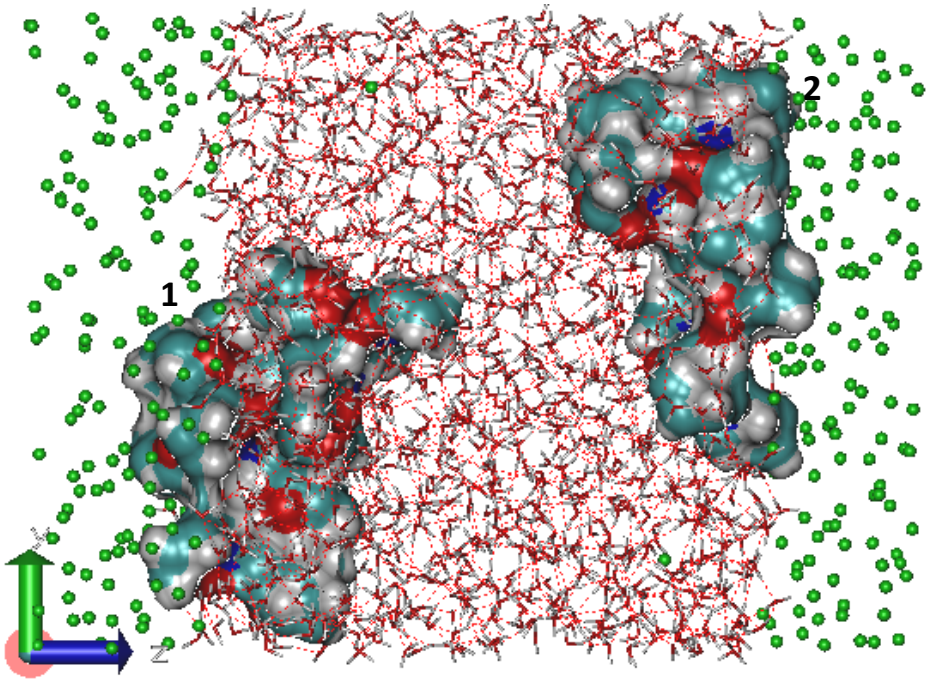

Figure 9-11: PVCap system I with LPA charges after 118.8 nanoseconds.

This will obviously affect and delay the hydrate nucleation and formation. Visual examination showed that PVCap1 was more immersed in water as compared to PVCap2. The PVCap molecules kept their distance from each other and showed no apparent affinity towards each other. PVCap1 extended across y-z plane whereas PVCap2 extended across the y-axis, approximately at an angle of 90°.

Density profiles were generated separately to focus on the two PVCap molecules individually. This was done so that the density distribution around each PVCap molecule would not be smeared by the presence of undisturbed methane and water. The profiles were generated by partitioning the simulation box into 100 bins in z direction (0.5 Å per bin). Only 2 frames were used, corresponding to 2000 time steps since the system drifted very fast across the box due to the PBC. To get the accurate profiles, specific frames were chosen in which the two PVCap molecules were not overlapping with each other in x-y plane and both of them remaining inside the box. This was needed, as PBC are not handled in density profile code.

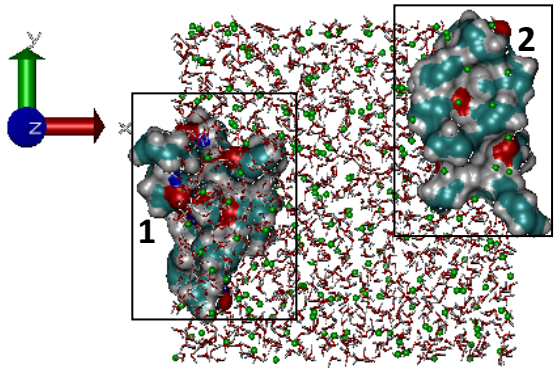

Figure 9-12: Scheme for generating density profile

Figure 9-12 represents the x-y projection of boxes 1 and 2 used to generate density profiles for PVCap1 and PVCap2, respectively. The approximate location and extent of PVCap1 and PVCap2 in x and y plane at that instance was found using VMD. Figure 9-13 and Figure 9-14 shows the density profile for PVCap1 and PVCap2 as well as water and methane molecules present in this cutout section. It is obvious that each PVCap molecule was positioned at the interface but more inside water than methane. The minima of the PVCap peaks coincide with the maxima of water peaks and vice versa.

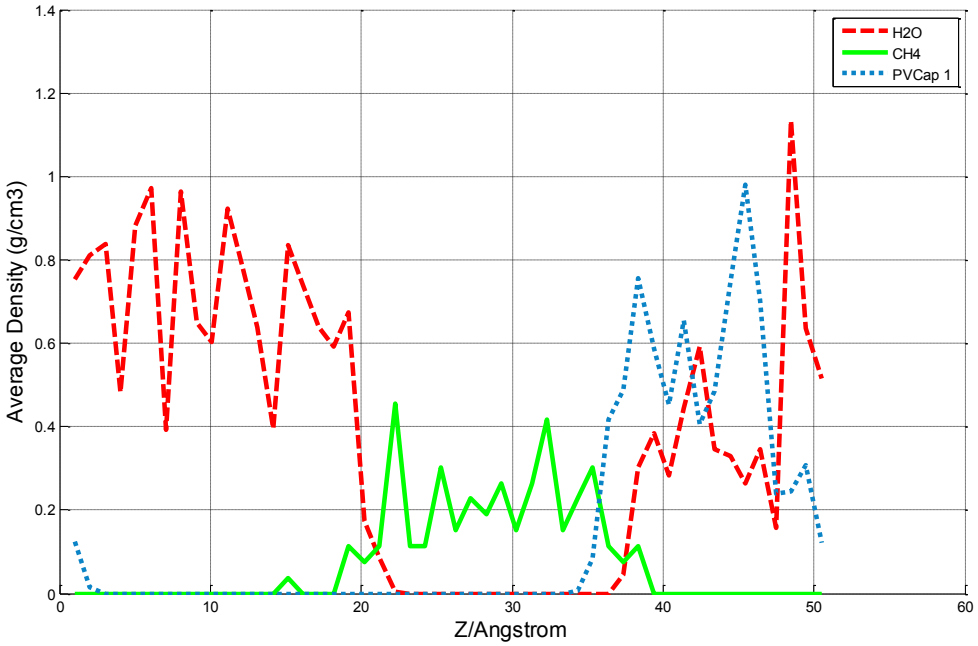

Figure 9-13: Density profile for PVCap1 in PSI-L system.

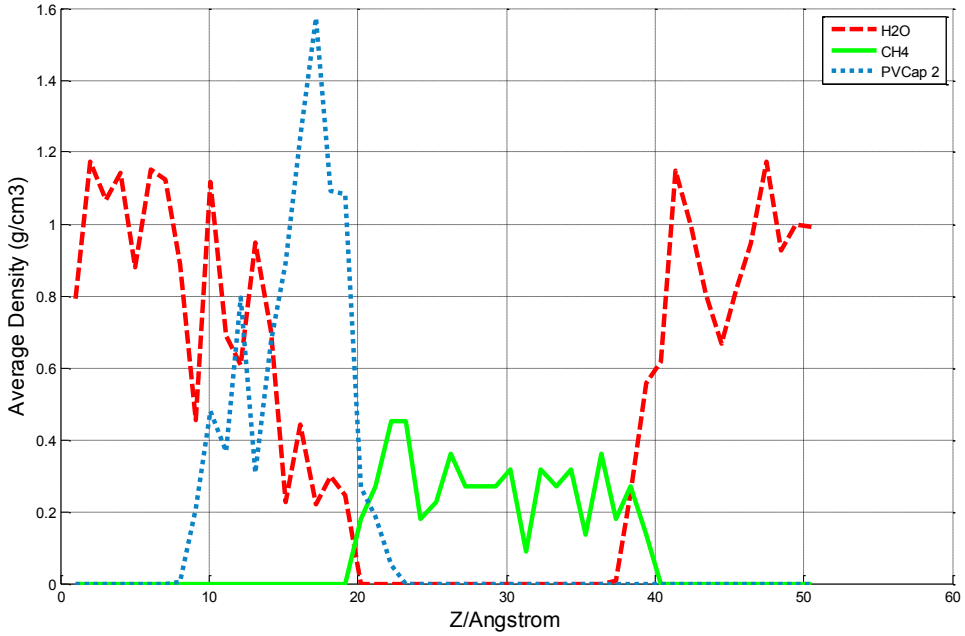

Figure 9-14: Density profile for PVCap2 in PSI-L system.

The analysis of density profile makes it very clear that PVCap affects the interface between water and methane. The water in the vicinity of PVCap showed the presence of small peaks and more ordered behavior as compared to interface water in the absence of PVCap (RSI). It was also evident that both PVCap molecules had most of their bulk immersed in water and were not interacting much with the hydrophobic methane molecules.

Various RDFs calculated for the PVCap especially concentrated on the carbonyl oxygen of PVCap because this is the site most likely to be responsible for structuring of water (Carver 1999).

Figure 9-15 indicates that the first peak for both the PVCap molecules was located at 2.65 Å, which corresponds to a shift of 0.1 Å compared to OW-OW in liquid water. In case of PVCap2, this peak is followed by a second small peak at 4.15 Å, which is in turn followed, by three height insignificant peaks resulting in the flattening of the third peak. The second peak in PVCap1 is higher than that in PVCap2 indicating that PVCap1 is further inside the water than PVCap2. The third peaks in PVCap1and PVCap2 are at the same position with just 0.1 Å inwards to OW-OW, showing the similarities between the PVCap and liquid water oxygen.

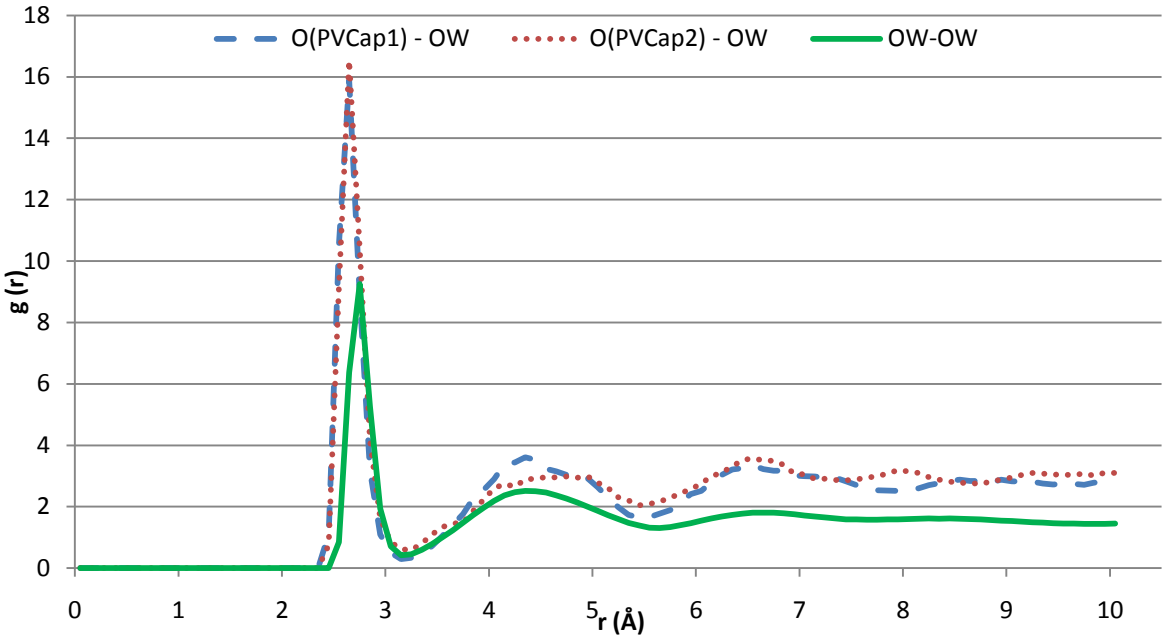

Figure 9-15 RDFs for carbonyl oxygen in PVCap & water oxygen, compared with distribution of water oxygen alone.

Figure 9-16 present RDFs for hydrogen atoms (H) connected to PVCap's backbone with methane and with OW. Backbones of either PVCap molecules showed no strong interactions or affinity towards methane.

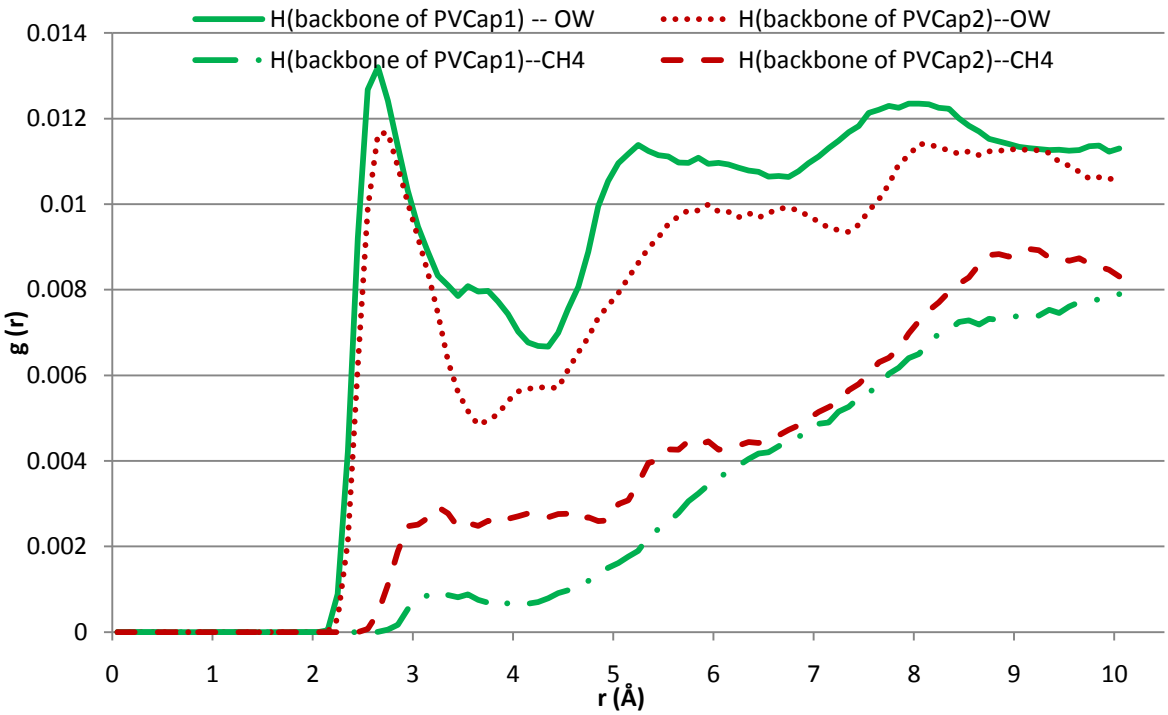

Figure 9-16: RDFs for Hydogen (PVCap Backbone) with methane and with water oxygen.

The curve behavior indicates that they actually preferred positions away from methane. The number integral value indicated that not even a single methane molecule was present up to a distance of 6.5 Å. Analysis of pair correlation functions between PVCap backbones and water oxygen revealed a strong first peak indicating the preferred position of water molecules close to the backbone. Water molecules around backbone of PVCap1 appeared more structured than for PVCap2, again reflecting to the fact that PVCap1 is more inside water and hence more interaction with water than PVCap2.

Figure 9-17 presents the pair correlation function for interactions between the nitrogen of PVCap ring and water oxygen (N--OW) and hydrogen (N--HW). These RDFs indicate that nitrogen atoms of the PVCap molecule did not have any affinity for water interaction and hence most possibly are not directly responsible for restructuring of water molecules.

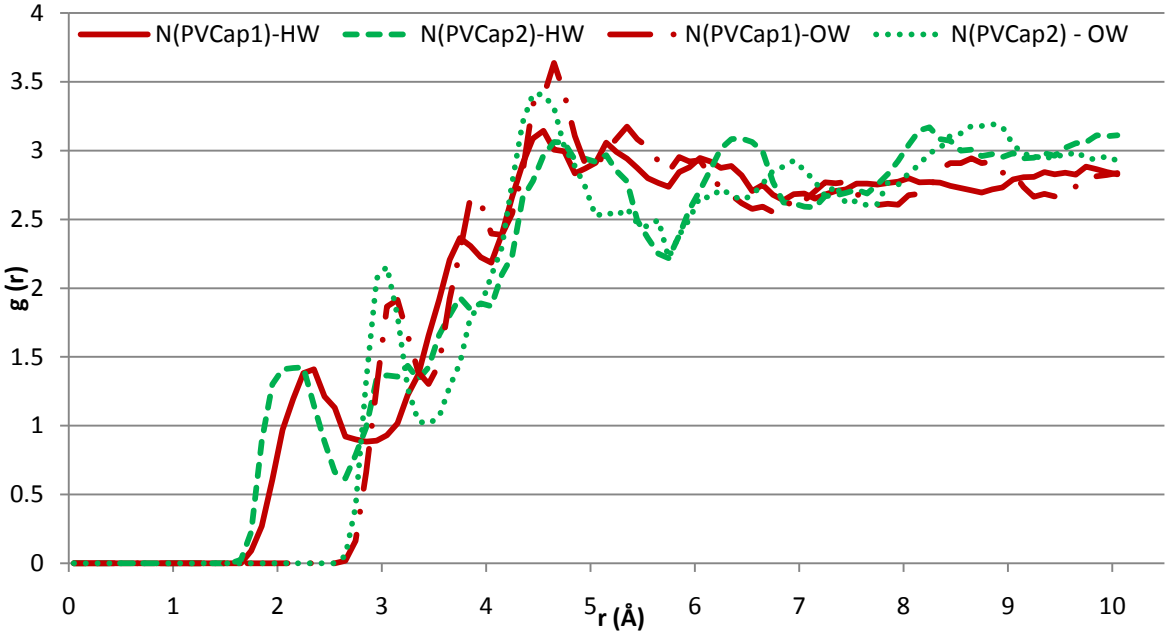

Figure 9-17: RDFs for Nitrogen (PVCap) with water oxygen and methane.

Hydrogen bonding is observed to be mainly responsible for hydrate formation. To learn whether PVCap contributes to restructuring of water by forming hydrogen bonds, the number of hydrogen bonds formed between carbonyl oxygen of PVCap and liquid water were calculated using VMD. On average, PVCap1 and PVCap2 formed 1.28 and 1.10 bonds per oxygen respectively, as compared to 1.39 bonds per oxygen in liquid water. Since the number of hydrogen bonds formed in RSI was on an average 1.42 per water oxygen, this indicates that the presence of PVCap decreases the degree of hydrogen bonding in liquid water. This

hydrogen bonding between PVCap oxygen and water hydrogen increased as the system evolved with time since at the start of simulation there were 0.316 hydrogen bonds formed per oxygen of PVCap. This indicates that PVCap molecule is positioning itself favorably to interact with water, form more hydrogen bonds, and hence decrease the hydrogen bonding possibility available to water molecules.

Since PVCap is a surfactant, it should reduce the interfacial tension and we have thus calculated interfacial tension for the last 2000 intermediate averages using equation (8-2). These results are plotted in Figure 9-18. The average interfacial tension was observed to be uniform and amounted to 0.1421$\pm$0.0019 N/m at the end. Similar calculations were performed for RSI containing no PVCap. In this reference system the fluctuation in interfacial tension was observed due to wide variation in system pressure with the average value at the end found to be equal to 0.1822 $\pm$ 0.00164 N/m as indicated in Figure 9-19.

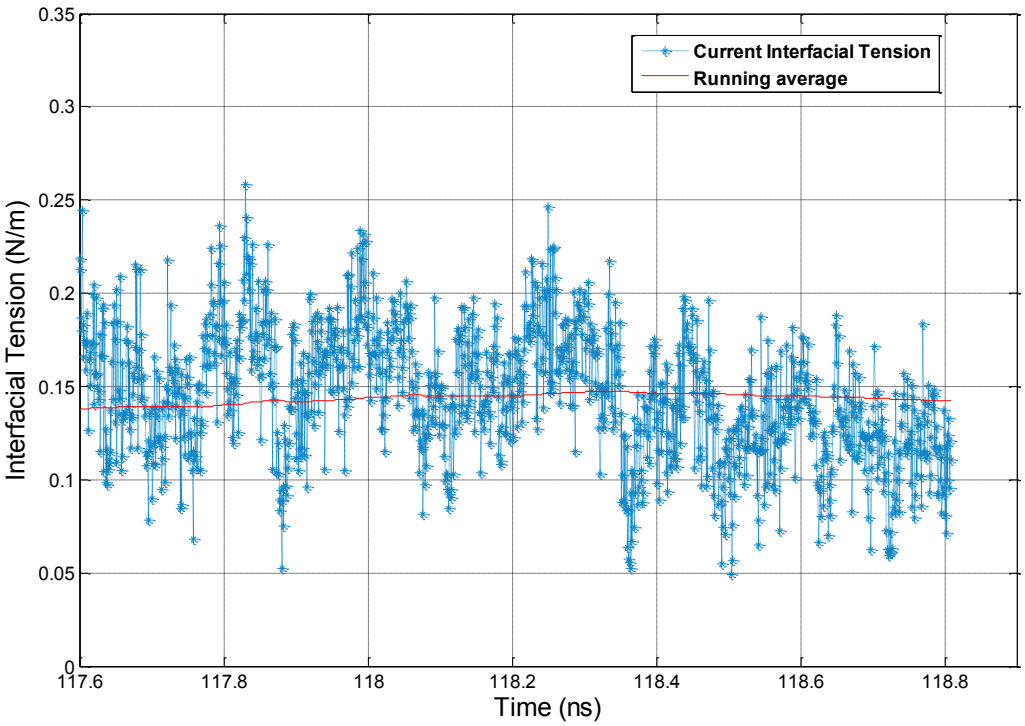

Figure 9-18: Interfacial tension in PSI-L system.

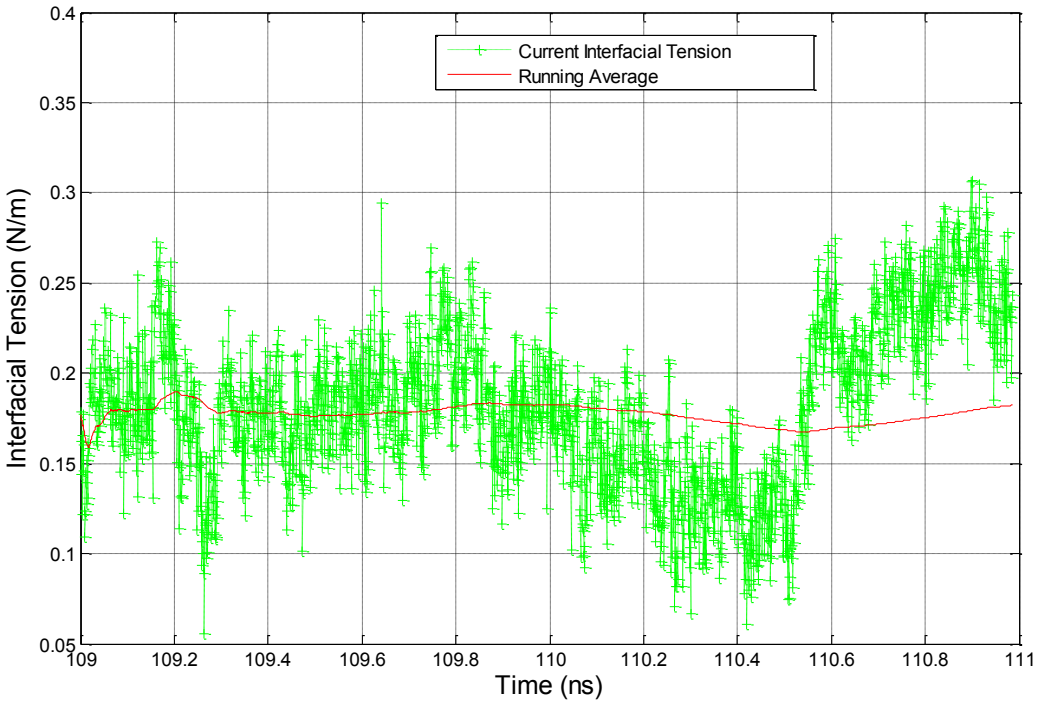

Figure 9-19: Interfacial tension in RSI system.

md43 tend to overestimate the interfacial tensions when using flexible molecules, so to consider these values as absolute may not be accurate. But comparing the values for both the system with and without PVCap does show that the interfacial tension is reduced approximately by 22 % due to the presence of PVCap.

Due to time limitations, the PSI-C system was run for 25.78 nanoseconds. After about 21.13 nanoseconds into the simulation run, Nosé-Hoover thermostat was switched on to, control the temperature. No diffusion of methane into the bulk water phase, observed in the PSI-L system, was detected in this system. As expected, the use of CM4 charges did affect the orientation of PVCap molecules to a significant extent. Figure 9-20 demonstrates the difference in the PVCap positioning. This figure consists of four snapshots. The first and second snapshots show the position of PVCap1 in PSI-C and PSI-L system respectively, while the third and fourth snapshots indicate the position of PVCap2 in PSI-L and PSI-C systems. To highlight the difference in the orientation of backbone and ring, backbones are indicated in mauve and orange color for PSI-C system and PSI-L system respectively.

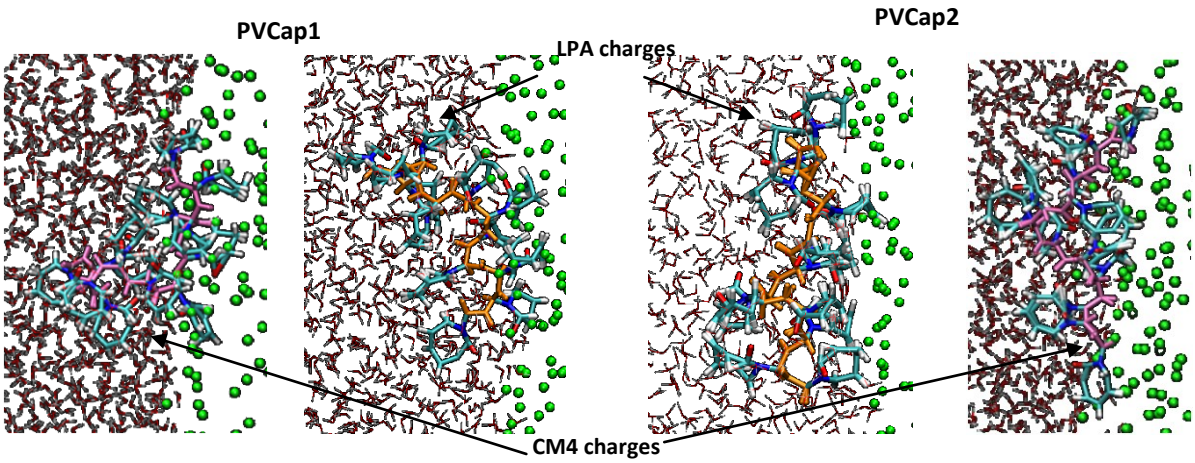

Figure 9-20: Orientation of PVCap molecules corresponding to charges

It is evident from the figure that LPA charges resulted in most of the backbone being shielded by rings in contrast to the CM4 charges. Also with CM4, the orientation of rings was biased towards water rather than methane. PVCap1 in both systems preferred a position close to the interface but more inside the water than PVCap2. It appeared that even during the shorter run PVCap with CM4 charges already started to orient itself so that its backbones would interact with methane and rings with water. In this system, the conformation of PVCap1 molecule was different from PVCap2 as indicated by the RDFs in Figure 9-21 and Figure 9-22 respectively. RDFs used the following abbreviations: N for nitrogen, CO for carbonyl carbon, C (Ring) for carbon atom in the ring and C (Backbone) for carbon atom in the backbone. N(PVCap)—N (PVCap) pair correlation function and the pair correlation function between the CO(PVCap)-CO(PVCap) appeared to indicate that PVCap2 nitrogen and carbonyl carbon were more structured as seen from the sharp peaks. The pair correlation function of the ring carbon that was located directly opposite to the nitrogen atom C(Ring)—C(Ring) pointed out the fact that the rings were spreading on both sides of the backbone in PVCap1, whereas the sharper peaks in PVCap2 reflects that more rings were pointing towards only one side of the backbone. This confirms that at interface the rings will prefer to orient itself towards water rather than methane thus increasing the possibility of hydrogen bonding with water molecules. The sharp first three peaks observed for C (backbone)—C(backbone) RDF for PVCap1 also indicates a more structured ordering in the backbone. This was not the case with LPA charges, where the rings were shielding the backbones of both the PVCap molecules and no significant interaction was observed between backbone and methane.

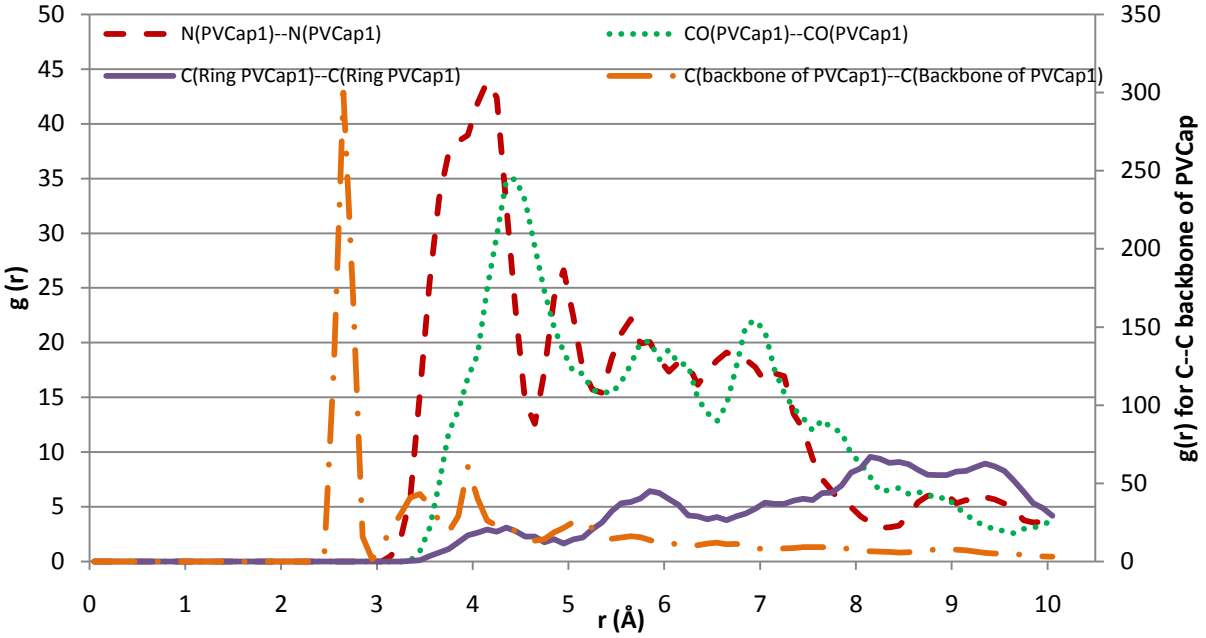

Figure 9-21: Structuring of atoms of PVCap1 (PSI-C system)

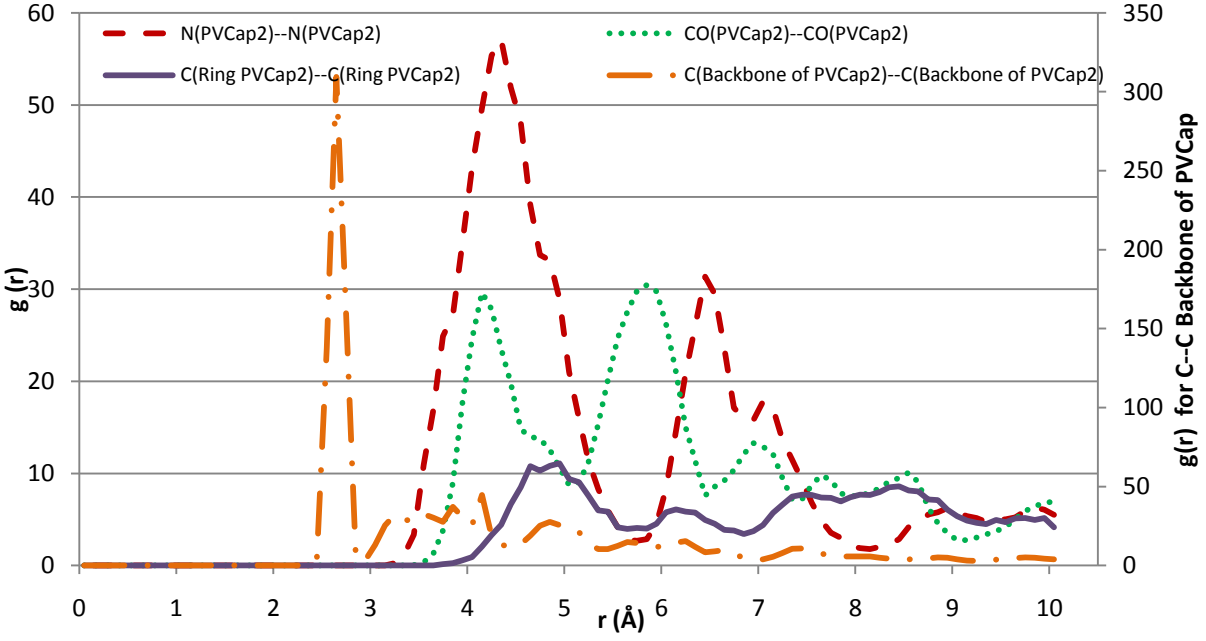

Figure 9-22: Structuring of atoms of PVCap2 (PSI-C system)

However, the simulation run was not long enough to reach complete equilibrium. By the end of the 25.78 nanoseconds, the interfacial tension was 0.144 ± 0.00145 N/m and showed the decreasing trend. Although the total energy of the system did not vary much, the overall pressure, which is always the last property to equilibrate, still fluctuated dramatically. Because of the drastic pressure fluctuations, the interfacial tension calculated in this system

would be unreliable. To study the detailed effect of charge distribution and compare the thermodynamic properties of this system with PSI-L, longer simulation runs are needed. Average energy contribution due to the short-range interactions and electrostatic interaction between two different types of molecules are listed in Table 9-B.

The electrostatic energies of PVCap—PVCap interactions indicate a much stronger repulsion between the PVCap molecules in the PSI-L system compared to the PSI-C system. In addition, the Coulombic interactions between PVCap and water were approximately 68% less in magnitude in PSI-C than PSI-L. This indicates that the interaction between PVCap and water is stronger in the PSI-L system. This is an obvious consequence of the charge distributions as discussed in section 8.1.3. Most of the PVCap atoms with the CM4 charges are close to neutral as compared to the LPA charges where all the carbon atoms except for the carbonyl carbon are negatively charged, and all the hydrogen atoms having positive charge. Because of this, LPA-generated backbone will also prefer to interact with water rather than with united-atom methane molecules, thus contributing to the overall interaction between PVCap and water molecules. This fact could also explain the difference in PVCap orientation. The short-range interactions between water molecules also become less repulsive in PSI-L system than in RS-I(Table 9-A) and PSI-C system. The situation may change if 5-site methane model is used instead of one-site model. It would be instructive to study the effect of 5-site methane molecule.

Table 9-B: Intermolecular Energies (PSI).

	Short Range interaction energies (kJ/mol of the total system)		**Electrostatic intermolecular energies (kJ/mol of the total system)**	
	LPA Charges (PSI-L)	**CM4 Charges (PSI-C)**	**LPA Charges (PSI-L)**	**CM4 Charges (PSI-C)**
PVCap—H_2O	-267.1372 ± 0.1517	-325.4538 ± 0.0675	-2344.008 ± 8.892	-753.8188 ± 4.8766
PVCap—CH_4	-136.1015± 0.1579	-219.5328 ± 0.1427	0.0	0.0
PVCap--PVCap	-0.0151± 0.0001	-0.0235 ± 0.0001	7.5991±0.3234	0.7117 ± 0.0233
H_2O—H_2O	12.577±0.0027	12.8431 ± 0.0018	-71.8237±0.083	-79.4628 ± 0.0932
H_2O—CH_4	-2.1206±0.0017	-2.0242 ± 0.0015	0.0	0.0

9.3 PVCap system II

PVCap molecules with LPA charges in PSII behaved very differently from PSI-L despite of the number of PVCap molecules being the same. Some of the differences may be attributed to the initial positions of the PVCap molecules and the more pronounced hydrodynamic effects of a denser methane phase. Behavior observed in PSII system with the LPA charges (PSII-L) can be due to the distribution of partial atomic charges. Results obtained in the PSII-L system will be discussed first. This system was simulated for 135.4 nanoseconds. Nosé –Hoover thermostat was switched on to control the temperature at 106.5 nanoseconds into the simulation to enable sampling of the true thermodynamic properties. As indicated in Figure 9-23 showing the final state of the system, the PVCap molecules exhibited different behavior while staying close to each other. PVCap2 was completely immersed in water whereas PVCap1 was lying at the interface between water and methane. Large number of methane molecules ended up inside the bulk water thus markedly enhancing the possibility for hydrate formation.

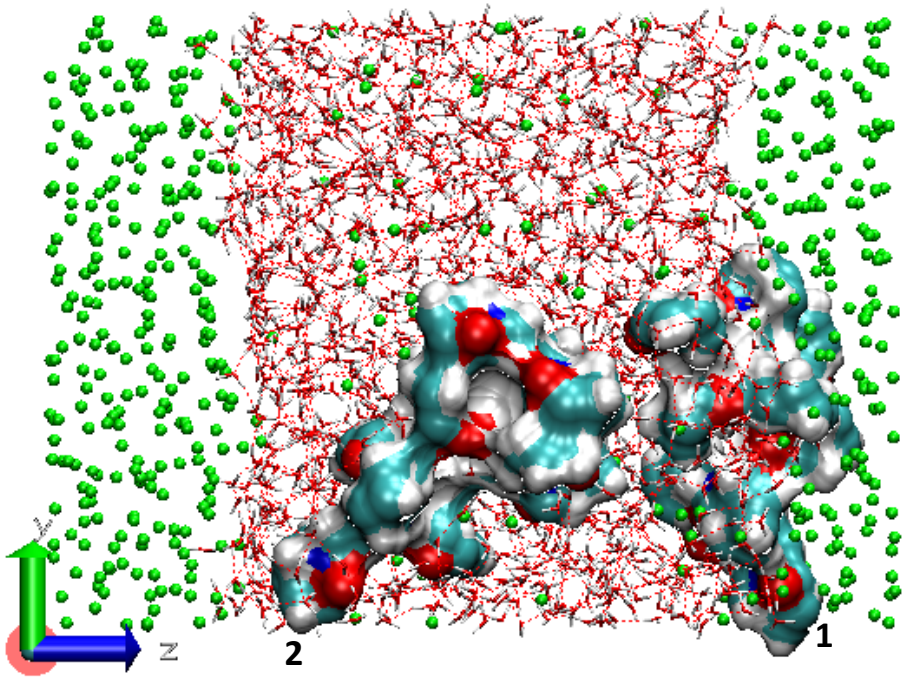

Figure 9-23: PVCap system II with LPA charges after 135.4 ns

Figure 9-24 demonstrates the time evolution of the system showing how PVCap molecules arrived at the position they are found at the end of the simulation. These snapshots may also indicate how the PVCap molecules promote the nucleation process. At the beginning of simulation, both PVCap molecules were located close to the interface and positioned across

each other (frame 1). Given the relatively high affinity for each other, PVCap2 molecules (orange continuous surface) entered into the methane bulk drifting towards the other PVCap1 (blue continuous surface) (frame2). After 63 picoseconds of simulation (frame3), PVCap1 made its way inside the bulk water phase dragging a number of methane molecules inside water along with it. PVCap2 was completely inside the methane bulk.

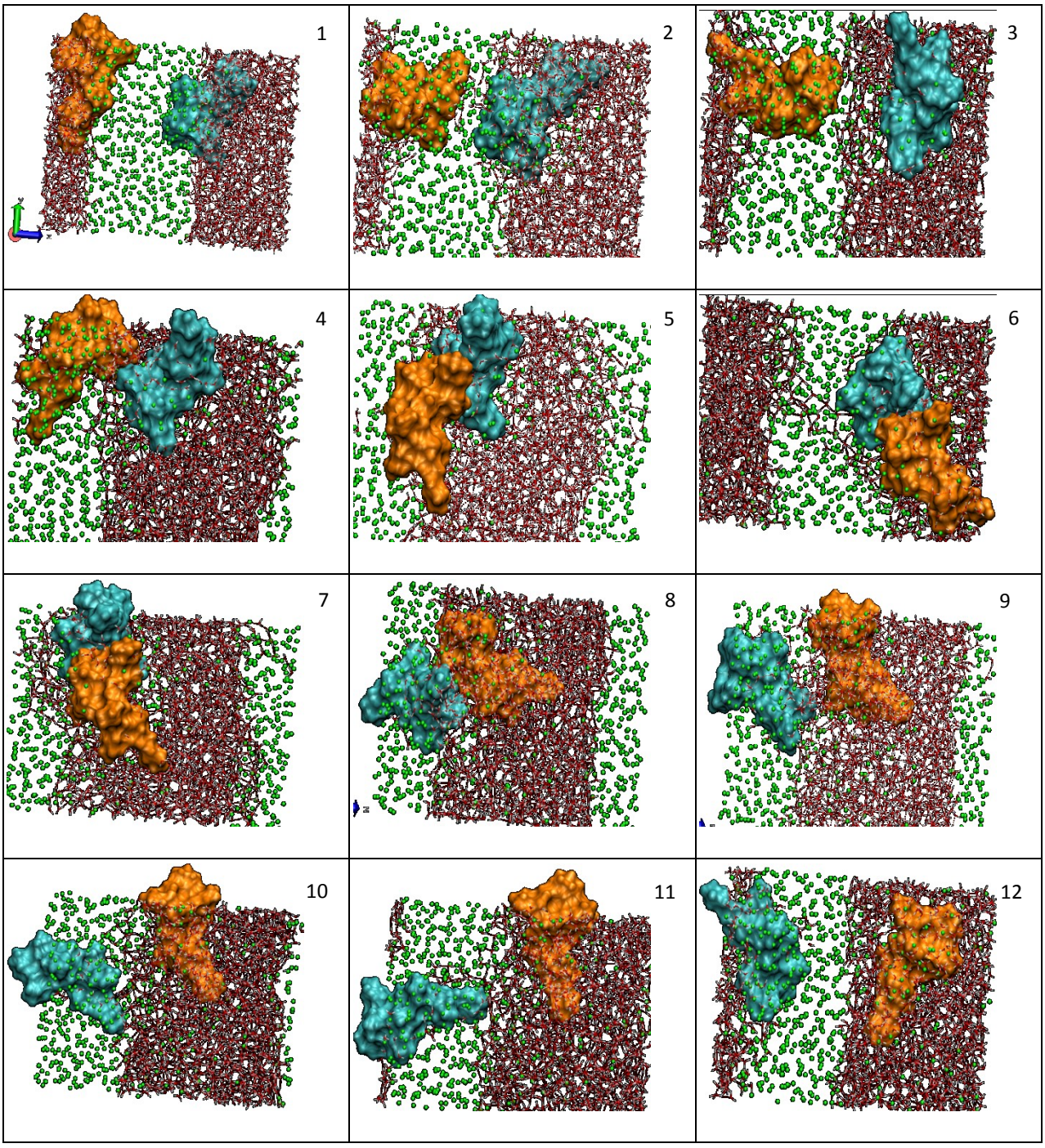

Figure 9-24: Snapshots of early system evolution. (PVCap1 represented by blue continuous surface and PVCap2 by orange continuous surface)

PVCap2, with its strong affinity for the other PVCap and water, immediately crossed the methane bulk and migrated towards PVCap1 in bulk water phase (frame5). A trail of water molecules followed the PVCap2 and formed a bridge between the two interfaces (frame6). Since the bulk water phase was apparently not large enough, PVCap1 was pushed towards the bulk methane phase after a few picoseconds carrying molecules of water along with it(frame 10). After 148 picoseconds, it was observed that PVCap1 positioned itself at interface between water and methane and PVCap2 remained inside the bulk water phase (frame12) quite close to PVCap2. Both PVCap molecules then preferred these positions for the rest of the simulation run. In contrast to PSI-L, this system promoted the dissolution of methane into water rather than inhibited it.

One might be tempted to explain this curious behavior by the possibility that much higher pressure in the system has been able to overcome the inhibitor influence, similarly to a very high degree of sub-cooling. The system had 40+ methane molecules dissolved inside water as compared to 2 in PSI-L and 13 in RSII. Nevertheless, the major reason behind this type of behavior should be attributed to the distribution of partial charges. As discussed in section 8.1.3, PVCap charges obtained from the LPA are quite different from those calculated from the CM4. When the mutual orientation of PVCap1 and PVCap2 was favorable, i.e. when the oppositely charged atoms of the two PVCap molecules were facing each other, the strong attraction between the two PVCap molecules could be seen (frame 2 to 7). The moment the like charges on individual PVCap molecules faced each other, repulsion occurred as seen in frame 8 to 10. The electrostatic interaction between PVCap1 and PVCap2 were so strong that allowed them to drag the neutral methane molecules inside water (frame 2 and 3). Also, since the carbonyl oxygen is more negative in LPA with an average charge of -0.54, it might form stronger hydrogen bonds with water, causing a trail of water molecules through the methane phase (frame 6). This indicates that the distribution of partial atomic charges on PVCap molecule will play a major role, promoting the diffusion of methane inside water as compared to the system without PVCap molecules. For the future work, it will be instructive to study the PVCap behavior in a larger system with water phase able to accommodate both the PVCap molecules without causing any possible drift of the PVCap and subsequently forceful injection of methane inside water. Since the interaction between PVCap and water molecules is stronger, this may lead to a strongly inhibited system with reduced water – water and water-methane interaction.

Density profiles were generated focusing on each of the PVCap molecule separately. The procedure followed was the same as for PSI-L. Figure 9-25 and Figure 9-26 present the density profiles across PVCap1 and PVCap2 respectively. The density profiles also indicate that PVCap1 lies at the interface and PVCap2 in bulk water phase. In addition, the interface in this system is more diffuse compared to the RSII. A large number of methane molecules have been transferred inside water and that can be observed through these profiles.

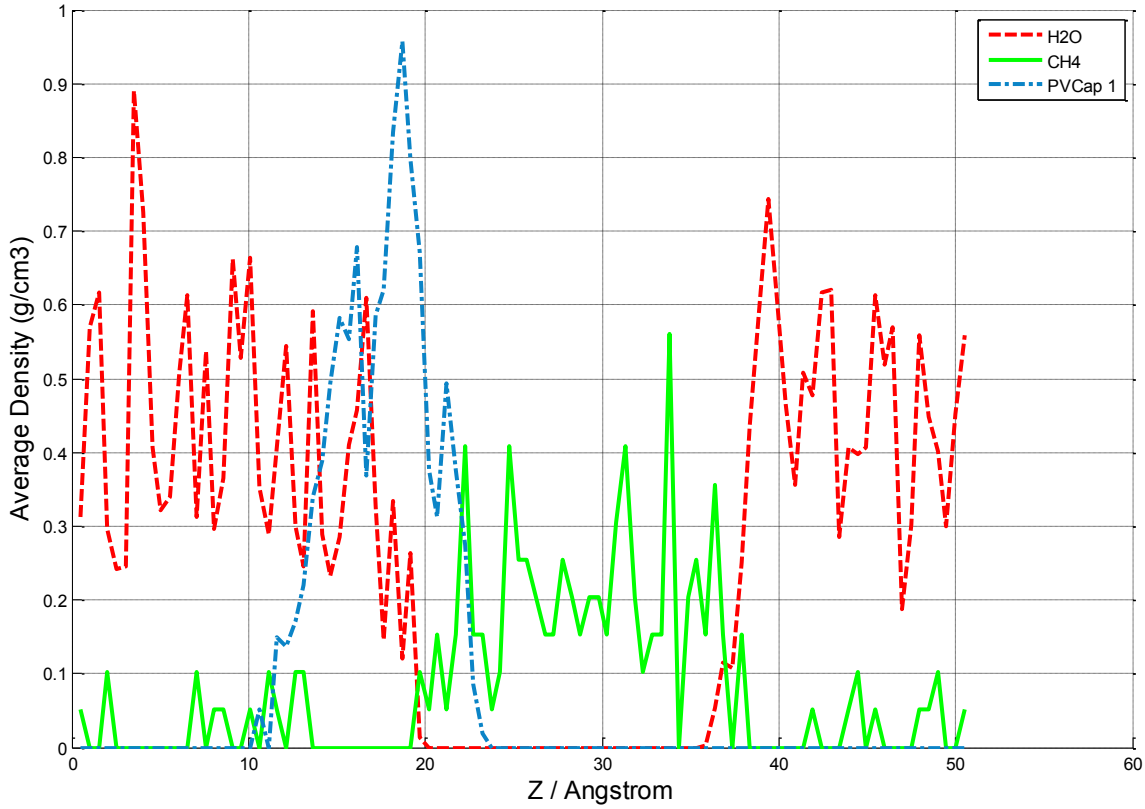

Figure 9-25: Density profile projected across PVCap1 for PSII-L system.

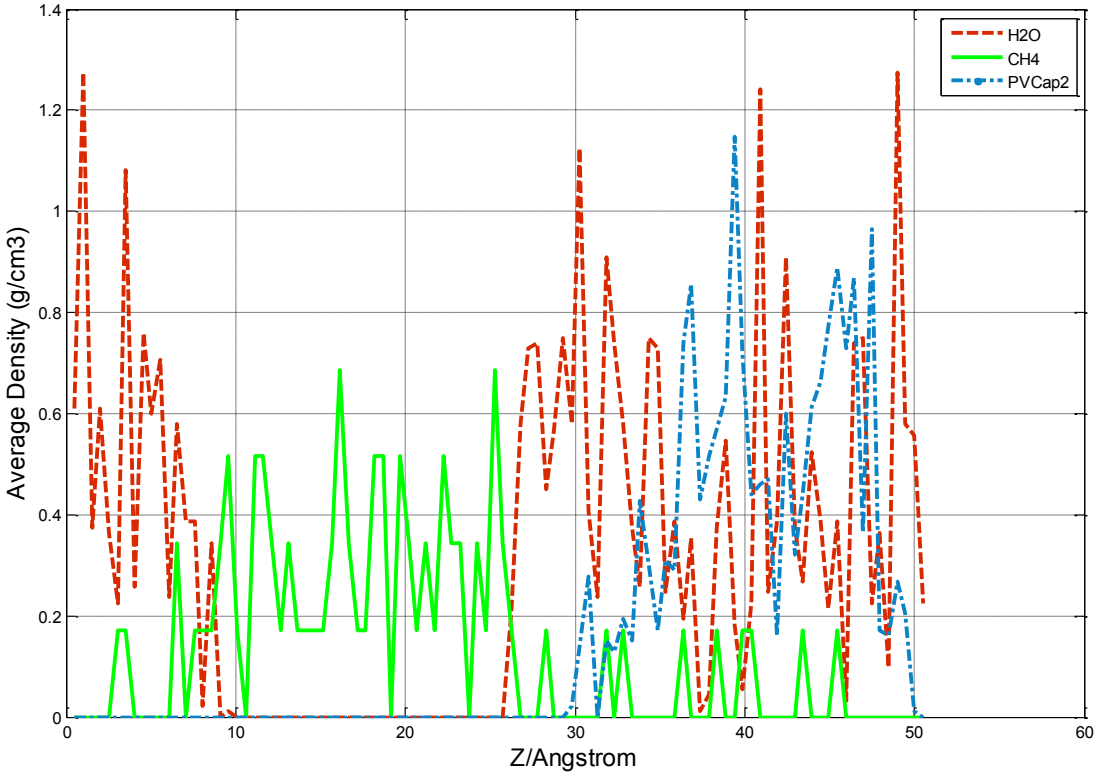

Figure 9-26: Density profile projected across PVCap2 for PSII-L system.

Figure 9-27 presents the behavior of the PVCap backbone. Since, carbon atoms in the backbone are shielded by the hydrogen atoms, the interaction of backbone hydrogen atoms with methane molecules and water oxygen's was the one studied. The backbone of PVCap1, showed more preference towards water than methane. Visual inspection of trajectories demonstrated that even though PVCap1 is located at the interface, there are about four rings between the backbone and the methane phase, which hinders the direct interaction between methane molecules and backbone. In spite of this, the second sharp peak of the H (backbone of PVCap1) -CH4 RDF indicates some structuring of methane molecules around backbone. Water oxygen around this backbone is also quite structured as indicated by the first two peaks, which are of the same height. In addition, the peaks for methane molecules are smaller and slightly shifted to the right compared to the water oxygen. In contrast, dissolved methane molecules showed better structuring around PVCap2 backbone than water oxygen. The rising nature of the RDF for H (PVCap2) – OW indicates that water molecules are keeping away from PVCap2 backbone, thereby conforming the fact that backbone will interact more vigorously with methane that with water.

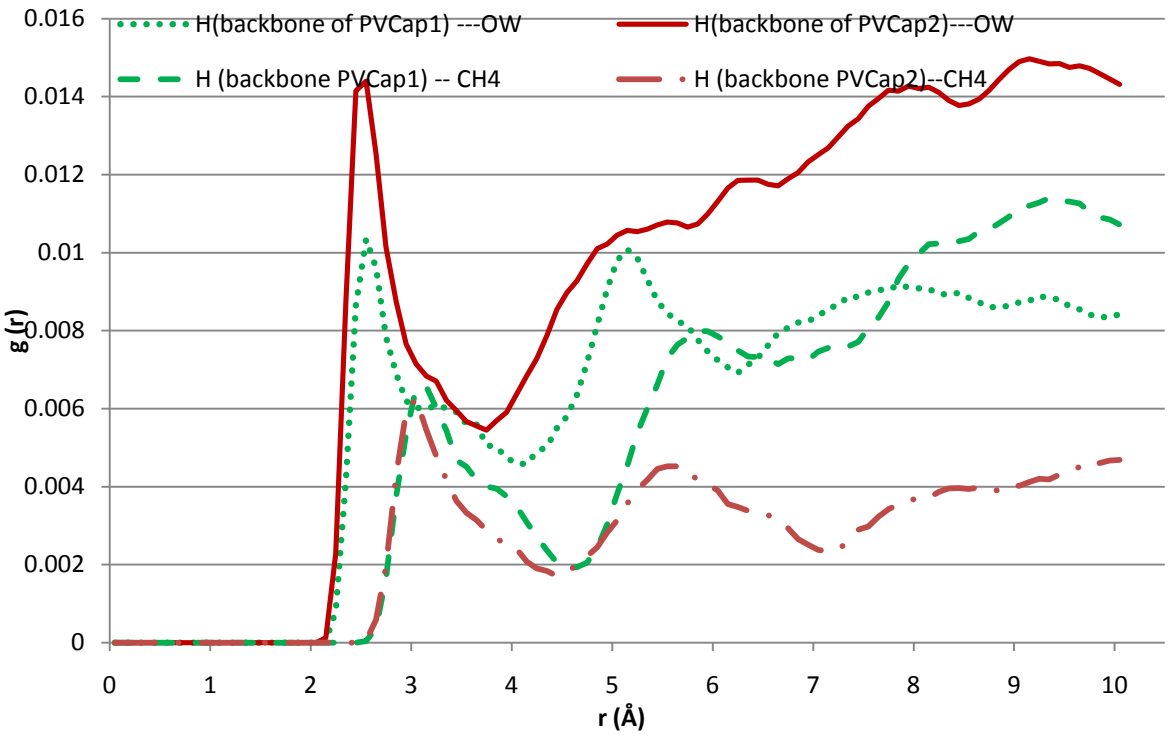

Figure 9-27: RDF for hydrogen (PVCap backbone) with methane and water oxygen in PSII-L system.

If we compare RDFs for PVCap1 lying at the interface in this system with the RDFs for PSI-L, where both PVCap molecules are at interface, it becomes clear that both methane molecules and water oxygens are more structured around the backbone in this system than in PSI-L.

Figure 9-28 presents the comparison of the RDFs for carbonyl oxygen and water oxygen. Since the peaks of O (PVCap)—OW are much lower than those of OW—OW in liquid water, a secondary axis was used. The behavior of water oxygen near the carbonyl oxygen was quite similar to that in PSI-L with some small differences. In PSI-L, both PVCap molecules demonstrated similar behavior but in PSII-L, the PVCap2 peaks beyond the second one were shifted further outward than in PVCap1. In addition, the peaks were flatter in PVCap2 beyond the second peak than in PVCap1. The integral values did indicate more water molecules around PVCap2 than PVCap1 due to the obvious fact that PVCap2 was immersed in water.

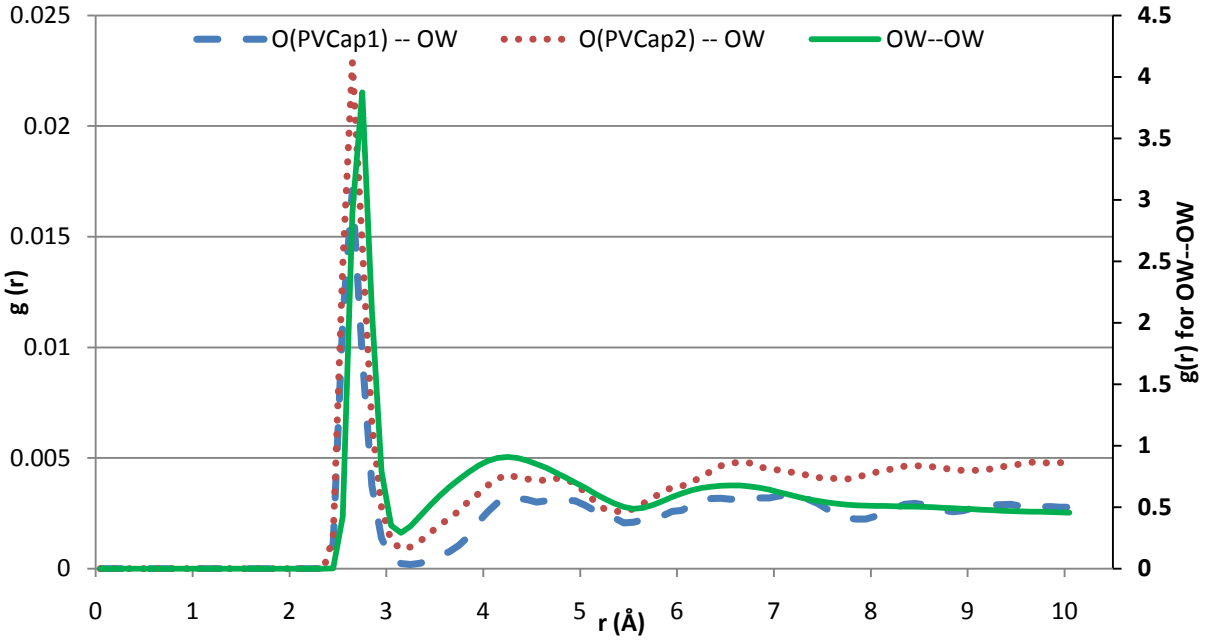

Figure 9-28: RDF for carbonyl oxygen (PVCap)—water oxygen and within water oxygens.

Calculation of the number of hydrogen bonds between the carbonyl oxygen of PVCap and the liquid water has shown that PVCap1 and PVCap2 formed 1.036 and 1.361 hydrogen bonds per oxygen atom on average, respectively. Liquid water in this system formed 1.361 numbers of hydrogen bonds per water oxygen as compared to 1.39 formed by water oxygen's in PSI-L and 1.42 formed by water oxygen's in RSII. Thus, PVCap2 formed similar number of hydrogen bonds as liquid water thereby reducing the possibility of hydrogen bonding within water molecules. Visual observations of trajectories done by means of VMD indicate that the number of hydrogen bonds formed by PVCap oxygen can vary from three to zero.

Figure 9-29 illustrates the hydrogen bond formation (indicated by the dotted orange line) between water hydrogen and PVCap oxygen.

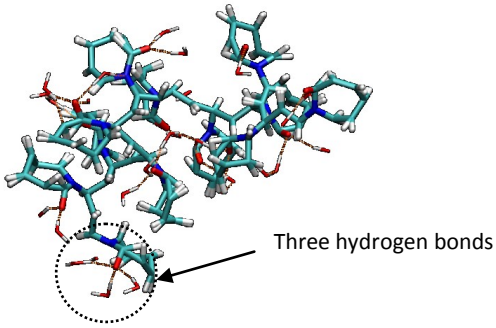

Figure 9-29: Hydrogen bonding in PVCap2 (PVCap represented as cyan, blue, white and red color molecule; water represented as red and white sticks, hydrogen bonds in orange dotted lines.

To study the surfactant effect of PVCap, equation (8-2) was used to calculate the interfacial tensions for the last 2000 intermediate averages. Each intermediate describes a 1000 MD steps. These results are plotted in Figure 9-30.

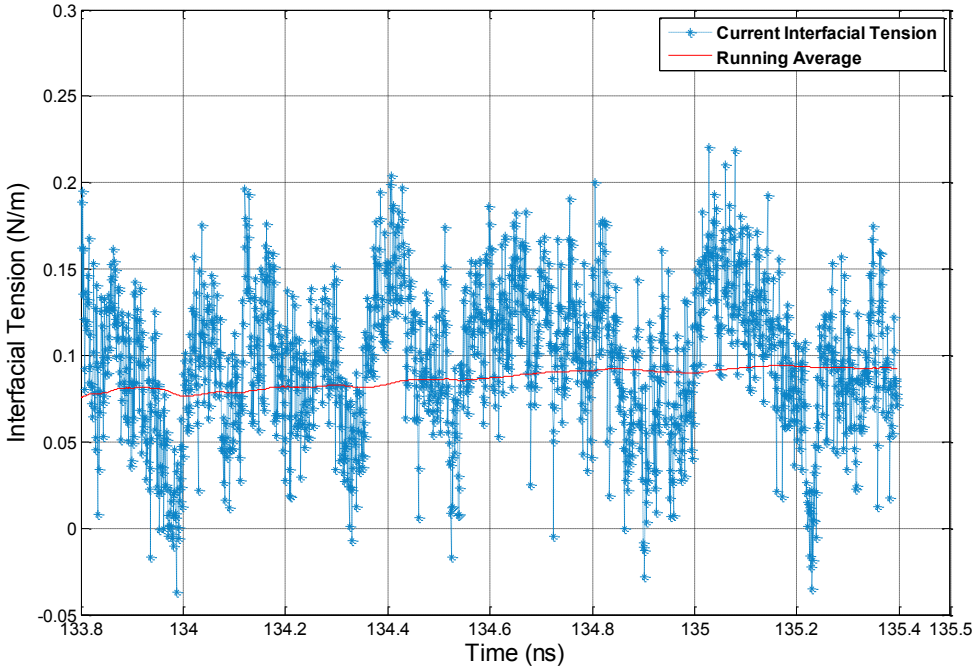

Figure 9-30: Interfacial tension in PSII-L system.

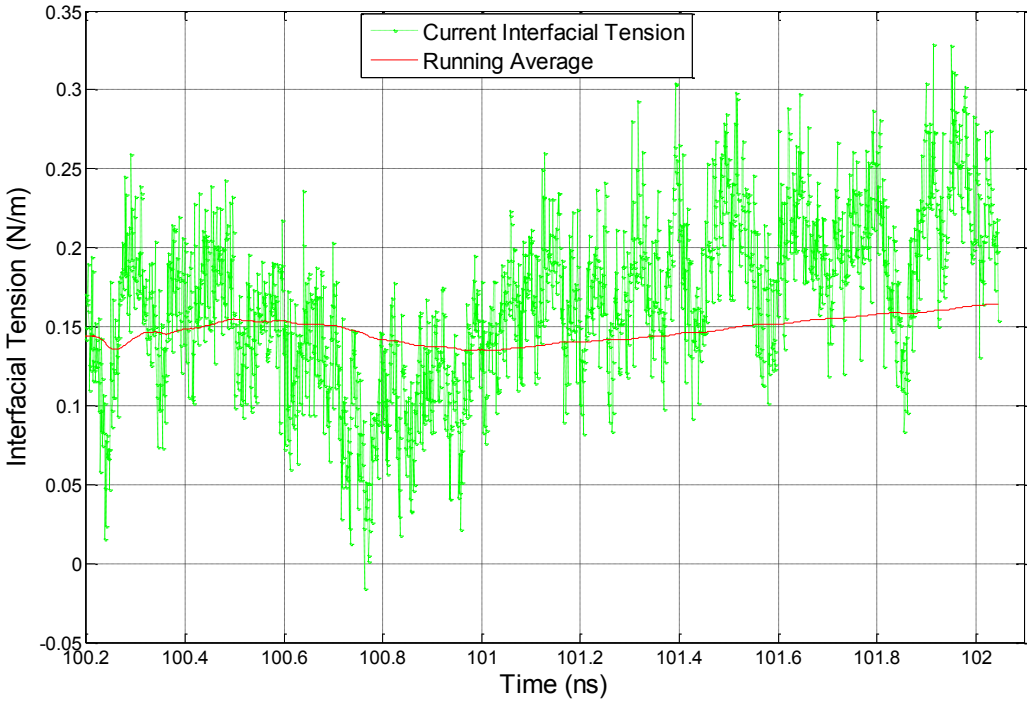

Figure 9-31: Interfacial Tension in RSII system.

The average value of interfacial tension at the end of simulation was 0.0926 $\pm$ 0.00267 N/m, identical calculations in RSII without PVCap molecules demonstrated the increasing trend of interfacial tension as illustrated in Figure 9-31. The average value at the end of 102 nanoseconds was 0.1645 $\pm$ 0.0022 N/m. This comparison indicates the decrease in the interfacial tension in the presence of PVCap. The fluctuation in interfacial tension was due to the usual wild fluctuations in system pressure. As stated earlier in section 9.2, pressure calculated by md43code for flexible molecules tend to overestimate the interfacial tension.

We will now discuss the results obtained for the PSII-C system (system with CM4 charges). This system was simulated for 26.38 nanoseconds. After 21.13 nanoseconds, Nosé –Hoover thermostat was switched on for temperature control. The final position of PVCap molecules is shown in Figure 9-32.

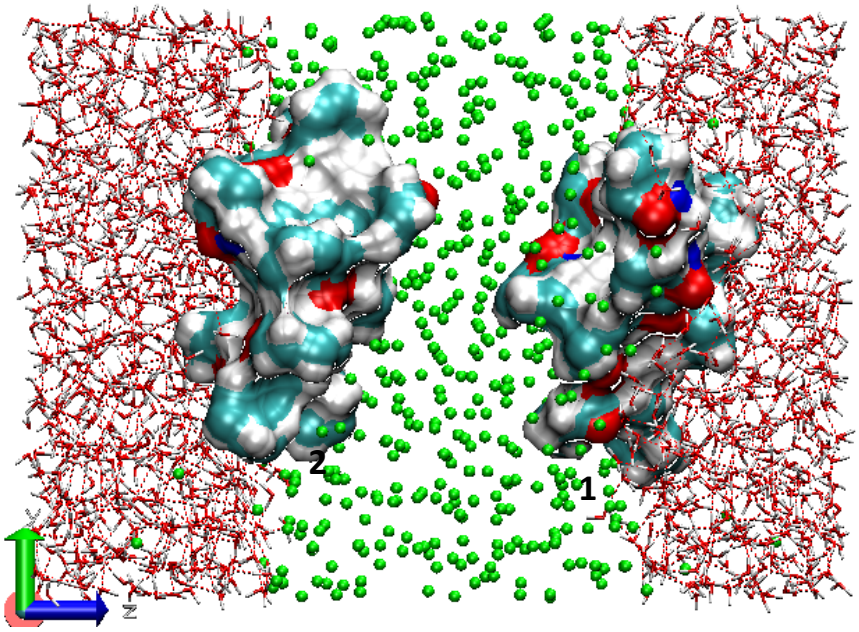

Figure 9-32: PVCap system II with CM4 charges after 26.38 ns

The behavior demonstrated by PVCap molecules in the PSII-C was clearly different compared to the PSII-L. In PSII-C, both PVCap molecules preferred to position themselves at interface with a major portion of a molecule lying in the methane phase. To probe the differences between the two systems, let us first have a closer look at the orientation of the two PVCap molecules in the two systems. Figure 9-33 illustrates the position and the orientation of the PVCap molecules. The PVCap backbone in PSII-C is indicated in mauve color, while in PSII-L is orange. Let us start with PVCap1.Its backbone lies more inside the

methane phase in PSII-C than in PSII-L. The rings attached to the ends preferred to lie flat at the interface with the most of the other rings oriented towards methane. In contrast to this, the most of the backbone was immersed in water with few rings facing towards methane in PSII-L.

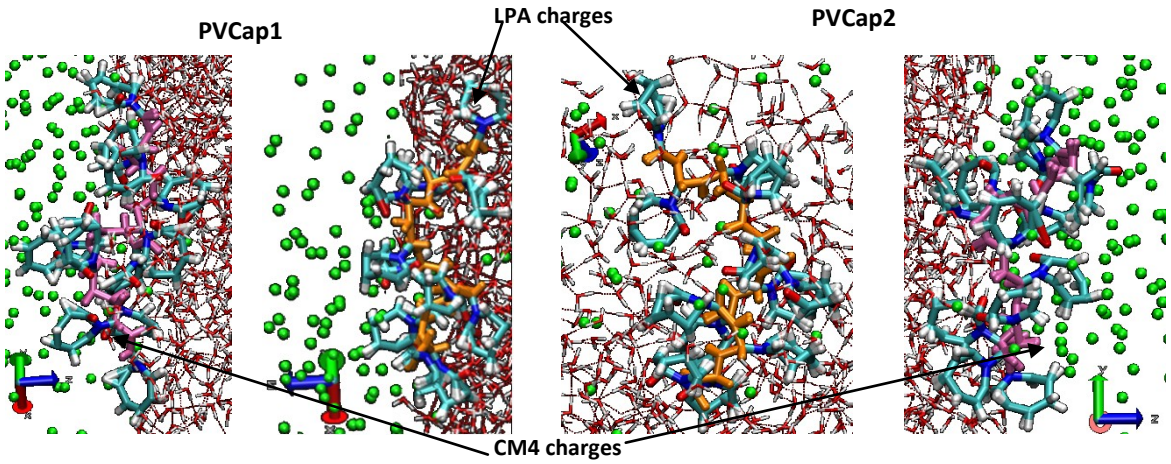

Figure 9-33: Orientation of PVCap molecules corresponding to charges (PSII)

Both the position and the orientation of the PVCap2 molecule in PSII-C were completely opposite to those in PSII-L. In PSII-L, PVCap2 preferred to remain close to PVCap1 and was completely immersed in the water phase. In contrast to this, PVCap2 in PSII-C was lying at the interface with most of its atoms interacting with the bulk methane phase. In both cases, oxygen atoms tended to point towards liquid water, increasing the possibility of hydrogen bonding with water. Since both PVCap molecules preferred the interface in PSII-C, the diffusion of methane molecules into water was hindered. In RSII system, there were 8 methane molecules dissolved inside liquid water after 26 nanoseconds as compared to 4 in PSII-C and more than 40 in PSII-L. It was concluded that in presence of high concentration of methane, the LPA charges appear to promote the formation of hydrate, whereas the CM4 charges would inhibit the hydrate formation process.

To get more concrete results, PSII-C needs to be run for a longer period of time. The total energy of the system did not show major fluctuations but the system pressure fluctuated drastically. The interfacial tension by the end of simulation run was 0.21188 ± 0.00195 N/m which may be unrealistic due to the pressure fluctuations. This is much higher than that in PSII-L and RSII system since the system is not yet fully equilibrated. The decrease in interfacial tension should be expected in PSII-C after a sufficiently longer simulation run. The

average intermolecular energy contributions obtained from PSII-L and PSII-C is presented in Table 9-C.

The strong interaction between the PVCap molecules in PSII-L could be clearly explained by the electrostatic energy between the PVCap molecules. Both the short-range and the long-range interactions indicated that the attraction between the PVCap molecules was so strong that it caused the methane molecules trapped between them to be dragged into water as well. The highly negative intermolecular energy value between PVCap and water molecules suggests a very strong interaction between them in case of PSII-L system. Short-range interactions are stronger between PVCap and other molecules (water and methane) in PSII-C than in PSII-L system thereby weakening water – water and water – methane interactions. When compared to RSII (Table 9-A), PSII-L showed a stronger interaction between water and methane whereas PSII-C showed comparatively weaker interaction between the guest and the host molecule.

Table 9-C: Intermolecular Energies (PSII)

	Short Range interaction energies (kJ/mol of the total system)		**Electrostatic intermolecular energies (kJ/mol of the total system)**	
	LPA Charges(PSII-L)	**CM4 Charges(PSII-C)**	**LPA Charges(PSII-L)**	**CM4 Charges(PSII-C)**
PVCap—H_2O	-252.8666±0.1619	-262.3217 ± 0.1363	-2306.085±10.981	-701.125 ± 5.685
PVCap—CH_4	-230.4933±0.0746	-389.2516 ± 0.1647	0.0	0.0
PVCap--PVCap	-0.8956 ±0.0016	-0.0005 ± 0.0	-82.9491±0.3961	0.1510 ± 0.0119
H_2O—H_2O	13.2877±0.0026	12.9546 ± 0.0021	-76.8505±0.0642	-74.7852 ± 0.0978
H_2O—CH_4	-3.6811+0.0010	-1.7671 ± 0.0005	0.0	0.0

It was thus concluded that the distribution of the partial atomic charges on its atom plays a major role in its orientation and interactions with other molecules. Similar behavior was not evident to this extent in the PSI-L system. This may be due to the initial positions of the PVCap molecules in the system. In PSII-L, at the start of the simulation run, both the PVCap molecule were positioned in such a way that they exhibited a very strong attraction towards each other, leading to the drift of PVCap molecules towards each other as illustrated in Figure 9-24. The other difference between the PSI-L and PSII-L system was that of methane concentration. Study of the values listed in Table 9-B as compared to that in Table 9-C

indicates that the electrostatic energies obtained from CM4 charges are consistent in the case of PSI and PSII systems with differences due to change in methane concentration. However, the electrostatic energy contributions obtained from LPA charges do not show any consistency in the two systems (PSI & PSII).

9.4 PVCap system III

This system was of particular interest, when it comes to analyzing the effect of PVCap concentration on its inhibition efficiency. Henceforth, system with CM4 charges and LPA charges will be referred to as PSIII-C and PSIII-L respectively. Let us discuss the PSIII-L system first. The simulation run for this system spanned the total of 111.17 nanoseconds. After simulating for 69.35 nanoseconds, Nosé-Hoover Thermostat was switched on to control the temperature of the system. It was observed that the initially dispersed methane formed a separate bubble inside the box only after 27 nanoseconds of simulation time. The nine PVCap molecules were distributed around the entire simulation box forming a continuous phase. None of the PVCap molecules were immersed inside the methane bubble as before, but rather preferred to lie close to the interface formed between the methane bubble and water.

Figure 9-34 below shows the final positions after 111.17 nanoseconds. This figure illustrates that a chain like pattern formed by all PVCap molecules that encloses the methane bubble. The nine PVCap molecules are represented in nine different colors. To get a clearer understanding of the PVCap arrangement, we present four different visualization of the nine replicas of the system (PBC applied to get a 3x3 cell). Both part ‘a’ and part ‘b’ are projections of the system in the x-y plane. Part ‘a’ shows only the backbones of PVCap molecules, along with water and methane phase while part ‘b’ excludes water but presents entire PVCap dodecamer and all the methane molecules to highlight the clear formation of methane bubble (indicated in circle). Part ‘c’ and part‘d’ are projections in the x-z plane. Representations in part ‘c’ and part‘d’ are similar to part ‘a’ and part ‘b’, respectively. Snapshots ‘c’ and‘d’ indicate the interface formation by the PVCap molecules, with the methane bubble forming close to this interface. It is evident from the snapshots that at high concentration PVCap molecules have formed a continuous pattern without flocculating, leading to the formation of separate PVCap interface between water and methane. The separation of water and methane phases was achieved due to reduction in the interfacial tension between them. Distinct separation of the phases could be expected for longer

simulation runs. Since the system was quite dense, the complete phase separation was retarded.

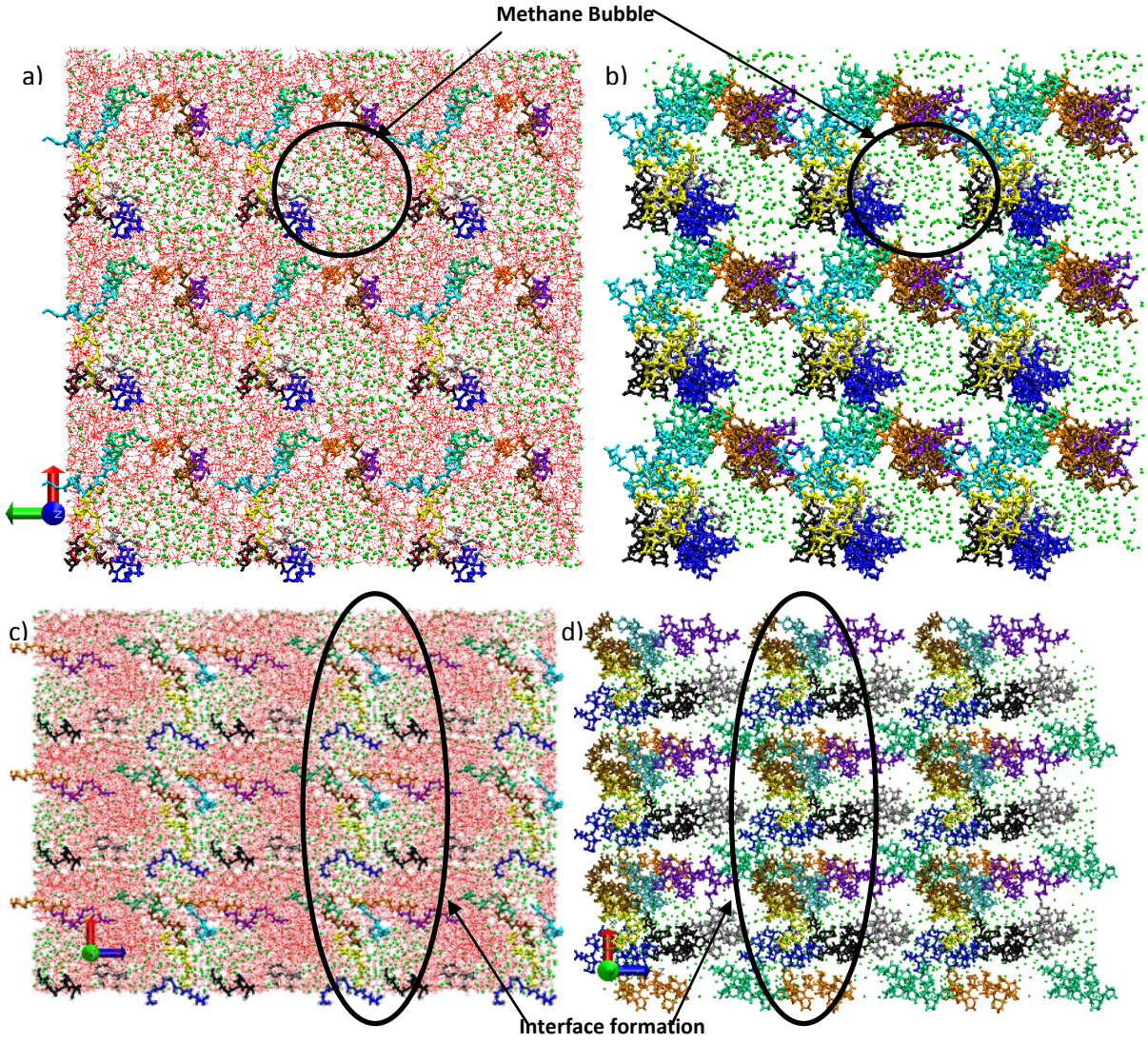

Figure 9-34: 9 replicas of the PSIII-L system (3x3). Color code: PVCap1 in Blue, PVCap2 in orange, PVCap3 in yellow, PVCap4 in Black, PVCap5 in cyan, PVCap6 in violet, PVCap7 in ochre, PVCap8 in Grey, PVCap9 in green.

The O (PVCap)—HW RDFs of all the nine PVCap molecules were quite similar to each other and also showed resemblance to the liquid water OW—HW RDFs. Several RDFs are presented in Figure 9-35. The first peak in the 9-PVCap system had been shifted slightly inwards, with the second peaks at about the same location as OW—HW, indicating that PVCap oxygen behaves similarly to water oxygen. All the RDFs reached the value close to 1.0 beyond 8.0 Å indicating that the system was quite isotropic.

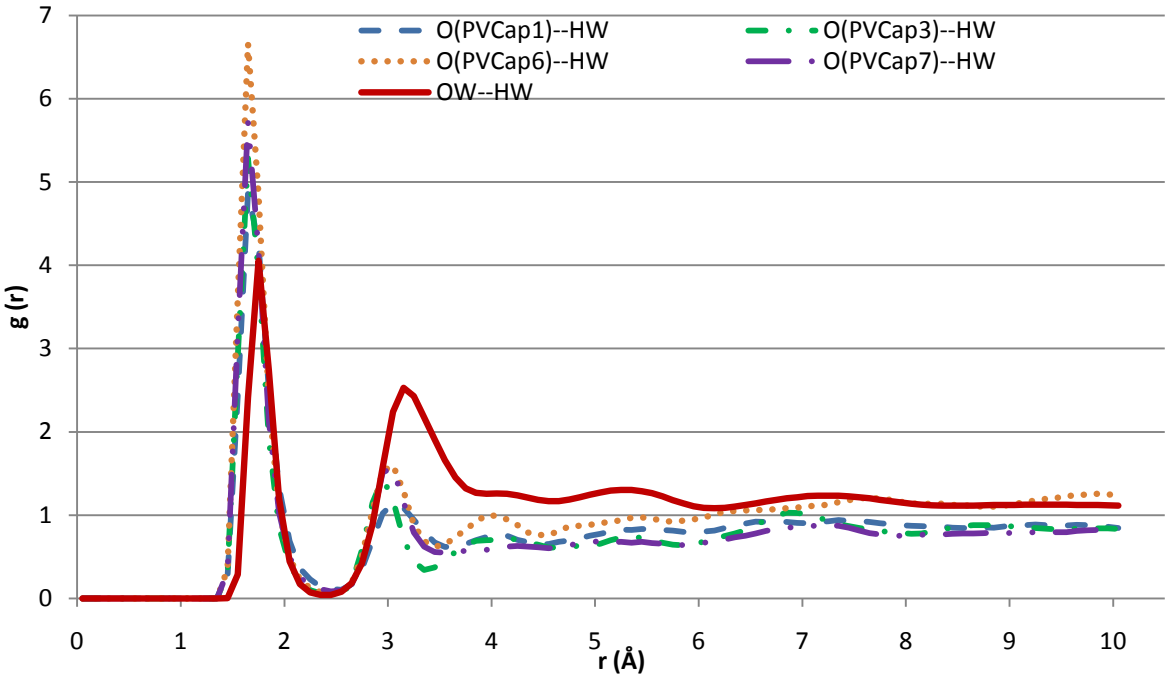

Figure 9-35: RDFs for carbonyl oxygen (PVCap)—water hydrogen compared with water oxygen—water hydrogen.

PVCap backbones showed a much more pronounced preference towards water oxygen than towards methane. The orientation of each PVCap was unique as can be seen from Figure 9-36 that presents the pair correlation between the H (Backbone of PVCap)—OW. The only similarity is that the PVCap ended with the coinciding of the first peak. It was observed that rings shielded the backbones of PVCap molecules and hence the interaction between the backbone and the methane molecules was hindered.

The presence of PVCap will restructure the liquid water by forming hydrogen bonds with it. The hydrogen bonds estimates indicated that PVCaps were engaged in more hydrogen bonding per oxygen than liquid water. On average, PVCap formed 1.307 hydrogen bonds per O (PVCap) atom in comparison to 1.26 hydrogen bonds for liquid water. This is much fewer than the number of hydrogen bonds formed by liquid water in PSI-L (1.39), PSII-L (1.36) and pure liquid water (1.42). This result is obvious since there are nine number of PVCap molecules in this system as compared to two in PSI-L and PSII-L. This indicates that the water ordering will be highly influenced with the greater amount of PVCap molecules.

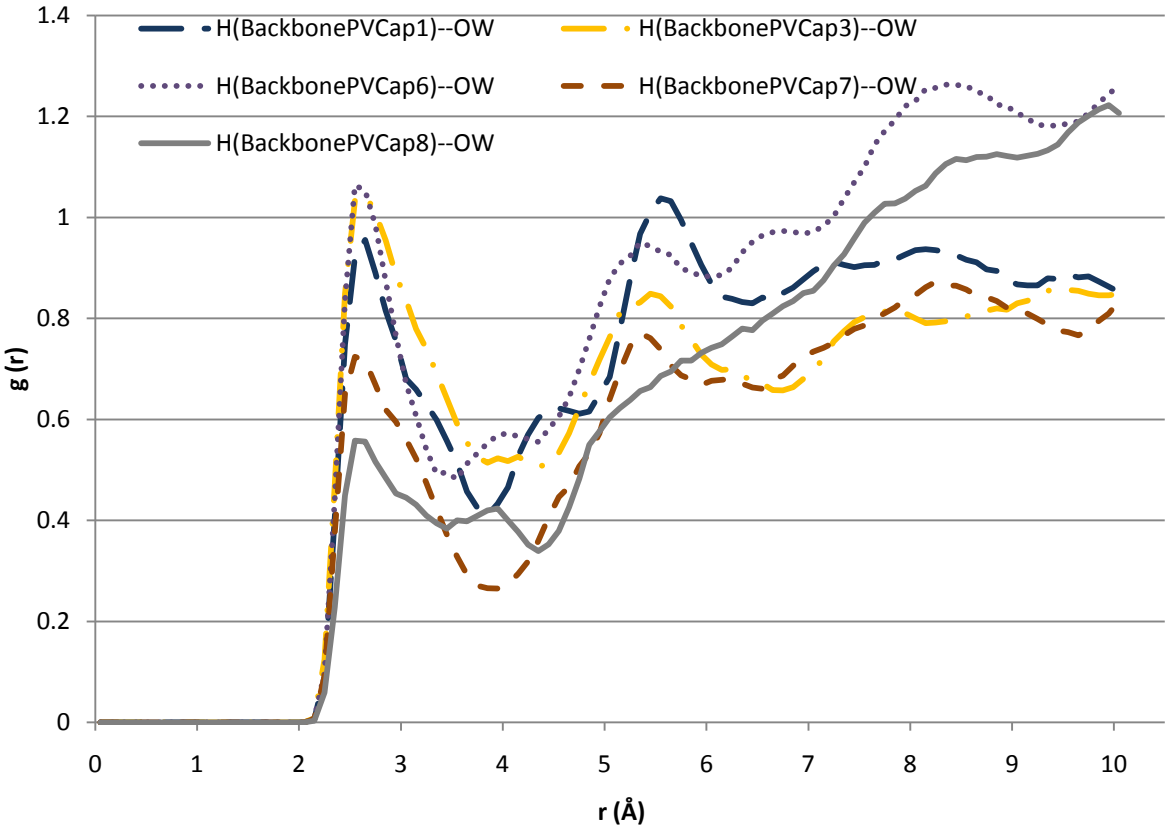

Figure 9-36: RDFs for hydrogen (PVCap Backbone)—water oxygen.

We will now address the different behavior of the PSIII-C system. This system was simulated for 23.05 nanoseconds with Nosé-Hoover thermostat on after 17.18 nanoseconds. The final state of this system is demonstrated in Figure 9-37 with PBC applied. Snapshots 'a' and 'b' are on y-z plane whereas snapshot 'c' and'd' are in x-z plane. The same conventions are used as in Figure 9-34. As seen from the snapshots, PVCap molecules formed a chain-like pattern similar to that in PSIII-L system. The majority of methane molecules formed a bubble close to the interface created by PVCap. To understand better how the orientation of the PVCap molecules is affected by the choice of charge distribution, RDF analysis was made. Since the extension of the PVCap molecules in both the systems (PSIII-L and PSIII-C) varied from 16 Å to 20 Å, RDF analysis was made with maximum distance cut off set to 20Å. At first, the pair correlation function for only the nitrogen atom of the first ring in each of the nine PVCap molecules was estimated.

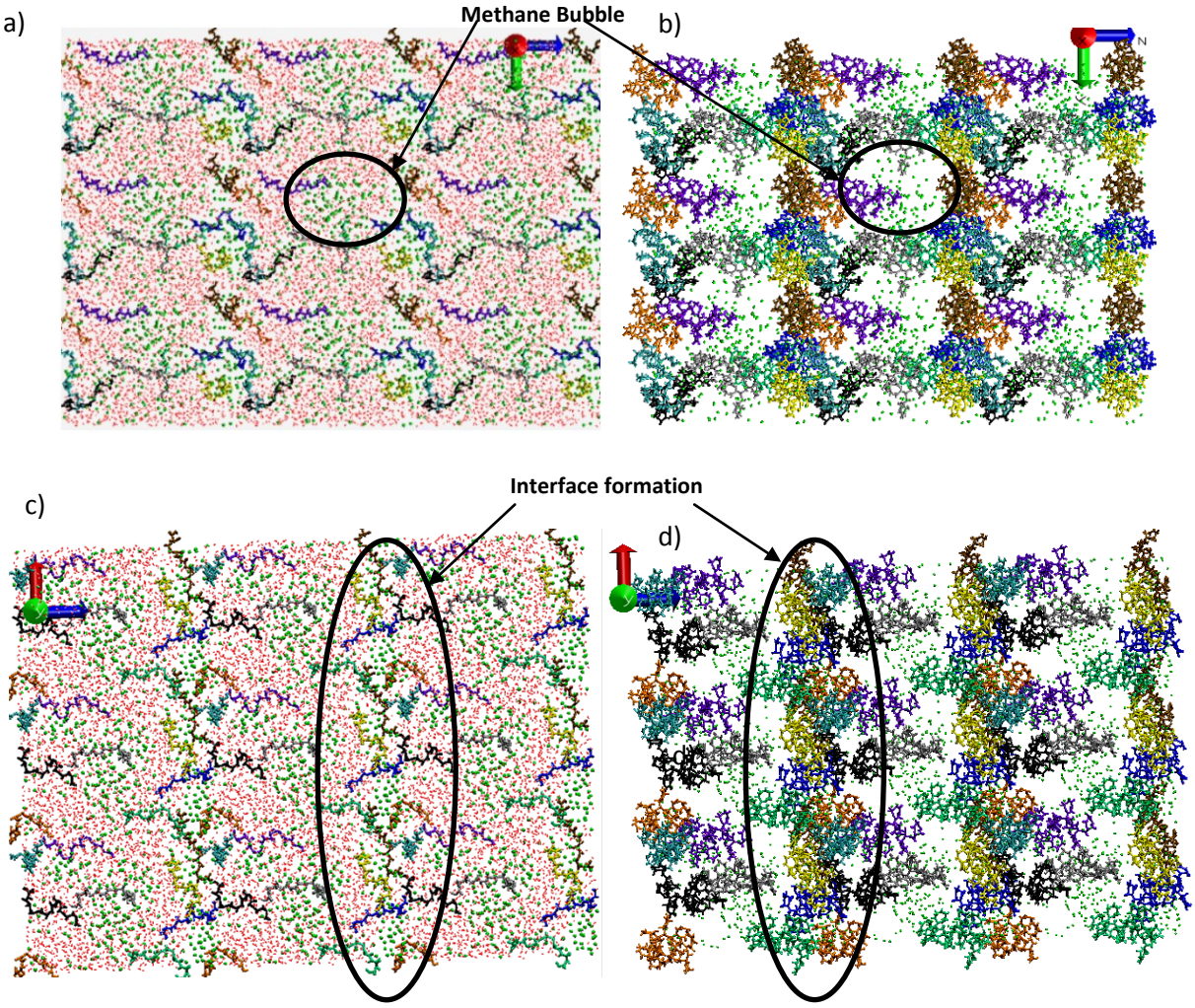

Figure 9-37: 9 replicas of the PSIII-C system after 23.05 ns. Color code: PVCap1 in Blue, PVCap2 in orange, PVCap3 in yellow, PVCap4 in Black, PVCap5 in cyan, PVCap6 in violet, PVCap7 in ochre, PVCap8 in Grey, PVCap9 in green.

Figure 9-38 presents the N-N RDFs for nitrogen in the edge ring for both systems. These RDFs will indicate the relative ordering of the edge in the PVCap molecules. The first peak in PSIII-L is at 13.05 Å showing the most probable distance between the first rings of any two PVCap molecules. A number of sharp peaks indicating no uniform position of the PVCap molecules follow this peak. In PSIII-C system, the first peak is further shifted outward to 14.65 Å and is followed by a second sharp peak at 17.35 Å. Note that the second peak is higher than the first. The integral values at the first peak are close to 1 whereas the integral value at second peak are close to 2, indicating the most likely distance between the first ring of the two and three PVCap molecules respectively. The distribution of PVCap molecules appeared to be more structured in PSIII-C system than in PSIII-L system.

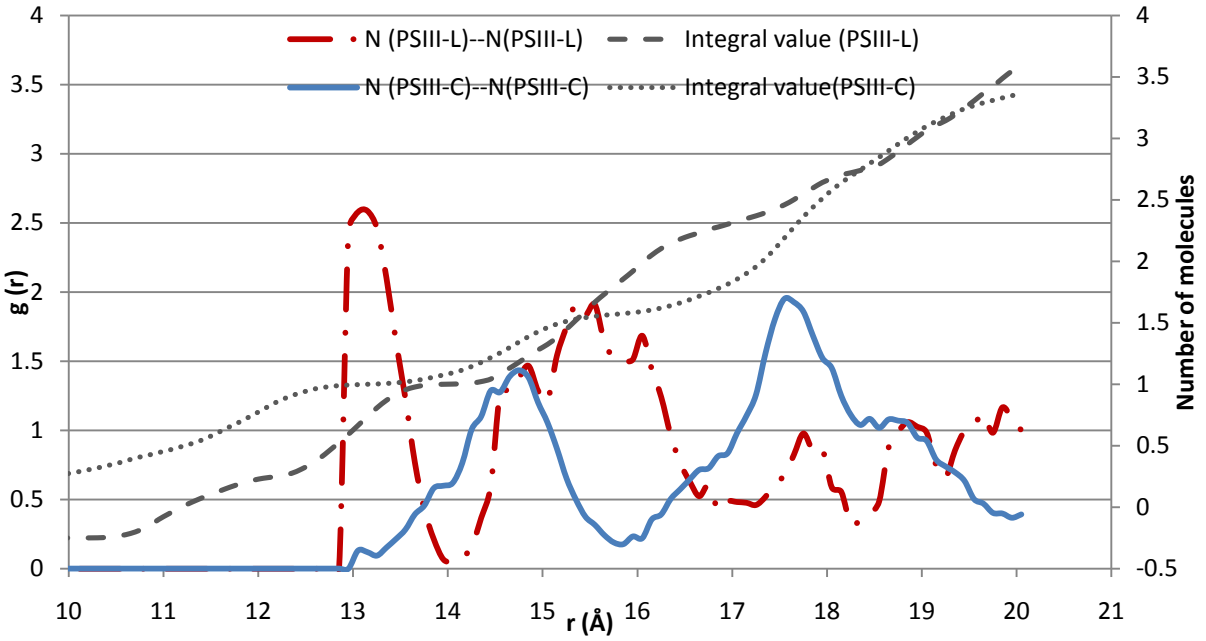

Figure 9-38: RDF between nitrogen—nitrogen for both the systems.

Figure 9-39 illustrates the pair correlation between the last carbon atoms in the backbone of all PVCap molecules.

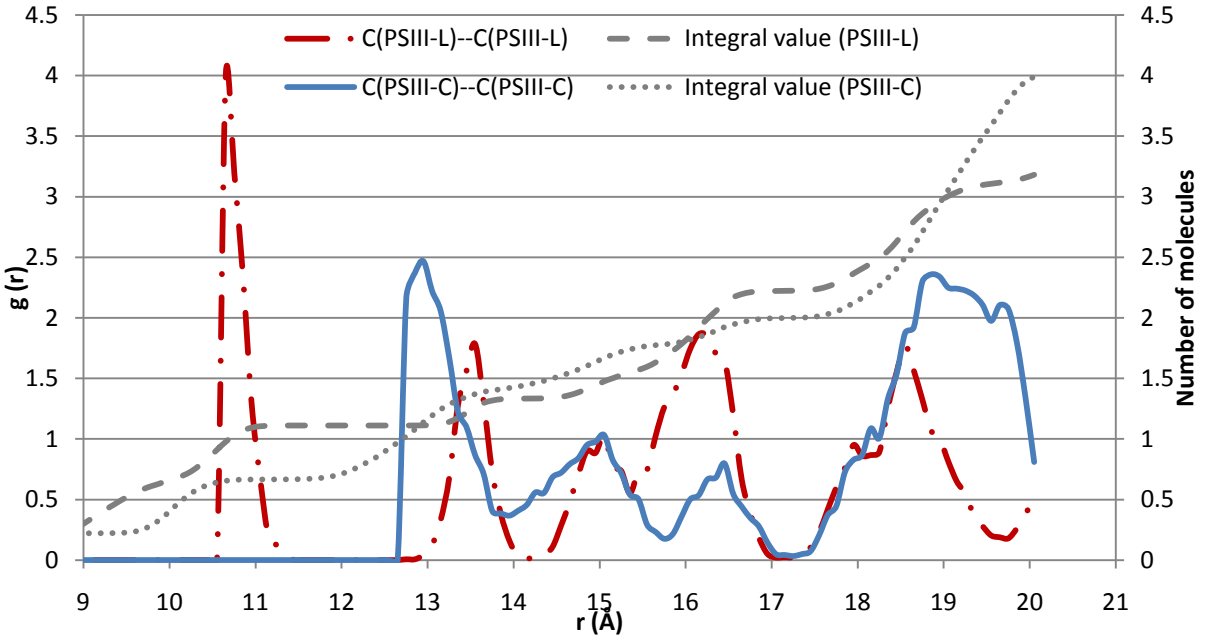

Figure 9-39: RDF between carbon (backbone)—carbon (backbone) for both the systems.

For PSIII-L system, the first sharp peak is at 10.55 Å and is followed by the second, the fourth and the sixth peak with roughly the same height, and the third and the fifth shoulder-like peaks of similar height. This indicates the ordered positions of the PVCap backbones. In the PSIII-C system, the first peak is shifted by 2.3 Å outwards to 12.85Å and is followed by

the second and the third sharp peaks. It is interesting to see that the fourth distinct peak is of almost the same height as the first peak, indicating the two most probable distances between the two backbone carbon atoms of the different PVCap molecules. It becomes evident from the RDFs that the attractive interaction between the PVCap molecules is stronger in PSIII-L system than in PSIII-C thereby decreasing the distance between the two PVCap molecules in PSIII-L system. The PSIII-C system needed to be run for a longer period to allow the time for the system to achieve a more complete separation if it is so inclined.

The final intermolecular energy contributions from the two systems are listed in Table 9-D. Results obtained from the RDFs analysis are confirmed by the values corresponding to the electrostatic interaction between the PVCap molecules that indicate a stronger electrostatic attraction between PVCap molecules in PSIII-L system then in PSIII-C. As observed earlier, a much stronger electrostatic attraction is also present between PVCap and water molecules in PSIII-L system, thus weakening the water-water interactions. The short-range interactions between water and methane are relatively more favorable in the PSIII-C system. This is due to a better phase separation of methane molecules in form of bubbles has occurred in PSIII-L system than in PSIII-C system. It was also instructive to observe that the short-range interactions between PVCap and other molecules (water and methane) are more negative for the CM4 charges than for the LPA ones. A much better separation of phases should be expected in PSIII-C system if this system was run for same time as PSIII-L system.

Table 9-D: Intermolecular Interactions (PSIII)

	Short Range interaction energies (kJ/mol of the total system)		**Electrostatic intermolecular energies (kJ/mol of the total system)**	
	LPA Charges (PSIII-L)	**CM4 Charges (PSIII-C)**	**LPA Charges (PSIII-L)**	**CM4 Charges (PSIII-C)**
PVCap—H_2O	-223.3061±0.128	-321.6909 ± 0.059	-2338.079±3.421	-658.1749 ± 2.246
PVCap—CH_4	-105.5409±0.035	-158.7547 ±0.034	0.0	0.0
PVCap--PVCap	-95.1812±0.0242	-107.1956 ± 0.0251	-80.1329±0.8933	-37.4060 ± 0.5170
H_2O—H_2O	12.0431±0.0019	12.4461 ± 0.0015	-59.4294±0.0628	-67.4674 ± 0.0664
H_2O—CH_4	-5.3223+0.0017	-6.5584 ± 0.0011	0.0	0.0

9.5 System IV

This system was set up with the aim of obtaining a composite system with stable hydrate phase. Once the stable hydrate phase is achieved, the PVCap molecules would have been inserted, and its effect and preferences could be studied in this composite system containing two distinct interfaces, namely hydrate-liquid water and liquid water-methane. Since the exact stable hydrate temperature for a model water-hydrate system is unknown, this system was replicated to run at two different temperatures, 240K and 200K. Let us denote the systems ran at 240K and 200K as 'SIV-A' and 'SIVB' respectively. The time step used in all the runs was 1 x 10^{-15} seconds. Soon after a short run of 2.89 nanoseconds, the hydrate in the SIV-A system began to melt as indicated in Figure 9-40 (dotted circle). Since the hydrate phase was not stable at 240K, the temperature of the system was reduced to 220K. This system was then run until 18.69 nanoseconds and neither reformation nor further melting of hydrate was observed.

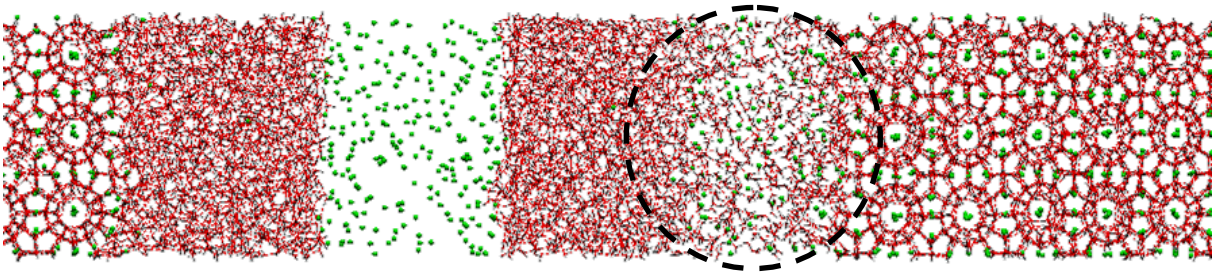

Figure 9-40: SIV-A system after 2.89 ns

The methane molecules released from melted hydrate preferred to clump together forming the methane bubble demonstrated in Figure 9-41.

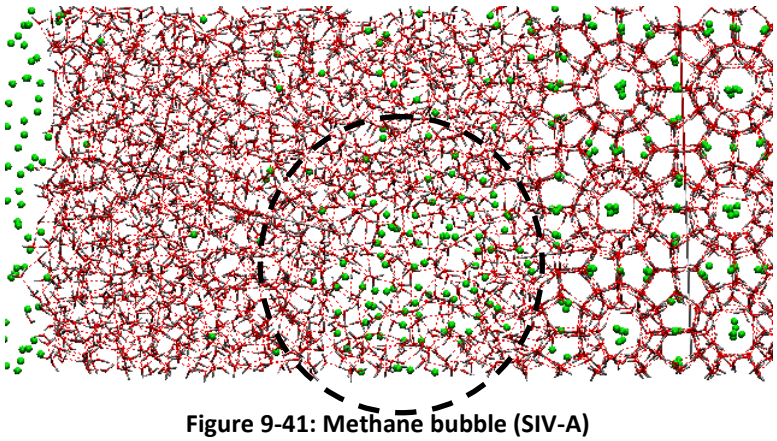

Figure 9-41: Methane bubble (SIV-A)

Hydrate in SIV-B also showed the tendency to melt but since the temperature was 40K lower than in SIV-A, the melting of hydrate began at 5.7 nanoseconds. Taking a notice of this, the

temperature of the system was reduced to 190K and the system was simulated for 13 nanoseconds more. A formation of methane bubbles from the melted hydrate was observed similarly to SIV-A. Figure 9-42 shows the state of the SIV-B system at 5.7 nanoseconds (part a) and the formation of methane bubbles at the end of simulation (part b). The behavior of the SIV-A and SIV-B, appears to suggest no tendency for reformation of unstable hydrate. These systems could not be considered viable for the study of PVCap impact, since the results obtained could be misleading and no assured conclusion could be drawn.

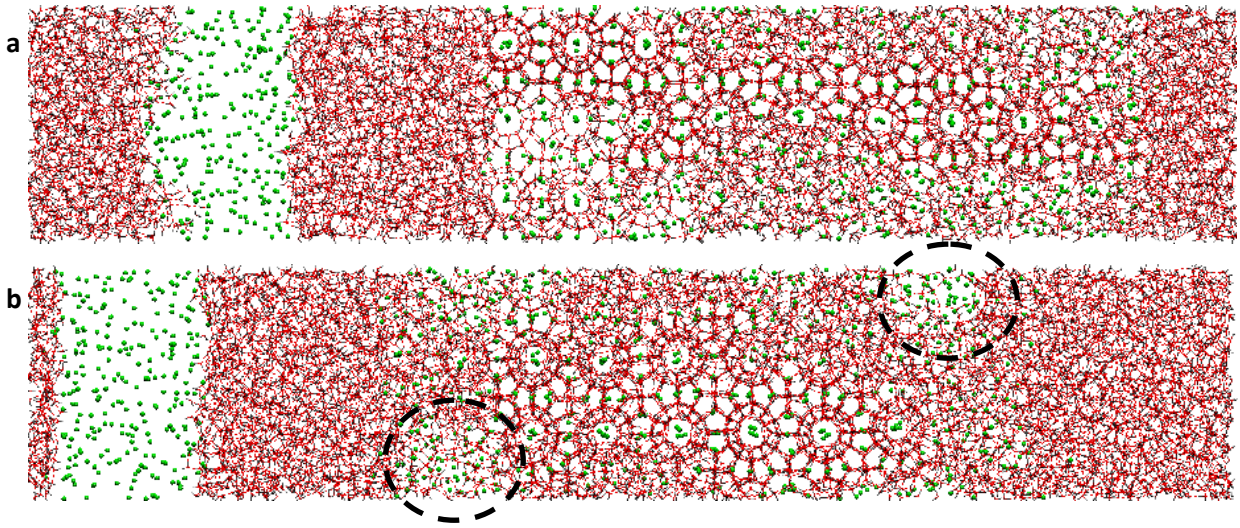

Figure 9-42: a) Melted hydrate at 5.7 ns (SIV-B); b) After 18.73 ns.

To obtain a stable hydrate phase system, a backup file saved in system SIV-B before the hydrate started to melt (after 5.4 nanoseconds) was restored, and a new simulation set with temperature reduced still further from 200K to 190K. This system will be referred to as 'SIV-C'. No sign of hydrate melting was exhibited in SIV-C even beyond 20 nanoseconds of simulation time. After 21.7 nanoseconds, simple velocity scaling was switched off and Nosé-Hoover Thermostat applied to control the temperature. To check the stability of the system and find the melting point for hydrate, it was decided to gradually increase the temperature of the system by 1K at a time after 25.1 nanoseconds elapsed. Temperature incremented by 1K every 10000 time steps until the system reached the temperature of 200 K after 26.1 nanoseconds. This system was simulated further at 200 K until 28.68 nanoseconds, and the hydrate was found to be intact. Figure 9-43 illustrates the final condition of the system before the simulation was stopped.

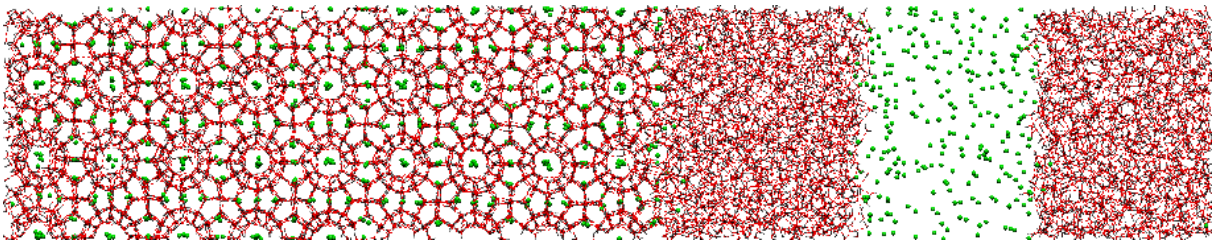

Figure 9-43: SIV-C after 28.68 ns of run.

Because of the time constraint and uncertainty in regards to hydrate melting, no quantitative analysis was applied to these systems. Given the fact that hydrate demonstrated the tendency to dissociate except for SIV-C, the main work of studying the behavior of PVCap molecule in the system consisting of all three phases, hydrate, liquid water and methane phase were not accomplished. A further work needs to done. To save the time this stable system should be taken as a start point and must be developed further to analyze the effect of KHI.

10 Conclusion

We have successfully applied molecular dynamic simulations to study the impact of PVCap dodecamer on water structure and hydrate nucleation process. We have analyzed to which extent PVCap's effectiveness as a kinetic hydrate inhibitor is affected by varying hydrocarbon concentrations, distribution of partial atomic charges and its own concentration in water. Three main simulation setups were used to study these effects.

The pure water-methane reference systems RSI and RSII exhibited the signs of pre-nucleation by diffusion of methane molecules into water. It was observed that dissolution of methane in water increased with the higher concentrations of methane in RSII. Water was found to form cavity-like structures around the diffused methane molecules. The cavity formation and congregation were more evident in RSII than in RSI. By the end of the simulations, 8 and 13 methane molecules dissolved in water in RSI and RSII systems, respectively. It can therefore be concluded that the driving force for hydrate formation increased with the hydrocarbon phase density.

Two PVCap--water--methane systems with two different sets of charges on PVCap (PSI-L and PSI-C systems) were studied and compared with the reference system RSI. No evidence of nucleation was observed in these systems with the two PVCap molecules preferring to remain at the interface between methane and water. Since those, PVCap molecules positioned themselves at the most likely location for the hydrate nucleation, the onset of nucleation was be delayed. It was concluded that both the position and intermolecular interactions of the PVCap molecules were heavily influenced by the distribution of partial atomic charges. When the charge set generated via the LPA was used (PSI-L), the rings stuck out on both sides of interface and shielded the PVCap backbones. Whereas the PVCap rings tended to point towards water rather than methane in the case of CM4 charges (PSI-C), thereby increasing the possibility of hydrogen bonding with water. The interaction between the PVCap molecules was more repulsive with LPA charges than with CM4.

In the two simulations involving a high-density phase of methane, the behavior exhibited by the PVCap molecules was shown to be very much dependent on the partial atomic charges chosen. PSII-L system with the LPA charges promoted rapid diffusion of methane inside

water. On the contrary, PSIII-C system with the CM4 charges slowed down the process of diffusion in comparison with reference system, RSII. The electrostatic attraction between the two PVCap molecules in PSII-L system was very strong causing the methane molecules to be pushed inside the water phase. It was this strong affinity between PVCap, which governed their preferred positions, with one PVCap molecule at the water-methane interface and the other completely immersed inside bulk water very close to the first PVCap molecule. On the other hand, in PSII-C system, both the PVCap molecules preferred to remain at the interface between water and methane thereby reducing the rate of dissolution of methane molecules into water.

The effect of high PVCap concentration on the dispersed water-methane phase was studied in PSIII-C and PSIII-L systems. In these systems, it was concluded that PVCap molecules would form a continuous chain-like pattern across the entire system without flocculating at high concentrations. The interfacial tension between water and methane was reduced in the presence of high concentration of PVCap molecule. Therefore, methane will tend to form a separate bubble from a randomly dispersed methane phase. Confirming the findings from the other simulations, none of the PVCap molecules were immersed inside the methane bubble but preferred to lie near the interface between water and methane bubble. The study of RDFs indicated that the positioning of the PVCap molecules in PSIII-C system was more ordered than that in PSIII-L system. In addition, the short-range interaction between PVCap and other molecules were stronger in PSIII-C system than in PSIII-L. Due to this fact, the PSIII-C will show a clear tendency to achieve a better phase separation if allowed to run for sufficiently long time.

In order to pinpoint the model-specific temperature region for methane hydrate stability, system IV containing a hydrate slab along with water and methane phases, was simulated at two different temperatures. At both 240 K (SIV-A) and 200 K (SIV-B), hydrate demonstrated the tendency to melt. Within the limited simulations, in this work it was not possible to find a stability region for the hydrate, making it impossible to study the effect of PVCap inhibitor in systems containing liquid water-hydrate interface and liquid water-methane interface. The only system in which hydrate phase remained intact until the end was the SIV-C, which was run for a long time at 190K temperature and with temperature increased to 200K towards the

end. Since this system did not dissociate even after 28 nanoseconds, it could be utilized for further work.

In general, it can be concluded that in all the systems, PVCap did restructure liquid water by forming hydrogen bonds with water via the carbonyl oxygen. This will reduce the possibility of hydrogen bonding between water molecules and hinder water reordering needed to build hydrate cages from liquid water. It was found that the interfacial tension between water and methane phase was reduced in the presence of PVCap molecules. The distribution of the partial atomic charges within the atoms of PVCap molecule was shown to play a major role in their orientations and interactions with other molecules. Charges obtained using the CM4 proved to induce a more consistent behavior than those obtained by means of the LPA approach. The PVCap behavior was strongly affected by its concentration in water. At high concentration, the interaction between PVCap molecules was increased to a great extent and led to the formation of a continuous PVCap network in the simulation box. At low concentration, PVCap preferred to remain at the methane-water interface thereby inhibiting the process of nucleation.

11 Suggestions for further work

Improvement in the models:

PVCap model needs to be validated against all available experimental data to make sure it is useable for studying the PVCap kinetics. It might be advisable to sacrifice the force field transferability in favor of obtaining separate charge sets for PVCap-water interactions and PVCap-methane interactions. An extended literature survey on experimental results for PVCap using fundamental experimental techniques (NMR, X-Ray etc) is also recommended in a search for data, which can be used for model verifications.

As PVCap is a surfactant and these are liquid/gas systems, the difference between interface free energy and interfacial tension is very limited. Adjusting the models carefully so as to reproduce realistic pressures is therefore recommended. Search for experimental data on interfacial tensions in this type of systems is also recommended.

In this thesis, a one-site methane model was used. This model might be unable to provide true methane-water and methane-PVCap interactions. Hence, a 5-site methane model must be tested to see if it improves the results.

System setups:

The effect of high PVCap concentrations must be tested in a system having a distinct water-methane interface to find if PVCap molecules cover the interface or aggregate. PVCap effect in the stable hydrate system with two interfaces, hydrate-liquid water and liquid water-methane must be studied. System setups with a true bulk water phase should be considered.

Since the hydrate tended to melt, it is recommended to start the simulation with liquid water already saturated with methane. To achieve a stable hydrate phase and investigate the effect of PVCap – hydrate interactions, longer simulation runs in an NPT ensemble is also recommended.

Simulation protocols:

As opposed to md43, the newer MdynaMix version 5.1 can handle parallel runs with fully flexible molecules. In addition to this, pressures obtained in version 5.1 are claimed to be

better than md43 (private communication between its developer Alexander Lyubartsev and Prof. Tatiana Kuznetsova). Hence, in future simulations, it is recommended that this new version be used.

Capillary wave approach for sampling of interface free energy requires large interfaces for sampling significance/accuracy but it would be recommended since variations in pressures are likely to be high even though adjusted potentials may result in pressures that are more realistic.

Systems should be run at wide range of temperatures to calculate the change in chemical potential due to insertion of PVCap.

Experiments:

It is possible that at high pressures the solubility of methane in water is increased due to the influence of PVCap. Experiments must be performed to check the PVCap effect on the methane solubility in water at high pressures, with the surface adsorption effects being the focus.

References

Allen, M. P. and D. J. Tildesley (1989). Computer simulation of liquids. Oxford, Clarendon Press.

Allinger, N. L. and K. A. Durkin (2000). "Van der Waals effects between hydrogen and first-row atoms in molecular mechanics (MM3/MM4)." Journal of Computational Chemistry **21**(14): 1229-1242.

Allinger, N. L., Y. H. Yuh and J. H. Lii (1989). "Molecular Mechanics - the MM3 Force-Field for Hydrocarbons .1." Journal of the American Chemical Society **111**(23): 8551-8566.

Andersen, H. C. (1983). "Rattle: a velocity version of the shake algorithm for molecular dynamics calculations." Journal of Computational Physics **52**(1): 24.

Anderson, B. J., J. W. Tester, G. P. Borghi and B. L. Trout (2005). Properties of Inhibitors of Methane Hydrate Formation via Molecular Dynamics Simulations. **127:** 17852-17862.

Baird, C. and M. C. Cann (2004). Environmental chemistry. New York, Freeman.

Bauer, H. (1994). Scientific literacy and the myth of the scientific method, Univ of Illinois Pr.

Becke, A. (1993). "A new mixing of Hartree-Fock and local density-functional theories." The Journal of Chemical Physics **98**(2): 1372.

Berendsen, H. J. C. (1987). "The missing term in effective pair potentials." The Journal of physical chemistry **91**(24): 6269.

Carroll, J. J. (2003). Natural gas hydrates: a guide for engineers. Amsterdam, Gulf Professional Publ.

Carver, T. J. (1999). "Molecular dynamics calculations of N-methylpyrrolidone in liquid water." Physical chemistry chemical physics **1**(8): 1807.

Christiansen, R. L. and E. D. Sloan (1994). "Mechanisms and Kinetics of Hydrate Formation." International Conference on Natural Gas Hydrates **715**: 283-305.

Colle, S., C. Taillefumier, Y. Chapleur, R. Liebl and A. Schmidt (1999). "Synthesis and biological testings as inhibitors of HMGCoA reductase of the seco-acid of tuckolide and its C-7 epimer." Bioorganic & Medicinal Chemistry **7**(6): 1049-1057.

Dalmazzone, D., N. Hamed, C. Dalmazzone and L. Rousseau (2006). "Application of high pressure DSC to the kinetics of formation of methane hydrate inwater-in-oil emulsion." Journal of thermal analysis and calorimetry **85**(2): 361-368.

Dill, K. A., S. Bromberg and D. Stigter (2003). Molecular driving forces: statistical thermodynamics in chemistry and biology. New York, Garland Science.

Englezos, P. (1993). "Clathrate Hydrates." Industrial & Engineering Chemistry Research **32**(7): 1251-1274.

Førrisdahl, O. K. (2002). Computer simulations of natural gas hydrates : equilibrium, melting, inhibition and free energy calculations. [Bergen], Programme of Process Technology, Department of Physics, University of Bergen.

Gibbs, J. (1928). "The collected works of JW Gibbs, Vol. 1." Yale Univ. Pr., New Haven, Conn.

Hawtin, R. and P. Rodger (2006). "Polydispersity in oligomeric low dosage gas hydrate inhibitors." Journal of Materials Chemistry **16**(20): 1934-1942.

Hinchliffe, A. (2003). Molecular modelling for beginners. Chichester, Wiley.

Hinchliffe, A. (2008). Molecular modelling for beginners. Chichester, Wiley.

Hohenberg, P. (1964). "W. Kohn." Physical review. C, Nuclear physics **3**(136): 864.

Hoover, W. (1985). "Canonical dynamics: Equilibrium phase-space distributions." Physical Review A **31**(3): 1695-1697.

Humphrey, W., A. Dalke and K. Schulten (1996). "VMD: Visual molecular dynamics." Journal of Molecular Graphics **14**(1): 33-&.

Hünenberger, P. (2005). "Thermostat algorithms for molecular dynamics simulations." Adv. Polym. Sci **173**: 105-149.

Hutter, J. L., H. E. King and M. Y. Lin (2000). Polymeric Hydrate-Inhibitor Adsorption Measured by Neutron Scattering. **33:** 2670-2679.

Jeffrey and McMullan (1967). The Clathrate Hydrate.
Jeffrey, G. A. (1984). "Hydrate inclusion compounds." Journal of inclusion phenomena and molecular recognition in chemistry **1**(3): 211.
Jensen, F. (2007). Introduction to computational chemistry. Chichester, Wiley.
Jorgensen, W. L. (1984). "Optimized intermolecular potential functions for liquid hydrocarbons." Journal of the American Chemical Society **106**(22): 6638.
Kaminski, G. and W. Jorgensen (1998). "A quantum mechanical and molecular mechanical method based on CM1A charges: applications to solvent effects on organic equilibria and reactions." J. Phys. Chem. B **102**(10): 1787-1796.
Kashchiev, D. (2000). Nucleation: basic theory with applications. Oxford, Butterworth-Heinemann.
Kelland, M. A. (1994). Control of hydrate formation by surfactants and polymers
Proceedings of SPE Annual Technical Conference and Exhibition SPE.
Kelland, M. A. (2006). "History of the Development of Low Dosage Hydrate Inhibitors." Energy & Fuels **20**(3): 825-847.
Kelland, M. A. and N. J. Phillips (1999). The Application of Surfactants in Preventing Gas Hydrate Formation. London, Royal Society of Chemistry.
Kelland, M. A., T. M. Svartaas, J. Øvsthus, T. Tomita and J.-i. Chosa (2006). "Studies on some zwitterionic surfactant gas hydrate anti-agglomerants." Chemical Engineering Science **61**(12): 4048-4059.
Kelland, M. A., T. M. Svartås and L. D. Andersen (2009). "Gas hydrate anti-agglomerant properties of polypropoxylates and some other demulsifiers." Journal of Petroleum Science and Engineering **64**(1-4): 1-10.
Kelly, P. C., C. J. Cramer and D. G. Truhlar (2005). ""SM6: A Density Functional Theory Continuum Solvation Model for Calculating Aqueous Solvation Free Energies of Neutrals, Ions, and Solute-Water Clusters"." *Journal of Chemical Theory and Computation*: 1133-1152
King, J. H. E., J. L. Hutter, M. Y. Lin and T. Sun (2000). "Polymer conformations of gas-hydrate kinetic inhibitors: A small-angle neutron scattering study." The Journal of Chemical Physics **112**(5): 2523-2532.
Klomp, U. (2002). Method for inhibiting the pluggins of conduits by gas hydrates, Google Patents.
Klomp, U., V. Kruka and R. Reinjhart (1997). Low Dosage Inhibitors:(How) Do They Work.
Kuliev, A. M., A. M. Rasulov and F. A. Dashdamirov (1972). "A study of methanol recovery from in a unit with short-cycle adsorption." Journal Name: Gazov. Delo; (USSR); Journal Volume: 10: Medium: X; Size: Pages: 24-27.
Kuznetsova, T. (2001). Molecular modeling for thermodynamic properties of bulk and interfacial systems. [Bergen], University of Bergen, Department of Physics.
Kvamme, B. (1984). Thermodynamic properties of polyatomic fluids from atom-atom-interactions. [Trondheim] ,, Department of Chemical Engineering.
Kvamme, B. (1996). A new theory for the kinetics of hydrate formation. Proceedings of the Second International Conference on Natural Gas Hydrates, Toulouse, France.
Kvamme, B. (2000). "A unified nucleation theory for the kinetics of hydrate formation." Gas Hydrates: Challenges for the Future **912**: 496-501.
Kvamme, B. (2002). "Thermodynamic properties and dielectric constants in water/methanol mixtures by integral equation theory and molecular dynamics simulations." Physical chemistry chemical physics **4**(6): 942-948.
Kvamme, B. and R. Asnes (2006). "Kinetic Hydrate Inhibitors and Mass Transport Limitations." WSEAS TRANSACTIONS ON HEAT AND MASS TRANSFER **1**(5): 580.
Kvamme, B., A. Graue, E. Aspenes, T. Kuznetsova, L. Gránásy, et al. (2004). "Kinetics of solid hydrate formation by carbon dioxide: Phase field theory of hydrate nucleation and magnetic resonance imaging." Physical chemistry chemical physics **6**(9): 2327-2334.

Kvamme, B., A. Graue, T. Buanes, T. Kuznetsova and G. Ersland (2007). "Storage of CO2 in natural gas hydrate reservoirs and the effect of hydrate as an extra sealing in cold aquifers." International Journal of Greenhouse Gas Control **1**(2): 236-246.

Kvamme, B., G. Huseby and O. K. Forrisdahl (1997). "Molecular dynamics simulations of PVP kinetic inhibitor in liquid water and hydrate/liquid water systems." Molecular Physics **90**(6): 979-991.

Kvamme, B., T. Kuznetsova and K. Aasoldsen (2005). "Molecular dynamics simulations for selection of kinetic hydrate inhibitors." Journal of Molecular Graphics & Modelling **23**(6): 524-536.

Kvamme, B. and H. Tanaka (1995). "Thermodynamic stability of hydrates for ethane, ethylene, and carbon dioxide." Journal of Physical Chemistry **99**(18): 7114-7119.

Lachance, J. W., E. D. Sloan and C. A. Koh (2006). Calorimetric measurements of low dosage kinetic inhibitors
16th Symposium of Thermophysical Properties Boulder
Colorado.

Lachance, J. W., E. D. Sloan and C. A. Koh (2009). "Determining gas hydrate kinetic inhibitor effectiveness using emulsions." Chemical Engineering Science **64**(1): 180-184.

Larsen, R., C. Knight, K. Rider and E. Sloan Jr (1999). "Melt growth and inhibition of ethylene oxide clathrate hydrate." Journal of Crystal Growth **204**(3): 376-381.

Larsen, R., C. A. Knight and E. D. Sloan (1998). "Clathrate hydrate growth and inhibition." Fluid Phase Equilibria **150-151**: 353-360.

Leach, A. R. (1996). Molecular modelling: principles and applications. Harlow, Longman.

Lederhos, J. P., J. P. Long, A. Sum, R. L. Christiansen and E. D. Sloan (1996). "Effective kinetic inhibitors for natural gas hydrates." Chemical Engineering Science **51**(8): 1221-1229.

Long, J. (1994). Gas hydrate formation mechanism and kinetic inhibition, advisor: E. Dendy Sloan, Dept. of Chemical Engineering and Petroleum Refining.Colorado School of Mines.

Long, J., J. P. Lederhos, A. Sum and R. L. Christiansen (1994). Kinetic inhibitors of natural gas hydrates. . Proceedings of the Annual GPA Convention. . **73**.

Loveday, J. S., R. J. Nelmes, M. Guthrie, S. A. Belmonte, D. R. Allan, et al. (2001). "Stable methane hydrate above 2[thinsp]GPa and the source of Titan's atmospheric methane." Nature **410**(6829): 661-663.

Lyubartsev, A. and A. Laaksonen (2000). "M. DynaMix–a scalable portable parallel MD simulation package for arbitrary molecular mixtures." Computer Physics Communications **128**(3): 565-589.

Makogon, T. Y., R. Larsen, C. A. Knight and E. Dendy Sloan (1997). "Melt growth of tetrahydrofuran clathrate hydrate and its inhibition: method and first results." Journal of Crystal Growth **179**(1-2): 258-262.

Makogon, Y. F. (1999). Gas solubility in water, kinetics and morphology of gas hydrates
Annual report - Great Lakes Fishery Commission.

McQuarrie, D. A. (2000). Statistical mechanics. Sausalito, Calif., University Science Books.

Mennucci, B. and R. Cammi (2007). Continuum solvation models in chemical physics: from theory to applications. Chichester, John Wiley.

Modell, M. and R. Reid (1983). Thermodynamics and its Applications, Prentice Hall.

Moon, C., R. W. Hawtin and P. M. Rodger (2007). "Nucleation and control of clathrate hydrates: insights from simulation." Faraday Discussions **136**: 367-382.

Moon, C., P. Taylor and P. Rodger (2003). "Molecular dynamics study of gas hydrate formation." J. Am. Chem. Soc **125**(16): 4706-4707.

Mullin, J. W. (1993). Crystallization. London, Butterworth-Heinemann.

Nosé, S. (1984). "A molecular dynamics method for simulations in the canonical ensemble." Molecular Physics **52**(2): 255-268.

Nosé, S. (1991). "Constant temperature molecular dynamics methods " Progress of Theoretical Physics **103**: 1-46.

Olson, R., A. Marenich, C. Cramer and D. Truhlar (2007). "Charge Model 4 and intramolecular charge polarization." J. Chem. Theory Comput **3**(6): 2046-2054.
Quayle, O. R. (2002). "The Parachors of Organic Compounds. An Interpretation and Catalogue." Chemical Reviews **53**(3): 439-589.
Radhakrishnan, R. and B. L. Trout (2002). "A new approach for studying nucleation phenomena using molecular simulations: Application to CO[sub 2] hydrate clathrates." The Journal of Chemical Physics **117**(4): 1786-1796.
Rae, A. I. M. (2002). Quantum mechanics. Bristol, IOP Publ.
Ryckaert, J. P., G. Ciccotti and H. J. C. Berendsen (1977). "Numerical integration of the Cartesian equation of motions of a system with constraints: molecular dynamics of n-alkanes." Journal of Computational Chemistry **23**: 327.
Sakaguchi, H., R. Ohmura and Y. H. Mori (2003). "Effects of kinetic inhibitors on the formation and growth of hydrate crystals at a liquid-liquid interface." Journal of Crystal Growth **247**(3-4): 631-641.
Sapronova, A. and K. Johannsen (2008). Molecular Dynamics Study of Natural Gas Hydrate Kinetics in the Presence of KHI.
Schrodinger (2008). Jaguar. New York, Schrodinger, LLC.
Setaram (2003). Micro DSC VII Commissioning Utilisations. France.
Sewell, J. H. (1973). "A method of calculating densities of polymers." Journal of Applied Polymer Science **17**(6): 1741-1747.
Sloan, E. D. (1995). Method for controlling clathrate hydrates in fluid systems (Patent no.: 5432292) Golden, Colo., Colorado School of Mines.
Sloan, E. D. (1995). Method for controlling clathrate hydrates in fluid systems (Patent No.:5420370) Colorado School of Mines.
Sloan, E. D. (1998). Clathrate hydrates of natural gases. New York, Marcel Dekker.
Sloan, E. D. (2003). "Clathrate hydrate measurements: microscopic, mesoscopic, and macroscopic." The Journal of Chemical Thermodynamics **35**(1): 41-53.
Sloan, E. D. (2005). "A changing hydrate paradigm - from apprehension to avoidance to risk management." Fluid Phase Equilibria **228**: 67-74.
Sloan, E. D., R. L. Christiansen, J. P. Lederhos, J. P. Long, V. Panchalingam, et al. (1997). Additives and method for controlling clathrate hydrates in fluid systems. Golden, Colo., Colorado School of MInes.
Sloan, E. D. and C. A. Koh (2008). Clathrate hydrates of natural gases. Boca Raton, CRC Press.
Smith, P. and B. Pettitt (1994). "Modeling solvent in biomolecular systems." The Journal of physical chemistry **98**(39): 9700-9711.
Stephens, P., F. Devlin, C. Chabalowski and M. Frisch (1994). "Ab initio calculation of vibrational absorption and circular dichroism spectra using density functional force fields." The Journal of physical chemistry **98**(45): 11623-11627.
Storer, J., D. Giesen, C. Cramer and D. Truhlar (1995). "Class IV charge models: A new semiempirical approach in quantum chemistry." Journal of Computer-Aided Molecular Design **9**(1): 87-110.
Storr, M., P. Taylor, J. Monfort and P. Rodger (2004). "Kinetic inhibitor of hydrate crystallization." J. Am. Chem. Soc **126**(5): 1569-1576.
The Shodor Education Foundation, I. (1999-2000). Retrieved 08/10/09, 2009, from http://www.shodor.org/chemviz/basis/teachers/background.html.
Thompson, J., J. Xidos, T. Sonbuchner, C. Cramer and D. Truhlar (2002). "More reliable partial atomic charges when using diffuse basis sets." PhysChemComm **5**(18): 117-134.
Udachin, K. A., C. I. Ratcliffe and J. A. Ripmeester (2001). A Dense and Efficient Clathrate Hydrate Structure with Unusual Cages. **40:** 1303-1305.
Verlet, L. (1967). "Computer experiments on condensed fluids I; thermodynamical properties of Lennard-Jones molecules." Phys. Rev **159**: 98–103.

Appendix A

Atomic charges from Charge Model 4 (CM4)

Atom	C1	H2	H3	C4	H5	H6	C7	H8	C9	H10
Charge	0.07396	0.03549	-0.01022	-0.04266	0.02524	-0.0144	0.15393	0.00888	-0.01781	0.0161
Atom	H11	C12	H13	C14	H15	H16	C17	H18	C19	H20
Charge	-0.04231	0.11645	-0.10319	-0.01072	0.01931	-0.00641	0.17271	-0.04209	-0.02207	-0.05772
Atom	H26	C27	H28	C29	H30	H31	C32	H33	C34	H35
Charge	0.01045	0.14875	-0.09386	-0.02521	0.04688	0.0483	0.20086	-0.11526	-0.01764	0.02121
Atom	H36	C37	H38	C39	H40	H41	C42	H43	C44	H45
Charge	-0.03115	0.16164	-0.0074	-0.00988	-0.10538	-0.12923	0.17984	-0.07215	0.03749	-0.10057
Atom	H46	C47	H48	C49	H50	H51	C52	H53	C54	H55
Charge	-0.10588	0.19063	-0.02315	-0.01099	-0.06753	-0.00662	0.14743	-0.0641	-0.04046	0.03516
Atom	H56	C57	H58	H59	N60	C61	C62	C63	C64	C65
Charge	0.04959	0.13471	-0.04763	-0.0332	-0.34272	0.37851	-0.09243	-0.08443	-0.09067	-0.09215
Atom	C66	O67	H68	H69	H70	H71	H72	H73	H74	H75
Charge	0.10935	-0.44537	0.07039	0.06797	0.05724	0.06771	0.06664	0.06184	0.05613	0.07032
Atom	H76	H77	N78	C79	C80	C81	C82	C83	C84	H85
Charge	0.05241	0.05178	-0.33072	0.15465	-0.05583	-0.0738	-0.04199	-0.0747	0.40938	-0.0129
Atom	H86	H87	H88	H89	H90	H91	H92	H93	H94	O95
Charge	-0.00576	0.05086	0.03396	0.05538	0.06309	0.03083	-0.00894	0.04624	0.06523	-0.46898
Atom	N96	C97	C98	C99	C100	C101	C102	H103	H104	H105
Charge	-0.33794	0.13591	-0.07954	-0.08578	-0.07634	-0.07768	0.42745	0.04878	0.04758	0.0454
Atom	H106	H107	H108	H109	H110	H111	H112	O113	N114	C115
Charge	0.07469	0.06104	0.06716	0.06842	0.04437	0.06145	0.06309	-0.42673	-0.31267	0.1801
Atom	C116	C117	C118	C119	C120	H121	H122	H123	H124	H125
Charge	-0.04767	-0.08112	-0.07707	-0.07143	0.41313	0.01164	-0.00185	0.06309	0.02102	0.06597
Atom	H126	H127	H128	H129	H130	O131	N132	C133	C134	C135
Charge	0.06693	0.04267	0.07118	0.06504	0.05367	-0.45636	-0.29442	0.20607	-0.03164	-0.04196
Atom	C136	C137	C138	H139	H140	H141	H142	H143	H144	H145
Charge	-0.02249	0.01037	0.48264	-0.06865	-0.04234	0.04502	-0.00345	0.0619	0.03121	0.02236

Atom	H146	H147	H148	O149	N150	C151	C152	C153	C154	C155
Charge	0.0448	-0.0757	-0.05775	-0.42773	-0.28927	0.15259	-0.02918	-0.05841	-0.03019	0.01614
Atom	C156	H157	H158	H159	H160	H161	H162	H163	H164	H165
Charge	0.51716	0.02382	0.00842	0.00047	0.05945	0.06058	0.06034	0.0364	-0.01005	0.00501
Atom	H166	O167	N168	C169	C170	C171	C172	C173	C174	H175
Charge	-0.03753	-0.33592	-0.37845	0.20338	-0.03663	-0.05016	-0.06373	-0.08105	0.4365	-0.07562
Atom	H176	H177	H178	H179	H180	H181	H182	H183	H184	O185
Charge	-0.0899	0.00093	0.00961	0.04648	0.00414	0.05438	0.07018	0.05014	0.07593	-0.40235
Atom	N186	C187	C188	C189	C190	C191	C192	H193	H194	H195
Charge	-0.32185	0.13882	-0.0678	-0.0809	-0.06726	-0.05608	0.45633	0.01219	0.04086	0.04356
Atom	N186	C187	C188	C189	C190	H196	H197	H198	H199	H200
Charge	-0.32185	0.13882	-0.0678	-0.0809	-0.06726	0.00729	0.05208	0.065	0.04779	0.06811
Atom	H201	H202	O203	N204	C205	C206	C207	C208	C209	C210
Charge	0.0082	0.04226	-0.42549	-0.33901	0.16501	-0.02929	-0.05414	-0.06464	-0.08283	0.38715
Atom	H211	H212	H213	H214	H215	H216	H217	H218	H219	H220
Charge	-0.00628	-0.08225	-0.0242	0.01997	0.04568	0.0534	0.06122	0.02713	0.06264	0.05631
Atom	O221	N222	C223	C224	C225	C226	C227	C228	H229	H230
Charge	-0.4481	-0.31582	0.15531	-0.07112	-0.06882	-0.04839	-0.01086	0.44209	0.02993	-0.01793
Atom	H231	H232	H233	H234	H235	H236	H237	H238	O239	N240
Charge	0.07437	0.05578	0.04579	0.07417	0.04151	0.06465	0.01959	-0.00589	-0.34739	-0.35565
Atom	C241	C242	C243	C244	C245	C246	H247	H248	H249	H250
Charge	0.12733	-0.06003	-0.06629	-0.04529	-0.06847	0.4224	0.05198	0.04012	0.06433	-0.00315
Atom	H251	H252	H253	H254	H255	H256	O257	N258	C259	C260
Charge	0.05798	0.05952	0.0524	0.01052	0.049	0.00888	-0.42031	-0.34896	0.12337	-0.08359
Atom	C261	C262	C263	C264	H265	H266	H267	H268	H269	H270
Charge	-0.08569	-0.07756	-0.0873	0.39763	0.04332	0.03137	0.075	0.0539	0.05795	0.06927
Atom	H271	H272	H273	H274	O275					
Charge	0.05476	0.0719	0.05356	0.06207	-0.4509					

sum of atomic charges: 0

Atomic charges from Löwdin Population Analysis (LPA)

Atom	C1	H2	H3	C4	H5	H6	C7	H8	C9	H10
Charge	-0.2026	0.19169	0.22375	-0.3012	0.18427	0.18791	-0.13002	0.21984	-0.28382	0.18398
Atom	H11	C12	H13	C14	H15	H16	C17	H18	C19	H20
Charge	0.19913	-0.17383	0.20248	-0.22046	0.22241	0.20014	-0.12739	0.22871	-0.31386	0.19678
Atom	H21	C22	H23	C24	H25	H26	C27	H28	C29	H30
Charge	0.21268	-0.10103	0.21994	-0.28206	0.20487	0.2016	-0.14926	0.23818	-0.24747	0.20166
Atom	H31	C32	H33	C34	H35	H36	C37	H38	C39	H40
Charge	0.20212	-0.12386	0.21877	-0.27713	0.18726	0.22664	-0.132	0.22038	-0.30288	0.20549
Atom	H41	C42	H43	C44	H45	H46	C47	H48	C49	H50
Charge	0.20084	-0.10475	0.24446	-0.27397	0.17296	0.20939	-0.149	0.2029	-0.29633	0.22233
Atom	H51	C52	H53	C54	H55	H56	C57	H58	H59	N60
Charge	0.17913	-0.15294	0.21861	-0.26432	0.20375	0.19876	-0.22075	0.19494	0.18245	-0.31956
Atom	C61	C62	C63	C64	C65	C66	O67	H68	H69	H70
Charge	0.15059	-0.28239	-0.30672	-0.32518	-0.30997	-0.19108	-0.55172	0.19531	0.20623	0.18696
Atom	H71	H72	H73	H74	H75	H76	H77	N78	C79	C80
Charge	0.17779	0.17685	0.18439	0.19237	0.18182	0.19992	0.20451	-0.31797	-0.19494	-0.30685
Atom	C81	C82	C83	C84	H85	H86	H87	H88	H89	H90
Charge	-0.31927	-0.32948	-0.28326	0.15801	0.21146	0.21473	0.19393	0.19151	0.17885	0.18094
Atom	H91	H92	H93	H94	O95	N96	C97	C98	C99	C100
Charge	0.1746	0.18904	0.19446	0.20707	-0.52361	-0.33124	-0.18813	-0.30726	-0.32173	-0.30331
Atom	C101	C102	H103	H104	H105	H106	H107	H108	H109	H110
Charge	-0.28457	0.14382	0.21074	0.20733	0.19144	0.1892	0.1854	0.17867	0.17986	0.1814
Atom	H111	H112	O113	N114	C115	C116	C117	C118	C119	C120
Charge	0.20628	0.19976	-0.55691	-0.34008	-0.19005	-0.32208	-0.31968	-0.31088	-0.29007	0.12918
Atom	H121	H122	H123	H124	H125	H126	H127	H128	H129	H130
Charge	0.20566	0.21068	0.19227	0.19246	0.18603	0.18464	0.19042	0.18561	0.20067	0.20806
Atom	O131	N132	C133	C134	C135	C136	C137	C138	H139	H140
Charge	-0.50653	-0.30276	-0.23626	-0.32586	-0.29335	-0.32005	-0.33391	0.17833	0.18729	0.20433
Atom	H141	H142	H143	H144	H145	H146	H147	H148	O149	N150
Charge	0.19145	0.19637	0.18432	0.19707	0.17848	0.18995	0.17344	0.19822	-0.52813	-0.30606
Atom	C151	C152	C153	C154	C155	C156	H157	H158	H159	H160
Charge	-0.18425	-0.32582	-0.31259	-0.34516	-0.33862	0.12857	0.20481	0.24328	0.19082	0.19461
Atom	H161	H162	H163	H164	H165	H166	O167	N168	C169	C170
Charge	0.18492	0.19096	0.18478	0.21749	0.20115	0.18846	-0.59455	-0.37079	-0.21604	-0.33589
Atom	C171	C172	C173	C174	H175	H176	H177	H178	H179	H180
Charge	-0.3137	-0.29209	-0.27075	0.17258	0.22704	0.18219	0.17621	0.1967	0.1746	0.20021
Atom	H181	H182	H183	H184	O185	N186	C187	C188	C189	C190

Charge	0.18744	0.18416	0.20341	0.20062	-0.46913	-0.30654	-0.16847	-0.31968	-0.32673	-0.30856
Atom	C191	C192	H193	H194	H195	H196	H197	H198	H199	H200
Charge	-0.30261	0.16908	0.19833	0.19805	0.17819	0.21435	0.17341	0.18366	0.19363	0.18528
Atom	H201	H202	O203	N204	C205	C206	C207	C208	C209	C210
Charge	0.20376	0.19619	-0.58245	-0.28109	-0.20381	-0.33796	-0.32152	-0.31123	-0.28579	0.14153
Atom	H211	H212	H213	H214	H215	H216	H217	H218	H219	H220
Charge	0.20862	0.19315	0.1945	0.17936	0.1813	0.18628	0.17998	0.20445	0.19671	0.20223
Atom	O221	N222	C223	C224	C225	C226	C227	C228	H229	H230
Charge	-0.5359	-0.34111	-0.21777	-0.30693	-0.32097	-0.30837	-0.31765	0.1038	0.2012	0.18792
Atom	H231	H232	H233	H234	H235	H236	H237	H238	O239	N240
Charge	0.19269	0.20144	0.1846	0.18845	0.19523	0.18718	0.19694	0.19411	-0.48787	-0.31137
Atom	C241	C242	C243	C244	C245	C246	H247	H248	H249	H250
Charge	-0.18821	-0.31925	-0.31775	-0.30822	-0.29719	0.18596	0.20414	0.20314	0.18696	0.19454
Atom	H251	H252	H253	H254	H255	H256	O257	N258	C259	C260
Charge	0.17789	0.1876	0.17562	0.19714	0.19967	0.18333	-0.49214	-0.34955	-0.20501	-0.30744
Atom	C261	C262	C263	C264	H265	H266	H267	H268	H269	H270
Charge	-0.31984	-0.3004	-0.29445	0.14491	0.20086	0.1888	0.18792	0.19132	0.18268	0.18006
Atom	H271	H272	H273	H274	O275					
Charge	0.18765	0.1843	0.20537	0.19404	-0.49084					

sum	of	atomic	charges:	0

Appendix B

Sample input file for PVCap System I.

```
# Sample input file for the MD program, v.>=4.3 #
# Simulated system consists of  2 PVCap molecules,
# # Lines beginning with "#" are commentaries
 # In this file the commentaries go before the corresponding parameters. #
 # This file can be directly used as input (see directory sample for # short version of the input file) # #
 # Output control parameter #
Suitable values 2-10. The less number, the less you see in the output
# parameters higher than 7 used mostly for debug purposes
  5
#
# Full printout file name
  md43_fusionpwm
#   Base file name for output files:
#   Other files requested or created by the program have this name with
#   various extensions
  pwmsystem
# # Path to the molecular database # This directory contains *.mol files which describe the molecular
# structure and the force field
  ../moldb
#
# The program creates and updates periodically a restart file which
# contains configuration of the system and calculated averages.
# The program can be interrupted and then continued from the restart file
# without loosing any information.
#  If "Check only" parameter is true, the program does not run
# simulation. If it is a new run, the program only checks the input.
# If it is continuation of the old run, the program gives calculated results.
#
#  Read from        Dump              Check         Zero counter
# restart file?  restart file?         only?         of cpu time?
     .t.            .t.               .f.              .f.
# # The type of statistical ensemble. "Anisotropic NPT" means separate # pressure/volume control in each direction. Use this
#option only if the # system is really anisotropic (a piece of DNA, membrane, liquid crystal, # etc). Note, that for "constant
#pressure"=.t. "constant temperature" # must be also .true. (who knows what NVP ensemble is???). # Constant temperature?
#Constant pressure? Anisotropic NPT?
       .t.                .f.                .f.
#
#   Number of molecule types:
    3
#
#   which molecules:#  The database directory (specified above) should contain files #  H2O.mol, Na+.mol,  Cl-.mol
#  See README file about format of .mol files
  PVCAP_LPA    H2O_E     CH4
#
#   For each molecule:
#   Number of molecules:
  2      1306     260
#
#  non-bonded intramolecular interactions:Calculate intramolecular potential L-J and electrostatic for non-bound atoms,
#separated by #   more than 3 covalent bonds. Normally, it should be .true.    unimportant for small molecules)
  .t.          .t.          .t.       .t.     .t.
#
#    1 - 4 intramolecular interactions:#   Calculate L-J and electrostatic terms for 1-4 (i.e. separated by
#   3 covalent bonds) intramolecular interactions
  .t.          .t.        .t.       .t.        .t.
#   Scaling factors for 1-4 L-J interactions #  These are 0 in AMBER, 1 in CHARMM and 0.25 in GROMOS
#   Not important for small molecules
    1.           1.       1.          1.                  1.
```

```
#   Scaling factor for 1-4 electrostatic interactions
   1.          1.      1.          1.                  1.
#
#    intramolecular potential type #    Now it should be 0 for all molecules except the water. For water 1 is "harmonic" and 2
#"anharmonic" flexible SPC water #    (It tells the program to use a special subroutine)
  0          0         0       0          0
# # Rules for initial box size / density: # - If one of the box sizes is zero, the actual box size (cubic box) # is defined by
# the density. - If the density is also zero, the program run "vacuum # simulations". Set Ewald parameters (below) to 0 in
#the case of # vacuum simulations. # - If all the three box sizes are not zero, they define initial box size # and shape,
#and so the actual density # # Cell type: # 0 - rectangular # 1 - truncated octahedron: cube of side BOXL centered in 0,0,0
# with  truncated corners:|x|+|y|+|z| < 0.75*BOXL  2 hexagonal along Z axis temperature(K) density(g/cm**3) pressure (atm)
    200.0               0.7830                100.
#   box size (A)                                cell type
    36.09  36.09       50.5                    0
#
#  This is the long time step
#  Time step (s)      Small steps in one long
   1.0d-15              10
#
# Total (long)   Steps for interme-      take averages     dump restart file
#  MD-steps      diate averaging         each .. steps      after .. steps
   1000000              1000                        10              1000
#  Nose-Hoover thermostat parameters:Meaningful in const.-energy simulations(if const.temp.=.f.):!!ADDED:QTR after QT
# T-thermostat param(fs) P-thermostat(fs) Simplevelocity delta T (K) Intern.T-thermostat (fs) # scaling?
    100.0       100.0          7000.            .f.           5.      .t.      50.0
# # Rcutoff sets cut off radius for L-J and Real-space electrostatic forces # Interaction inside Rcut-fast are recalculated each
#short time step, interactions betweenRcut-fast and Rcutoff each long time step #
# Rcutoff(A)Rcut-fast forces check neighbors after .. steps

   12.0             6.0                   5

#=========================================

#   Treatment of electrostatic interactions:

#   Ewald parameters: alpha and fexp are set from the conditions:erfc(alpha*R)=required precision of the real-space Ewald

#  exp(-fexp)=required precision of reciprocal-space Ewald  the rule of thumb:

#    alpha*R               fexp (m/s**2)

    3.14159256           9.81

# If alpha*R above is negative, the reaction field method is used with # -alpha*R as dielectric permittivity, fexp is Debay

#screening length in Å # (setting Debay length to 0 means infinite Debue length, i.e non-conducting # solution) # If

#alpha is zero (exactly: between -1 and 0), no special treatment of # electrostatic interactions (simple spherical cutoff) # #

#Be careful by playing with these parameters and understand what are you # doing. Unproper setting can result in funny
#behavior of the system or too # long computation time. #

#=============================================

# which molecules move: # if .f., the molecules are fixed, but interact with other molecules.

   .t.       .t.       .t.             .t.               .t.

#   which molecules have translational DoFs:  if .f. but LMOVE=.t., the molecules can still rotate

   .t.       .t.       .t.             .t.               .t.
```

which molecules have rotational DoFs: # if LMOVE=.f. and LMOVETR=.f., the molecules should be fixed, but interact #with other molecules.

.t. .t. .t. .t. .t.

#

recalculate list of intramolec. interactions? may be .f., if you have a large molecule with stable conformation

Modified cross-inter?

.t. .f.

If true, constrain dynamics with SHAKE algorithm for specified # molecular species will be used. It will keep all

#the bond lengths constant. # No double time step algorithm in this case # which molecules considered as rigid (1/0) #

#Constrain dynamics? tolerance parameter (does not matter if Constrained dynamics = .f.)

.t. 0.5d-5 1 1 1 1 1 1 1 1

!!!! ADDED # Quaternion treatment? (rigid molecules with motion divided into COM-motion and rotation around COMs) #SHOULD BE TRUE ONLY IF CONSTRAINT DYNAMICS IS SPECIFIED AS WELL Exp-6 vdW as well?

.f. .f. .f. .f. .f. .f. .f.

Final positions to pdb-format file?

Pressure control for sum of X- and Y- pressure components?

Box volume corrections in Z-direction only?

TI over PP? All molecular species?

All molecular species?

Which type do the calcs for?

K_ONE K_SIX K_TWELVE ALAMBDA

.t. .t. .f. .f. .f. 2 2 2 4 0.95309d0

Initial state (from -1 to 4) # Values: -1 take initial center-of-mass coordinates of molecules from *.inp file 0

#take initial atom coordinates from *.inp file # /* .inp file should be written in free x y z format (one atom per line) #

#The order of atoms and molecules: # molecular type1 molecular type 2 # mol1 mol2 mol3 mol1 mol2 mol3 # at1 at2 at1 at2 #at1 at2 at1 at2 at1 at2 ... */ 1 start from FCC lattice 2 set a cylindrical hole along z-axis. Put molecules with parameter 1 #specified on the line below into the hole according initial coordinates in .mol file, and distribute others out the hole 3 the #same for spherical hole 4 start from cubic lattice set velocities to 0? | (otherwise, Maxwell distribution, or as it is at restart)

1 .f.

#

Parameters for above in cases 2,3 (specify 0 or 1)

0 0 0 0

#

If this parameter .t., the atoms described in file "fixed.atoms" will be put in a harmonic potential of this radius:

```
#  Radius of a hole          Keep initial         Permissible     File
#  for large molecules       configuration?       deviation?      name
    10.                      .f.                  3.       fixed.atoms
# # If you want to change temperature or density after restart.
# Change temperature at restart? Change density? Scale in
z-direction only?
    .f.                      .f.                  .f.
#
#  When to start final averaging
#  Final averaging after ..
#  intermediate averaging          XMOL config. file?
     0000                        .f.
# # This have a sense if you have to start from a very bad configuration # If total force on an atom exceed some level
#defined by the given # parameter, the force will be cut to this level in the internal units # Cut large forces? Parameter
   .t.                  1.d-4
#
#  RDFs have a separate restart file with extension .rdf
#  Calculate RDF?      Dump RDF?     Read restart RDF file?
   .f.                .f.          .f.
#
#  RDF for all sites?
#  (if .f., they should
#  be specified below)    Cutoff-RDF(A)       Resolution of RDFs
   .f.                 10.                200
#
#  dump trajectory (0/1/2)?              number of config. in a trajectory
#  0 - no trajectory                     file. Trajectory files have extensions
#  1 - unformatted files                 .001, .002, ...
#  2 - "XYZ" format          interval(s)
   1                     1.d-12          500
#  dump trajectory of molecules (1/0):
```

```
    1       1       1       1

#

#   TCF calculations

#   ----------------

#  Attention!  Tcf calculations are NOT parallelized and may essentially slow down parallel simulations

#

#  TCFs have a separate restart file with extension .tcf

#  NSTEG is number of points for calculation TCF

#  JUMP - number of MD steps between the points for calculation of tcf.

# calculate tcf?   restart tcf?   dump tsf?    NSTEG      JUMP

   .f.          .f.          .f.          200       5

# which of 12 tcf calculate (0/1/2): # 12 types: # 1 -velocity autocorrelations # 2 - angular velocity autocorrelations # 3 - 1
#order Legendre polynom for dipole moment # 4 - 2 order Legendre polynom for dipole moment # 5 – 1 order Legendre
#polynom for reorintational tcf defined by vector below # 6 - 2 order Legendre polynom for reorintational tcf

#defined by vector below # 7 - X projection of velocity TCF # 8 - Y projection of velocity TCF # 9 - Z projection of velocity

#TCF # 10 - X projection of angular velocity TCF # 11 – Y projection of angular velocity TCF # 12 - Z projection of

#angular velocity TCF # if "2" specified for tcf 7-9 or 10-12, then tcf projections are # calculated in molecular principal

#coordinate system; otherwise # they calculated in laboratorial coordinate system

 1 1 1 1 1 1 2 2 2 0 0 0

# # unit vectors for reorientations tcf # this vector is defined by 2 selected atoms on each molecule

  1          1    1    1

  1          2    1    1

#

#  Other optional parameters

#  if line "add <n>" is omitted, no optional parameters

#  Description of optional parameters is given in file Extra_param

#

add      0

#  Total number of RDF-s

2

#  RDFs are defined by "global" site number

#  First molecule type H2O have 3 sites with number 1,2,3
```

Second molecule Na has one site with number 4

and third molecule Cl has one site with number 5

C - C

This means RDF between sites 1 and 1, i.e. O atoms on H2O molecule

1 1

C - O

symbol & followed by a number means that these RDF will be averaged

(in this case: two hydrogens atoms (atoms 2 and 3 in H2O molecule)

are equivalent)

&2 O - O

1 2

1 3